TRANSITION TO TURBULENCE AND MIXING IN A QUASI-TWO-DIMENSIONAL LORENTZ FORCE-DRIVEN KOLMOGOROV FLOW

A Thesis
Presented to
The Academic Faculty

by

Radford Mitchell, Jr.

In Partial Fulfillment
of the Requirements for the Degree
Doctor of Philosophy in the
School of Physics

Georgia Institute of Technology
August 2013

TRANSITION TO TURBULENCE AND MIXING IN A QUASI-TWO-DIMENSIONAL LORENTZ FORCE-DRIVEN KOLMOGOROV FLOW

Approved by:

Professor Roman Grigoriev, Advisor
School of Physics
Georgia Institute of Technology

Professor Predrag Cvitanović
School of Physics
Georgia Institute of Technology

Professor Rafael de la Llave
School of Mathematics
Georgia Institute of Technology

Professor Michael Schatz
School of Physics
Georgia Institute of Technology

Professor Turgay Uzer
School of Physics
Georgia Institute of Technology

Date Approved: 3 May 2013

To Rebecca and Radford, my ever so supportive parents

ACKNOWLEDGEMENTS

First and foremost I wish to express my deepest gratitude to my advisor, Dr. Roman Grigoriev, for his infinite patience and wisdom as well as his guidance and support. And without whom, this thesis would not have been possible. I have learned an extraordinary amount from this man over the years that I have known him, and I believe him to be the one of the best advisors that a graduate student could ask for.

Next I want to acknowledge the members of my thesis committee. Not only for agreeing to serve on the committee but also for their suggestions in improving the thesis.

I would like to thank Dr. John F. Gibson for his assistance in helping me to work out the bugs in my Newton-Krylov code. I would also like to acknowledge my fellow graduate students Daniel Borrero and Ed Greco for many fruitful discussions over the years helping me to hash out various mathematical issues and computational difficulties; Balachandra Suri and Jeff Tithof for our many discussions about the details of the experiment and how best to incorporate them into the model. I would like to thank Jeff, in particular, for making all of the movies that I used in my thesis defense. I would like to also thank Alex Wiener for all of the time that he saved me by providing information concerning the necessary forms to fill out in order to graduate, formatting issues in the thesis, and a host of other details that I am glad I will soon no longer need to think about.

Finally, last, and certainly not least, I would like to thank my mom and dad from the bottom of my heart. Not only for helping me to pay my rent and bills during the two semesters when I had no funding, but, more importantly for all of the love, support, advice, and encouragement that they given me throughout my life.

TABLE OF CONTENTS

LIST OF TABLES

LIST OF FIGURES

SUMMARY

The research in this thesis was motivated by a desire to understand the mixing properties of quasi-two-dimensional flows whose time-dependence arises naturally as a result of fluid-dynamic instabilities. Additionally, we wished to study how flows such as these transition from the laminar into the turbulent regime. This thesis presents a numerical and theoretical investigation of a particular fluid dynamical system introduced by Kolmogorov. It consists of a thin layer of electrolytic fluid that is driven by the interaction of a steady current with a magnetic field produced by an array of bar magnets.

First, we derive a theoretical model for the system by depth-averaging the Navier-Stokes equation, reducing it to a two-dimensional scalar evolution equation for the vertical component of vorticity. A code was then developed in order to both numerically simulate the fluid flow as well as to compute invariant solutions. As the strength of the driving force is increased, we find a number of steady, time-periodic, quasiperiodic, and chaotic flows as the fluid transitions into the turbulent regime.

Through long-time advection of a large number of passive tracers, the mixing properties of the various flows that we found were studied. Specifically, the mixing was quantified by computing the relative size of the mixed region as well as the mixing rate. We found the mixing efficiency of the flow to be a non-monotonic function of the driving current and that significant changes in the flow did not always lead to comparable changes in its transport properties. However, some very subtle changes in the flow dramatically altered the degree of mixing. Using the theory of chaos as it applies to Hamiltonian systems, we were able to explain many of our results.

CHAPTER I

INTRODUCTION

1.1 Transport and mixing in fluid flows

Two-dimensional (2D) flows have proven to be very useful for studying various phenomena in fluid dynamics since, compared to three-dimensional flows, they are much more amenable to theoretical analysis and numerical investigation. In particular, much of our fundamental knowledge of transport properties of fluid flows has been developed using 2D models. Effectively 2D fluid flows are responsible for transport and mixing in many geophysical processes such as atmospheric [96] and oceanic [53, 135] flows as well as in convection processes within the Earth's mantle [56, 1]. Understanding 2D flows such as the motion of pollutants on the surface of the ocean would be invaluable for predicting, for example, the transport of the extensive amount of radioactive contamination released into the Pacific Ocean following the Fukushima nuclear reactor disaster in 2011. A better understanding of these types of flows could have perhaps improved some of the strategies employed in dealing with the recent *Deepwater Horizon* oil spill in the Gulf of Mexico. In addition, the transport and mixing properties of flows in the atmosphere in large part determines the global distribution of various chemical species. It has been shown that large scale flows on surfaces of constant density in the atmosphere can be well-modeled as a 2D flow [93]. A better fundamental grasp of the transport properties in these flows has significant implications for air quality, the absorption of ultra-violet radiation, and climate in general [54]. It could help predict, for instance, the evolution of the ash cloud following the volcanic eruption in Iceland in 2010. A 2D flow was also used to model the polar night jet that surrounds the ozone depleted region above Antarctica [11] which

suggests that mixing may have an important role to play in understanding climate change [3].

Two-dimensional laminar mixing is a key process in many types of microfluidic devices [69, 85], such as ones used for gene expression profiling and biological assays [114], which are essential in the development of new drugs and monitoring environmental pollutants. This type of mixing is also very useful in other processes like DNA purification and hybridization [41], polymerase chain reactions [133, 15], and protein folding [136]. Microfluidic devices promise to miniaturize many of these procedures (some of which would be impossible without miniaturization) and make them programmable in a fully integrated "lab-on-a-chip" environment [133, 24]. The microchannels on these chips require much smaller volumes of fluids than traditional methods and the fluid flow is much easier to control. The ability to effectively mix two or more fluids within the microchannels in a reasonable amount of time is crucial to this technology. For macroscopic systems, mixing is typically achieved using turbulence generated through some form of vigorous stirring. Turbulence occurs only in flows characterized by high Reynolds numbers $Re = UL/\nu$, where U and L are typical velocity and length scale of the flow and ν is the fluid viscosity. For most microfluidic applications, the length scales and velocity scales involved are such that Re is certainly less than 100 and typically $\mathcal{O}(1)$ or smaller [42]. Since for channel flow, turbulence occurs only for $Re \gtrsim 2000$, the flows in these on-chip devices are certainly expected to be laminar. Furthermore, in biofluids applications turbulence is an undesirable mechanism for mixing as the fluids contain delicate, long-chain molecules so the strain on them needs to be limited. The time-scale for molecular diffusion to mix fluids is much too large for this process by itself to be of much use on the microscale as it would require impractically long channels [85]. So for these applications to be of any success, we need to better understand how and why fluids stretch and fold (the necessary ingredients for mixing) in laminar flows and use this ever-expanding base of

knowledge to construct more efficient micromixers. The more understanding we have of the phenomenon of mixing in general, the more knowledge engineers will have to pull from in order to come up with better designs for the wide variety of important applications in this field.

Chaotic advection in 2D flows have provided numerous other technological advancements and improvements upon traditional methods, such as the creation of polymer blends [87], various multilayer films [106], as well as a vast improvement on the electrical conduction properties in the production of certain plastics and glasses [3]. The reduction to two dimensions has also provided insights into many difficult 3D problems ranging from mixing in the radiation zones of rotating stars [76] to confinement of thermonuclear plasmas [101]. So this simplification afforded by 2D flows is by itself a good reason to continue studying them as it will continue to impact our understanding of more complicated 3D flows.

1.2 Hamiltonian description

Much of our knowledge of transport properties in fluid flows comes from experimental observations or numerical simulations of the advection, or stirring, of passive tracers by the flow. The first observation is that these particles must be *passive*, which simply means that $\mathbf{u}_{\text{particle}} = \mathbf{u}_{\text{fluid}}$. In 2D, the velocity of a given particle is given by the rate of change of its position, $\mathbf{u}_{\text{particle}} = [\dot{x}, \dot{y}]$. The fluid velocity $\mathbf{u}_{\text{fluid}} = [u_x(x, y, t), u_y(x, y, t)]$ is obtained by solving a set of partial differential equations that describe the motion of the fluid (e.g. Navier-Stokes, Euler, etc.). For 2D incompressible flows, the velocity of the fluid can be defined through the streamfunction $\Psi(x, y, t)$: $u_x = \partial_y \Psi$, $u_y = -\partial_x \Psi$. And since the velocity of a passive particle must be identical to that of the fluid, we have

$$\begin{aligned} \dot{x} &= u_x = \partial_y \Psi, \\ \dot{y} &= u_y = -\partial_x \Psi. \end{aligned} \tag{1}$$

Thus, the dynamics of passive tracers in 2D flows of incompressible fluids is formally described by a Hamiltonian system with one degree of freedom. The streamfunction Ψ plays the role of a Hamiltonian, the coordinates x and y are the conjugate variables, and the phase space is the configuration space. This holds regardless of whether or not there is dissipation in the flow. It is the incompressibility of the fluid that makes it a Hamiltonian system. So, the problem of understanding mixing begins rather than ends with the specification of the fluid velocity.

Time-independent 2D flows are always integrable (because Ψ is conserved), and the trajectories of tracers are regular, meaning they coincide with the closed streamlines of the flow, resulting in poor mixing. The introduction of time-dependence effectively makes the velocity field a three-dimensional flow, which, in the absence of any additional conservation laws, makes the flow nonintegrable. Streamlines in these flows can be chaotic even if the underlying velocity field is regular (e.g., stable and time-periodic). If this is the case, they will diverge exponentially fast from one another, resulting in rapid stretching and folding of fluid elements. This process, known as chaotic advection or Lagrangian chaos, is the underlying mechanism responsible for efficient mixing.

The idea that particle motion in a 2D incompressible flow can be understood as a Hamiltonian dynamical system with one degree of freedom is rather obvious and has been well-known in the fluids community for many years. But the fact that the introduction of time-dependence could lead to chaotic particle motion for *any* Reynolds number was largely overlooked until the early 1980s. Indeed, even as late as 1986, Aref pointed out that, "...the notion of stochastic particle motion within laminar flows runs counter to common intuition to such a degree that the range of applicability of early model results has been questioned" [4]. Dynamical systems perspective introduced by Aref revolutionized our understanding of transport in fluid (and granular) flows.

Traditionally, the standard approach to predicting how material is transported in a fluid flow was to run numerical simulations of a model and use the resulting velocity field data to determine how the initial distribution of the material evolved in time. Since time-dependent flows are generally the rule rather than the exception, even in two dimensions, tracers are often advected in a chaotic manner and this leads to sensitive dependence on initial conditions (both on the initial position as well as the initial time) and makes the aforementioned approach a rather unreliable way to forecast the transport of material. Further, the full trajectory history is often quite complicated and difficult to interpret. Rather than focusing on individual trajectories, a more global understanding can be obtained by examining the underlying structure in a time-dependent flow that organizes and governs the overall transport.

1.3 Time-periodic flows

One of the simplest 2D models in which chaotic mixing can occur is the 'blinking-vortex' flow introduced by Aref [2]. Historically the first study of the mixing properties of a fluid system, this model was originally proposed as an idealization of a periodically stirred fluid and consists of a pair of spatially separated fixed point vortices which are alternately turned on for one half of the period T. Numerical simulations showed that when both vortices are running continuously (i.e., $T = 0$), the flow is time-independent and, thus, integrable. For small nonzero T, it was found that the trajectories nearest the vortices become chaotic. The size of the mixed region increases monotonically with T until, at some finite critical value of T, the entire domain becomes uniformly mixed.

The first systematic investigation of mixing in a time-periodic 2D flow is due to Khakhar *et al.* [64]. This study introduced an idealized model, known as the 'tendril-whorl' flow, in which uniform shear is followed by differential rotation and showed that mixing takes place in the vicinity of separatrices associated with saddle

fixed points of the period-T map of the flow, while the KAM tori surrounding the elliptic fixed points serve as transport barriers. The same structures were shown to also control mixing in the 'blinking vortex' flow. These studies demonstrated that laminar, time-periodic, area-preserving 2D flows can produce efficient mixing.

The results of these idealized models raised questions as to whether or not real-world laminar fluid flows could give rise to chaotic streamlines. This prompted the analytical and numerical study of chaotic advection in a journal bearing Stokes flow with physical boundary conditions [4, 20]. The basic setup is that of a Couette flow between non-coaxial rotating cylinders, where time-periodicity is introduced by alternating the rotation between the inner and outer cylinders. By varying the distance between the axes of the cylinders as well as the time-interval for which one of the cylinders rotates, one can obtain various flow patterns with both regular and chaotic trajectories. The experimental realization of this flow [19] showed excellent agreement with numerical results. Subsequently, the experimental study of cavity flows by Chien *et al.* [23] showed the existence of transverse intersections of homo/heteroclinic manifolds at small Reynolds numbers, providing even more evidence for the mixing capabilities of 2D laminar flows.

Rom-Kedar *et al.* [102] proved the existence of chaotic trajectories analytically for a model flow produced by a pair of time-independent point vortices perturbed by a time-periodic shear. The theory of lobe dynamics developed in this paper set up a framework for quantitative description of transport across separatrices of the unperturbed flow which evolve into a homoclinic tangle in the presence of a time-dependent perturbation. In conjunction with the analytic techniques introduced by Melnikov [77], this framework enabled them to estimate the fluxes between different regions of the flow domain.

Recently, many experimental and theoretical studies of mixing in 2D flows have used thin layers of electrolyte placed over various arrangements of permanent magnets.

The fluid flow is driven by the Lorentz force which arises when electric current flows through the electrolyte. Since this setup is closely related to our work, we describe here other studies which used it.

Rothstein *et al.* [103] discovered the existence of persistent spatial patterns, which they called strange eigenmodes, in a flow driven by a combination of a time-periodic current and either a disordered or a square array of magnets. These patterns were shown to emerge as a result of a delicate balance between advective stretching and molecular diffusion. The process of mixing was observed to continue even after these structures reached an asymptotic shape. The same experimental setup was subsequently used to investigate the rate of mixing [130]. By examining the spatial structure of persistent patterns, it was found that locally mixing rates are controlled by stretching, but on large scales they are governed by diffusive transport. Additionally, it was discovered that mixing rates could be dramatically enhanced by breaking certain spatial and temporal symmetries.

Voth *et al.* [129] used a disordered array of magnets and time-periodic current to drive the flow and were able to use flow measurements to construct forward and backwards finite-time Lyapunov exponent (FTLE) fields which follow the time evolution of the unstable and stable manifolds of saddle points of the flow, thus providing an empirical method for visualizing the geometrical structures underlying the mixing process. A follow-up experimental study carried out using magnets arranged in a square, hexagonal, and a disordered array [7] found that the probability distribution of FTLEs exhibited self-similar behavior regardless of the flow pattern or the degree of mixing in the system.

Fluid mixing was also studied in time-dependent flows driven by steady current. Danilov *et al.* [32] performed a combined experimental and theoretical study of mixing by a time-periodic four-vortex flow. The numerical study of a truncated analytic model showed that separatrices partitioned the flow domain into regions

with different mixing rates and that transport between these regions was a relatively slow process compared to the mixing within these regions. The theory of adiabatic chaos was used to explain the results and showed that long-term transport could effectively be modeled as a random walk of an adiabatic invariant.

1.4 Aperiodic flows

For aperiodic flows one can still define the underlying structures that are analogous to stable and unstable manifolds. These are referred to as Lagrangian Coherent Structures (LCS). The main idea behind the notion of LCS is that they divide the flow into regions having different dynamics. In a 2D flow, LCS are material lines advected by the flow as a continuous set (surfaces for a 3D flow), and they separate the domain into various regions where the motion of tracers over a finite time interval is qualitatively different [92]. These structures are effectively invariant manifolds, hence act as transport barriers in the flow. Computing an LCS directly is often a difficult, if not impossible, task, however there are indirect methods that can be used to reveal their existence based on the behavior of trajectories near such structures. By measuring the amount of "stretching" between trajectories through the computation of an FTLE field, one can interpret its ridges as being the LCS of the flow [108]. The FTLE will be defined more rigorously in Chapter 5 of this thesis.

Another driving force behind the development of the theory of LCS is the need of a frame-independent definition of these structures. There are two different ways that one can use to describe the time-evolution of a fluid. From the Eulerian perspective, one considers how the fluid velocity changes at any given point as a function of time. Mathematically, this means that $\mathbf{u} = \mathbf{u}(\mathbf{x}, t)$. Alternatively, in the Lagrangian description, individual fluid parcels are followed through time. In other words, $\mathbf{x}(\mathbf{a}, t)$ gives the position of parcel $\mathbf{a}$ at time t and these two points of view are related by $\mathbf{u}(\mathbf{x}(\mathbf{a}, t), t) = \partial_t \mathbf{x}(\mathbf{a}, t)$. Since we are concerned with understanding the advection of

particles in the fluid, the Lagrangian perspective is clearly the more natural of the two. But perhaps more importantly is the fact that the characterization of flow structures in terms of the velocity field do not remain invariant under a time-dependent transformation of the frame of reference so, for unsteady flows, it is not clear what the preferred frame should be [93]. This is because velocity fields as well as their streamlines look different when measured from different reference frames. So what appears to be a "coherent structure" one frame can looks completely "incoherent" in another. Reliable prediction of transport requires frame-invariant techniques and the Lagrangian point of view provides an objective and unambiguous way to identify these dynamically organizing structures.

For instance, for the *Deepwater Horizon* oil spill mentioned earlier, Olascoaga and Haller were able to take the velocity field data that existed at the time and using an LCS analysis, they predicted the formation and evolution of two major unexpected instabilities that occurred in the contamination pattern [86]. They computed all of the LCS in each data set, and in both cases they captured an LCS that was 99% stronger than all the coexisting LCS and used these to forecast the emergence of these two instabilities four to six days before they were actually observed. Fiorentino *et al.* used an LCS-based analysis to understand why, in the absence of any point sources of pollution, certain nearshore coastal areas can have high microbial levels while neighboring regions do not [44]. A similar LCS analysis was used to develop pollution control schemes in the coastal areas of Monterey Bay [27] as well as in southeastern Florida [70]. The release of contaminants in regions like these can have a profound environmental impact on the local ecosystem, particularly if it does not get transported out into the open ocean where it disperses but instead recirculates near the coast. Whether or not this happens is sensitive both to where, as well as when, the pollution is released. By using very accurate high frequency data obtained with radar, they were able to reconstruct the surface velocity at particular locations, compute

the hidden LCS, and from this, they were able to devise an automated pollution release schedule that minimized the recirculation of pollution near the coastline. This approach has proven successful in tackling a wide variety of other problems such as air traffic control [93], the kinematic theory of unsteady flow separation, jellyfish predation [94], and blood flow in the arteries [109].

1.5 Objectives and outline

As discussed in the previous sections, the majority of previous studies have focused on time-periodic flows as the simplest system that could produce efficient mixing. However, our fundamental understanding of this process is currently limited primarily to weak monochromatic perturbations of integrable flows. Which features of strongly perturbed time-dependent flows are responsible for good mixing is less clear. In particular, it is not obvious that the insights developed in the perturbative regime would also carry over to the case when the perturbation (e.g., the time-dependent component of the flow) is not weak compared with the integrable base flow (e.g., the time-independent component).

We will try to answer these questions using an example of Kolmogorov flow: a two-dimensional flow driven by an imposed shear. Our objective is to understand how its transport properties change in the process of transition from steady laminar flow (characterized by extremely poor mixing properties) to turbulence (which mixes extremely well). In particular, while time-dependence is a necessary condition for mixing via chaotic advection in 2D, is it also a sufficient condition? Can we expect the mixing to improve monotonically with the strength of externally applied shear? And is there a strong correlation between mixing quality of the flow and its type (steady, time-periodic, quasi-periodic, aperiodic)?

In Chapter 2 we present the model of the Kolmogorov flow in a thin liquid layer and show how and when it can be reduced to an effectively two-dimensional flow.

Chapter 3 describes the numerical methods used in analyzing this flow. The bifurcation sequence describing transition from steady laminar flow to weakly turbulent (more accurately aperiodic) flow is described in Chapter 4 and its mixing properties are investigated in Chapter 5. Finally, our conclusions are presented in Chapter 6.

CHAPTER II

MODEL

2.1 Problem description

We consider an electromagnetically-driven, quasi-two-dimensional experimental flow inspired by a model originally proposed by Kolmogorov and later investigated by Arnold and other mathematicians [6, 78] that made key contributions to the development of the theory of stability and dynamical systems. Bar magnets with alternating polarity in conjunction with a steady current generates a Lorentz force that drives a flow in a thin layer of electrolyte supported from below by a thin layer of liquid dielectric (see Fig. 1). Originally this flow was realized using only a single homogeneous layer of electrolyte. Years later, however, in an attempt to decrease the variation of the velocity with height, a new setup was employed by Marteau *et al.* [75] wherein the single layer was replaced by two layers of miscible fluids with different densities. The bottom layer was a heavier electrolyte (salt water) which was driven while the top layer (fresh water) was the one on which measurements were performed. An alternative implementation of the two layer setup was constructed by Rivera and Ecke [100] where an electrolyte was suspended above an immiscible layer of heavier dielectric fluid, which acts as a lubricant between the solid bottom and the electrolyte layer. This system is believed to be an improvement over previous setups as immiscibility enhances stratification and, as such, is the one we chose to model. Indeed, through a 3D direct numerical simulation of decaying vortical flows, Satijn *et al.* [105] found that a two layer, immiscible system tends to inhibit vertical motion and maintains its two-dimensionality for a larger range of Reynolds numbers than one using only a single layer. Next, we describe how our model is derived by reducing the Navier-Stokes

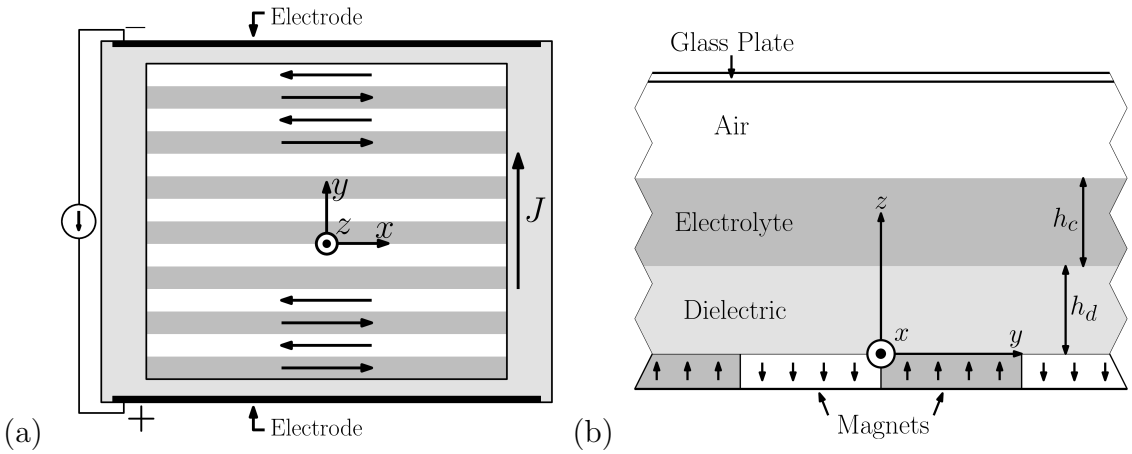

Figure 1: The experimental setup for the quasi-2D Kolmogorov flow, viewed (a) from above and (b) from the side.

equation to 2D.

The laminar flow field in our two-layer system is inherently three-dimensional in the sense that the velocity field generally depends on all three coordinates, $\mathbf{v} = \mathbf{v}(x, y, z, t)$. It is described by the Navier-Stokes equation for an incompressible fluid ($\nabla \cdot \mathbf{v} = \mathbf{0}$)

$$\rho(\partial_t \mathbf{v} + \mathbf{v} \cdot \nabla \mathbf{v}) = -\nabla \mathbf{p} + \mu \nabla^{\mathbf{2}} \mathbf{v} + \mathbf{f} + \rho \mathbf{g}, \tag{2}$$

where $\rho\mathbf{g}$ is the gravitational force and $\mathbf{f}$ is the electromagnetic force in the plane of the fluid (the xy-plane).

We assume that the magnet array is infinitely long in the x (longitudinal) direction and periodic in the y (transverse) direction. By symmetry, the magnets produce a magnetic field that has no component along the longitudinal direction:

$$\mathbf{B} = B_y(y, z)\hat{\mathbf{y}} + B_z(y, z)\hat{\mathbf{z}}. \tag{3}$$

Since the z-component of the magnetic field in the electrolyte varies linearly with z and roughly sinusoidally with y, we can write

$$B_z = (B_1 z + B_0)\sin(\kappa y), \tag{4}$$

where $\kappa = \pi/w$ and w is the width of each magnet. A uniform and constant current with density $\mathbf{J} = J\hat{\mathbf{y}}$ passing through the electrolyte along the tranverse direction

results in the Lorentz force density which is given by

$$\mathbf{f} = \mathbf{J} \times \mathbf{B} = \begin{cases} J(B_1 z + B_0)\sin(\kappa y)\hat{\mathbf{x}}, & h_d < z < h_d + h_c, \\ 0, & 0 < z < h_d \end{cases} \tag{5}$$

in the electrolyte and the dielectric, respectively.

For thin layers of fluids driven by a weak in-plane forcing, the velocity component normal to the plane is negligible compared to the in-plane components. The characteristic times $\rho_d h_d^2/\mu_d$, $\rho_c h_c^2/\mu_c$ (≈ 10 s) describing equilibration of momentum in the vertical direction are much smaller than those associated with the horizontal directions, $\rho_c w^2/\mu_c$ (≈ 150 s). Furthermore, the direction of $\mathbf{f}$ is independent of z. Hence, we can assume the *direction* of the velocity to be independent of the height z, which, in the spirit of Dovzhenko *et al.* [38], allows the velocity field to be factored as

$$\mathbf{v}(x, y, z, t) = P(z)\mathbf{u}(x, y, t) \equiv P(z)[u_x(x, y, t)\hat{\mathbf{x}} + u_y(x, y, t)\hat{\mathbf{y}}], \tag{6}$$

where $P(z)$ describes the vertical velocity profile. We impose the normalization condition

$$P(h_c + h_d) = 1 \tag{7}$$

to make the factorization unique, so $\mathbf{u}(x, y, t)$ can be interpreted as the velocity of the top surface of the conducting layer.

Substitution of (6) into (2) gives

$$\begin{aligned} \rho P \partial_t \mathbf{u} + \rho P^2 \mathbf{u} \cdot \nabla_\parallel \mathbf{u} &= -\nabla_\parallel p + P\mu\nabla_\parallel^2 \mathbf{u} + \mathbf{u}\mu\nabla_\perp^2 P + \mathbf{f}, \\ \nabla_\perp p &= \rho \mathbf{g}, \end{aligned} \tag{8}$$

along with $\nabla_\parallel \cdot \mathbf{u} = 0$, where the subscripts $\parallel$ and $\perp$ represent the horizontal and vertical components, respectively. In general, the vertical profile $P(z)$ depends on the exact form of forcing ($\mathbf{f}$) and the horizontal flow profile ($\mathbf{u}$). We start off by solving (8) for $P(z)$ assuming a steady, laminar solution of $\mathbf{u}$ for the forcing given by (5).

2.2 Kolmogorov flow

For small current density J, the direction of the horizontal flow profile ($\mathbf{u}$) follows that of the forcing (5), so we can look for laminar solutions of the form

$$\mathbf{u}(x, y, t) = u_0 \sin(\kappa y)\hat{\mathbf{x}}. \tag{9}$$

Substituting this into (8) yields a hydrostatic pressure distribution and a boundary value problem for the vertical profile

$$P'' - \kappa^2 P = -\frac{J}{u_0 \mu_c}(B_1 z + B_0), \qquad h_d < z < h_d + h_c. \tag{10}$$

$$P'' - \kappa^2 P = 0, \qquad 0 < z < h_d \tag{11}$$

where the prime denotes differentiation with respect to z. The solutions to the above differential equations are given by

$$P_\kappa = \begin{cases} Ce^{\kappa z} + De^{-\kappa z} + \frac{JB_1}{u_0 \mu_c \kappa^2} z + \frac{JB_0}{u_0 \mu_c \kappa^2}, & h_d < z < h_d + h_c, \\ Ee^{\kappa z} + Fe^{-\kappa z}, & 0 < z < h_d. \end{cases} \tag{12}$$

The unknown coefficients C, D, E, and F can be obtained using the continuity of the velocity and stress at the dielectric-electrolyte interface ($z = h_d$), the no-slip boundary condition at the bottom of the dielectric ($z = 0$), and the stress-free boundary condition at the top of the electrolyte ($z = h_d + h_c$, electrolyte-air interface):

$$\mu_d P'(h_d^-) = \mu_c P'(h_d^+), \quad P(h_d^-) = P(h_d^+), \quad P(0) = 0, \quad P'(h_d + h_c) = 0. \tag{13}$$

Finally, u_0 can be found using (7).

Once the coefficients have been computed, we can define the ratio of velocities at the top and bottom of the electrolyte layer

$$s = \frac{P(h_d + h_c)}{P(h_d)}. \tag{14}$$

For a monotonically varying profile, the value of s describes how strongly the magnitude of velocity varies with z in the electrolyte, with $s = 1$ corresponding to a

z-independent velocity profile. Unfortunately, the functional form of expression (14) is quite unwieldy and does not allow one to easily deduce the dependence on experimental parameters.

2.3 Unidirectional flow

We can derive a relatively simple analytical expression for the ratio of velocities (s) in the special case where we ignore the y dependence of the magnetic field, B_z, which can be thought of as the $\kappa \to 0$ limit of (4). In this case $B_z = B_1 z + B_0$, and the laminar flow is given by $\mathbf{u}(x, y, t) = u_0 \hat{\mathbf{x}}$. The solution (12) is then replaced by

$$P_0 = \begin{cases} -\frac{JB_1}{6u_0\mu_c} z^3 - \frac{JB_0}{u_0\mu_c} z^2 + Cz + D, & h_d < z < h_d + h_c, \\ Ez + F, & 0 < z < h_d. \end{cases} \tag{15}$$

Although the functional forms of the vertical velocity profile for the Kolmogorov flow $P_\kappa(z)$ and the uniform flow $P_0(z)$ are quite different, their shape is virtually indistinguishable, as figure 2 illustrates. This suggests that quasi-2D flows with arbitrary horizontal flow profiles $\mathbf{u}(x, y, t)$ and moderately high Reynolds numbers may be accurately described using the normalized form of the velocity profile (15).

Computing the coefficients using the boundary conditions (13) we find that the ratio of the velocities at the top and the bottom of the electrolyte layer is given by

$$s = 1 + \frac{1}{2}\frac{\mu_d h_c}{\mu_c h_d}\left(1 + \frac{1}{6}\frac{\triangle B}{B_{mean}}\right), \tag{16}$$

where $\triangle B = B_1 h_c$ is the change in magnetic field across the thickness of the electrolyte and $B_{mean} = B_0 + B_1 h_b + \frac{1}{2} B_1 h_c$ is the mean magnetic field in the electrolyte.

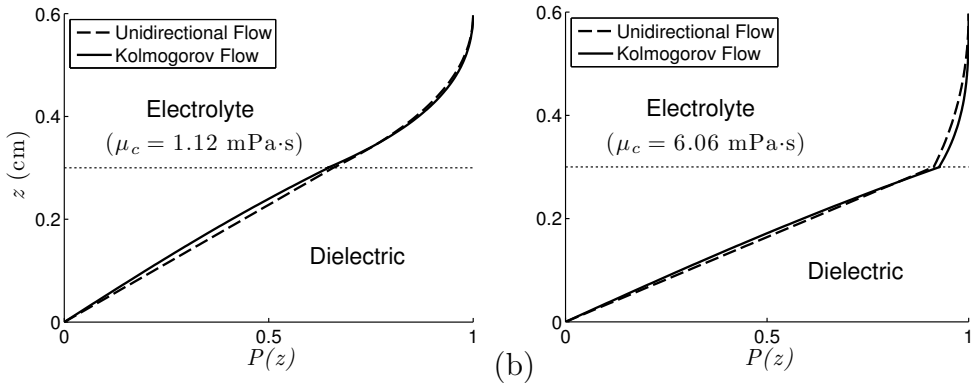

Figure 2: Analytical results for the vertical flow profile in both layers, with $h_d = h_c = 0.3$ cm, for (a) the low viscosity electrolyte and (b) the high viscosity electrolyte. The ratios of the velocities, as defined by (14), are: (a) uniform flow: $s = 1.52$, Kolmogorov flow: $s = 1.55$ and (b) uniform flow: $s = 1.09$, Kolmogorov flow: $s = 1.08$.

2.4 Quasi-2D flow

We can generalize the procedure employed in the previous section for flows driven by plane-parallel electromagnetic forces. By relying on the ansatz (6), we can derive an evolution equation that describes quasi-2D flows beyond the laminar flow into (moderately) high Reynolds numbers. Indeed, integrating the first of the two equations in (8) over the z coordinate, 0 to $h_d + h_c$, and taking a curl, we obtain an equation for the vertical component of the vorticity $\Omega = \partial_x u_y - \partial_y u_x$:

$$\partial_t \Omega + \beta \mathbf{u} \cdot \nabla_\parallel \Omega = \nu \nabla_\parallel^2 \Omega - \alpha \Omega + W, \tag{17}$$

where the parameters α, β, and ν are defined as follows

$$\nu = \frac{\int_0^{h_d+h_c} \mu P dz}{\int_0^{h_d+h_c} \rho P dz}, \quad \alpha = \frac{\mu_d P'(0)}{\int_0^{h_d+h_c} \rho P dz}, \quad \beta = \frac{\int_0^{h_d+h_c} \rho P^2 dz}{\int_0^{h_d+h_c} \rho P dz}. \tag{18}$$

In particular, we obtain the following expression for the Rayleigh friction coefficient, using the vertical velocity profile (15):

$$\alpha = \left(\frac{\mu_d}{\rho_c}\frac{1}{h_d h_c}\right) \Big/ \left(1 + \frac{1}{2}\frac{h_d}{h_c}\frac{\rho_d}{\rho_c} + \frac{1}{3}\frac{\mu_d}{\mu_c}\frac{h_c}{h_d}\left(1 + \frac{1}{8}\frac{\triangle B}{B_{mean}}\right)\right). \tag{19}$$

For the set of parameters used in the experiment, the Rayleigh friction coefficient has a very weak dependence on B_1 and B_0, with the term containing $\triangle B/B_{mean}$ contributing approximately 2% to the friction coefficient, so for practical purposes one can set $\triangle B = 0$.

The source term W on the right-hand side of (17) corresponds to the z-component of the curl of the depth averaged force density

$$W = \frac{\int_0^{h_d+h_c} (\partial_x f_y - \partial_y f_x) dz}{\int_0^{h_d+h_c} \rho P dz}. \tag{20}$$

Parameters $\beta = 1$, $\nu = 0.0115$ cm^2/s, and $\alpha = 0.1141$ s^{-1} were selected to be representative of a typical experimental setup. Furthermore, we chose the domain width $L_y = 5$ cm corresponding to four magnets of width $w = 1.25$ cm and the length $L_x = 2L_y = 10$ cm. For simplicity, unlike the experimental system which is larger and features physical (no-slip) lateral boundary conditions, we assume periodic boundary conditions. The effect of the bottom boundary, however, is included in our model via the Rayleigh friction term $-\alpha\Omega$. The importance of this term is described by the non-dimensional combination $F = \alpha/\nu\kappa^2 \approx 1.57$ which shows that it is comparable to the viscous term $\nu\nabla^2\Omega$. Finally, we take $W = A\sin(\pi y/w)$, where A measures the strength of the driving force and is used as a control parameter analogous to the Reynolds number. It is significant to note that in almost every study modeling electromagnetically driven thin films, the Rayleigh friction term is a phenomenological term that is assumed at the outset, but in the derivation of our model it arises naturally in the reduction to 2D. To the best our knowledge, no one else has provided an explicit theoretical derivation for this term in a two-layer system.

The vorticity equation (17) was solved numerically using a pseudospectral (Fourier) method with 64×128 modes. As a check, we recalculated one of the bifurcation sequences using 128×256 modes which yielded less than a 1% difference in both the leading stability eigenvalues and the location of the bifurcations. Temporal discretization used a second-order, semi-implicit, operator-splitting scheme with an adaptive

time step [95, 8]. This is described in more detail in the next chapter.

CHAPTER III

NUMERICAL METHODS

3.1 Integration of the vorticity equation

The nonlinear PDE for the vorticity (17) is solved by assuming periodic boundary conditions in both x and y and discretizing it in Fourier space using a spectral grid of 64×128 modes, which corresponds to a mesh size of $\Delta q_x = 2\pi/L_x \approx 1.257$ cm^{-1} ($\Delta x \approx 0.0781$ cm) and $\Delta q_y = 2\pi/L_y \approx 0.6283$ cm^{-1} ($\Delta y \approx 0.0781$ cm). Discretization in time is done via a three substep, semi-implicit, operator-splitting scheme [95, 8]. The splitting used is known as the Strang-Marchuk splitting (see Fig. 3.1) and is guaranteed to be 2nd-order in time provided each substep uses a method with at least 2nd-order convergence [113, 74].

For a general first order equation,

$$\partial_t u = \mathcal{L}u + \mathcal{N}[u] + F, \tag{21}$$

where $\mathcal{L}u$, $\mathcal{N}[u]$, and F denote the linear, nonlinear, and inhomogeneous (source) terms, respectively, the Strang-Marchuk protocol involves the following steps:

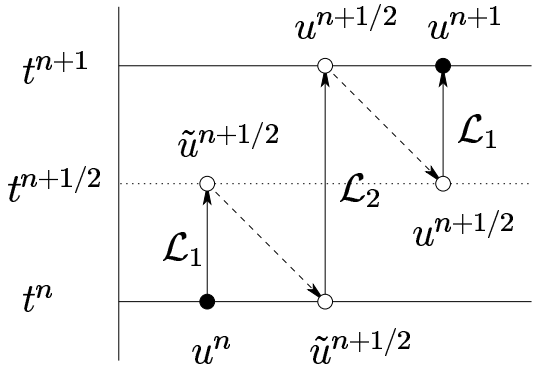

Figure 3: A visual illustration of the Strang-Marchuk operator splitting

1. $t \in (t^n, t^{n+1/2})$: $\quad u(t^n) = u^n \quad \longrightarrow \quad \tilde{u}^{n+1/2} = u(t^{n+1/2})$

   - $\tilde{u}^{n+1/2} = \left(I - \frac{\Delta t}{4}\mathcal{L}\right)^{-1} \left(\frac{\Delta t}{2}F + (I + \frac{\Delta t}{4}\mathcal{L})\right) u^n$

2. $t \in (t^n, t^{n+1})$: $\quad u(t^n) = \tilde{u}^{n+1/2} \quad \longrightarrow \quad u^{n+1/2} = u(t^{n+1})$

   - $u^{n+1/2} = \tilde{u}^{n+1/2} + \frac{\Delta t}{6}\left(k_1 + 2(k_2 + k_3) + k_4\right)$
     - $k_1 = \mathcal{N}[\tilde{u}^{n+1/2}]$
     - $k_2 = \mathcal{N}[\tilde{u}^{n+1/2} + \frac{\Delta t}{2}k_1]$
     - $k_3 = \mathcal{N}[\tilde{u}^{n+1/2} + \frac{\Delta t}{2}k_2]$
     - $k_4 = \mathcal{N}[\tilde{u}^{n+1/2} + \Delta t k_3]$

3. $t \in (t^{n+1/2}, t^{n+1})$: $\quad u(t^{n+1/2}) = u^{n+1/2} \quad \longrightarrow \quad u^{n+1} = u(t^{n+1})$

   - $u^{n+1} = \left(I - \frac{\Delta t}{4}\mathcal{L}\right)^{-1} \left(\frac{\Delta t}{2}F + (I + \frac{\Delta t}{4}\mathcal{L})\right) u^{n+1/2}$

In the particular case of the vorticity equation (17) we have $u \to \Omega$, $\mathcal{L} = \nu\nabla^2 - \alpha$, $\mathcal{N}[\cdot] = \mathbf{u} \cdot \nabla$, and $F = A\sin(\pi y/w)$, where w denotes the width of a single magnet. All spatial derivatives are computed in Fourier space. In steps 1 and 3, the vorticity is updated implicitly in Fourier space through the linear and forcing terms via the Crank-Nicolson method (CN). In step 2, it is updated explicitly in physical space through the advection term via the fourth-order Runge-Kutta method (RK4).

One could, in principle, use a 2nd-order Runge-Kutta method (RK2) in step 2 as this would not affect the overall order of convergence of the algorithm. However, despite the increase in the number of operations necessary to implement RK4, it is actually more efficient than RK2 in the long run. For moderate to high Reynolds number calculations, an adaptive time-stepping scheme proves to be an invaluable part of this integration scheme both for stability as well as computational speed. It turns out that one can incur the same amount of error with a much larger time step using CNRK4, so, even for moderate integration times, it easily surpasses CNRK2

in terms of computational time despite requiring twice as many operations in step 2. The adaptive time-stepping algorithm is fairly straightforward and proceeds as follows on each time step. Advance the state by a whole time step and then by two half time steps. If the relative error between the two is greater than some tolerance ϵ, let $\Delta t = \Delta t/2$ and repeat. Otherwise, go to the next time step. Let $\Delta t = \sqrt{2}\Delta t$ for the next time step if the relative error on the previous one was less than $\epsilon/4$. Keep Δt the same if not.

3.2 Time evolution of passive tracers

The dynamics of passive tracers in a two-dimensional, incompressible flow is governed by the equations of motion (1). In order to time-evolve the tracers over long time scales, a very accurate numerical scheme is required to solve these equations. In particular, since the system (1) is Hamiltonian, a method is needed that preserves the symplectic nature of this flow. Otherwise, conserved quantities (e.g., the value of the streamfunction Ψ and the corresponding action) will not be preserved, and the results of long-time calculations might simply reflect the numerical integration errors instead of the actual dynamics.

The accuracy of numerically computed trajectories is especially sensitive to the precision of the calculations in the neighborhood of saddles, where exponentially small errors can result in $\mathcal{O}(1)$ changes even in the short term dynamics. For instance, an error, whatever its source, which results in the trajectory crossing a separatrix of the flow produces a qualitatively different outcome. Since the velocity field $\mathbf{u}(\mathbf{x}, t)$ is defined on a grid, the right-hand-side of the system (1) has to be interpolated, introducing an additional source of error into the numerical integration. Hence, unlike analytical models, where the accuracy of the integrator near saddles can be increased by, for example, using a smaller time step or higher-precision arithmetics, no such band-aid is available in situations where the fluid flow itself is computed numerically.

Below we discuss different ways to address this problem.

3.2.1 General symplectic integrators

The Gauss-Legendre methods [51] form a family of collocation schemes based on Gauss quadrature. One nice property about them is that any s-stage Gauss-Legendre method has order $2s$ making them twice as efficient as most other multi-stage algorithms with the same order of convergence. It is customary to arrange the Runge-Kutta coefficients in a Butcher tableau as shown in Table 1. Based on these coeffi-

Table 1: The Butcher tableau for an arbitrary Runge-Kutta method.

c_1	a_{11}	a_{12}	$\cdots$	a_{1s}
c_2	a_{21}	a_{22}	$\cdots$	a_{2s}
$\vdots$	$\vdots$	$\vdots$	$\ddots$	$\vdots$
c_s	a_{s1}	a_{s2}	$\cdots$	a_{ss}
	b_1	b_2	$\cdots$	b_s

cients, the solution to the initial value problem, $\dot{\mathbf{x}} = \mathbf{u}(t, \mathbf{x})$, $\mathbf{x}(t_0) = \mathbf{x}_0$ will have the form

$$\mathbf{x}_{n+1} = \mathbf{x}_n + h \sum_{i=1}^{s} b_i \mathbf{k}_i,$$

where

$$\mathbf{k}_i = \mathbf{u}_i(t_n + c_i h, \mathbf{x}_n + h \sum_{i=1}^{s} a_{ij} \mathbf{k}_j), \quad i = 1, \ldots, s$$

and h is the time step. Lasagni has shown that a Runge-Kutta method is symplectic provided it satisfies $b_i b_j = b_i a_{ij} + b_j a_{ji}$ for $i, j = 1, \ldots, s$ which means that no explicit Runge-Kutta method can be symplectic [68]. By inspection of Table 2, it is clear that the 4th-order, 2-stage Gauss-Legendre Runge-Kutta method satisfies the symplectic condition. Since this method is fully implicit, one must solve a set of nonlinear equations at every time step. No explicit Runge-Kutta method is symplectic anyway, so not much can be done about this. However, this method is A-stable. In

Table 2: Coefficients for the 2-stage Gauss-Legendre Runge-Kutta method.

$\frac{1}{2} - \frac{\sqrt{3}}{6}$	$\frac{1}{4}$	$\frac{1}{4} - \frac{\sqrt{3}}{6}$
$\frac{1}{2} + \frac{\sqrt{3}}{6}$	$\frac{1}{4} + \frac{\sqrt{3}}{6}$	$\frac{1}{4}$
	$\frac{1}{2}$	$\frac{1}{2}$

other words, its region of absolute stability lies entirely in the left half of the complex plane regardless of the magnitude of the time step.

Since the symplectic integrators are implicit, in order to advect the set of tracers forward in time, one must solve the set of nonlinear equations

$$\mathbf{G}_i = \mathbf{u}_i(\mathbf{k}_j) - \mathbf{k}_i = 0 \tag{22}$$

by first linearizing it

$$D\mathbf{G}_{ij}\delta\mathbf{k}_j = -\mathbf{G}_i, \quad \text{where } D\mathbf{G}_{ij} = D\mathbf{u}_{ij} - \mathbf{I} \tag{23}$$

and then performing a sequence of Newton iterations on the linearized equation until the magnitude of the residual $\mathbf{G}_i$ falls below some suitable tolerance. In practice, this process converges fairly quickly even for a large number of tracers. The Jacobian $D\mathbf{u}_{ij}$ is computed on each Newton step using forward differencing, and the $\mathbf{k}_i$ are evaluated for each tracer using a cubic interpolant. At the beginning of each time step, two Euler steps are used to obtain initial guesses for both $\mathbf{k}_1$ and $\mathbf{k}_2$.

3.2.2 Predictor-corrector methods

If the underlying flow happens to be time-independent, one can instead constrain the trajectory of each tracer to follow the streamline defined by the initial condition $\Psi_s = \Psi(\mathbf{x}_0)$. The easiest way to accomplish this is by applying a correction $\delta\mathbf{x}_n$ to the position $\mathbf{x}_n$ at every step t_n, such that the corrected position lies on the original streamline:

$$\Psi(\mathbf{x}_n + \delta\mathbf{x}_n) = \Psi_s. \tag{24}$$

This is a nonlinear equation that can be solved by Newton iteration:

$$\mathbf{x}_n^{k+1} = \mathbf{x}_n^k + \left(\Psi_s - \Psi(\mathbf{x}_n^k)\right) \frac{\nabla\Psi(\mathbf{x}_n^k)}{|\nabla\Psi(\mathbf{x}_n^k)|^2}, \tag{25}$$

where $|\nabla\Psi(\mathbf{x})|^2 = \mathbf{u}^2(\mathbf{x})$ can be computed spectrally. In practice, the corrector requires at most two or three iterations per time step.

For unsteady flows, the value of the streamfunction will not be conserved along the streamline, so we will need an additional equation to update its value. For instance, for slowly varying unsteady flows (adiabatic limit) the generalization

$$\mathbf{x}_n^{k+1} = \mathbf{x}_n^k + \left(\Psi_s - \Psi(\mathbf{x}_n^k, t_n)\right) \frac{\nabla\Psi(\mathbf{x}_n^k, t_n)}{|\nabla\Psi(\mathbf{x}_n^k, t_n)|^2}, \tag{26}$$

of (25) can be used, where

$$\dot{\Psi}_s = \partial_t \Psi(\mathbf{x}(t), t) \tag{27}$$

and $\Psi_s(0) = \Psi(\mathbf{x}_0, 0)$. The idea is that, unlike the dynamics of $\mathbf{x}(t)$, the dynamics of $\Psi_s(t)$ are not sensitive to small errors in the neighborhood of the saddles.

For time-periodic flows, it may be more convenient to instead represent the streamfunction in terms of a perturbation about a steady state

$$\Psi(x, y, t) = \Psi_0(x, y) + \varepsilon\Psi_1(x, y, t), \tag{28}$$

where the perturbation Ψ_1 has zero time average and is normalized such that its time-averaged norm $\langle\|\Psi_1\|_2\rangle_t$ is equal to that of the time-averaged streamfunction $\|\Psi_0\|_2$. (Here and below $\|\ \|_2$ denotes the 2-norm and $\langle\ \rangle_t$ denotes the time average.) The parameter

$$\varepsilon = \frac{\langle\|\Psi_1 - \Psi_0\|_2\rangle_t}{\|\Psi_0\|_2} \tag{29}$$

quantifies the strength of the perturbation (unsteady component of the flow).

The time-averaged streamfunction Ψ_0 evolves along a streamline according to

$$\dot{\Psi}_0 = \frac{\partial\Psi_0}{\partial x}\dot{x} + \frac{\partial\Psi_0}{\partial y}\dot{y} = \varepsilon\left(\frac{\partial\Psi_0}{\partial x}\frac{\partial\Psi_1}{\partial y} - \frac{\partial\Psi_0}{\partial y}\frac{\partial\Psi_1}{\partial x}\right) \tag{30}$$

and for weakly perturbed flows ($\epsilon \ll 1$) changes very slowly. Hence one can use a corrector (25) with $\Psi \to \Psi_0$.

3.3 Newton-Krylov solver

In order to find invariant states of the system such as fixed points and periodic orbits, one must solve a very high-dimensional set of nonlinear equations which, using the standard Newton-Raphson approach, is a computationally impractical task. There is just not enough memory on most computers to construct Jacobians of this size, not to mention the time it would take to do so on each Newton step. As such, techniques were developed that use Newton's method but solve it in a subspace spanned only by the "important" directions – the other directions being strongly contracting. Such methods are referred to as inexact, or Jacobian-free, Newton-Krylov methods.

First, though, one must acquire good initial guesses. If there are stable attractors for the range of parameter values in question, one can easily obtain good guesses by integrating arbitrary initial conditions for long periods of time for various values of a particular parameter. While certainly a brute force approach, it will find them if they are there. Once one of these guesses converges to a solution, one can numerically continue it to smaller and larger values of the parameter until a bifurcation occurs. Examining how the stability eigenvalues change will indicate what type of bifurcation has taken place.

If no stable solutions exist, one can alternatively obtain initial guesses for unstable solutions through a temporal recurrence analysis. Starting with some arbitrary initial state Ω_0, one then time evolves it and looks for minima of the function $\phi(\Omega, T) = ||\Omega(x, t+T) - \Omega(x,t)||_2$. The pairs $(\Omega(x,t), T)$ for these various minima will provide guesses for both the initial state as well as for the period of the orbit to feed into the Newton-Krylov solver.

To find a time-periodic solution, one must solve the equation

$$G(\Omega, T) = f^T(\Omega) - \Omega = 0, \tag{31}$$

where $f^T(\Omega)$ is the time-T map of the Navier-Stokes equation. The Newton iteration

for $G(\Omega) = 0$ derives from a multivariate Taylor expansion about the current iterate Ω_k:

$$G(\Omega_{k+1}) = G(\Omega_k) + DG(\Omega_k)(\Omega_{k+1} - \Omega_k) + \mathcal{O}(|\Omega_{k+1} - \Omega_k|^2). \tag{32}$$

Dropping the higher order terms yields a sequence of linearized systems over which one must iterate.

$$J(\Omega_k)\delta\Omega_k = -G(\Omega_k), \quad \Omega_{k+1} = \Omega_k + \delta\Omega_k, \quad k = 0, 1, \ldots \tag{33}$$

J is the associated Jacobian matrix, $DG_{ij} = \frac{\partial G_i}{\partial \Omega_j} = Df_{ij} - I$. In order to start the iteration, the above equation must be supplemented by an initial guess, Ω_0 which is sufficiently close to the true solution so that the method successfully converges. Additionally, there is a continuous translational symmetry in the longitudinal direction (along the length of the bar magnets; shifts in this direction will be denoted X) as well as one in time. The derivatives $\partial_t\Omega$ and $\partial_x\Omega$ must be added to the Jacobian as its last two rows and last two columns in order to provide constraints to the linearized system. This ensures both that the Newton step will be in a direction orthogonal to the symmetries and that the Jacobian will be nonsingular. Additionally, this provides the equations necessary in order to solve for both T and X. Now we have a linear system of the form $A \cdot \delta\Omega - b = 0$ which one then solves in the Krylov subspace $\mathcal{K}_m$,

$$\mathcal{K}_m = \text{span}(r, Ar, A^2r, \ldots, A^{m-1}r), \tag{34}$$

where $r = b - A \cdot \delta\Omega$. The basic idea is that one seeks an approximation $\delta\Omega^{(m)}$ to the solution of $A \cdot \delta\Omega - b = 0$ by requiring that

$$\begin{cases} \delta\Omega^{(m)} \in \mathcal{K}_m, \\ A \cdot \delta\Omega^{(m)} - b \perp q_j, \quad j = 1, 2, \ldots, m, \end{cases} \tag{35}$$

where q_j are the basis vectors that span the subspace $\mathcal{K}_m$. There are a number of ways to construct the Krylov subspace and solve the linearized system of equations. One such method is a stabilized version of the biconjugate gradient method (Bi-CGSTAB)

[127]. There is also the transpose-free quasi-minimal residual algorithm (TFQMR) which is based on the conjugate gradient squared method (CGS) [46]. The method used in the code is known as the generalized minimal residual method or GMRES for short. This method guarantees a monotonically decreasing residual, a property not shared by either Bi-CGSTAB or TFQMR [65]. The algorithm is as follows [17]:

1. Start: Let Ω_n denote the current iterate and compute $G(\Omega_n)$. η denotes the current forcing parameter.

2. Arnoldi process:

   - Take $\delta\Omega^{(0)} = 0$ and form $r^{(0)} = -G - J \cdot \delta\Omega^{(0)} = -G$.
   - Compute $\beta = ||r^{(0)}||_2$ and $q_1 = r^{(0)}/\beta$.
   - For $k = 1, 2, \ldots, k_{max}$

     (a) Form $q_{k+1} = Jq_k$ and do modified Gram-Schmidt to the previous q_j

     $$h_{j,k} = \langle q_{k+1}, q_j \rangle, \quad j = 1, \ldots, k$$
     $$\hat{q}_{k+1} = q_{k+1} - \sum_{j=1}^{k} h_{j,k} q_j$$
     $$h_{k+1,k} = ||\hat{q}_{k+1}||_2$$
     $$q_{k+1} = \hat{q}_{k+1}/h_{k+1,k}$$

     (b) If there is a loss of orthogonality in the basis set

     for $j = 1, \ldots, k$

     $$h_{tmp} = \langle q_{k+1}, q_j \rangle$$
     $$h_{j,k} = h_{j,k} + h_{tmp}$$
     $$q_{k+1} = q_{k+1} - h_{tmp} q_j$$
     $$h_{k+1,k} = ||\hat{q}_{k+1}||_2$$
     $$q_{k+1} = \hat{q}_{k+1}/h_{k+1,k}$$

     (c) Approximate the norm of the residual $\rho_k = ||G + J \cdot \delta\Omega^{(k)}||_2 \approx ||G(\Omega_n + \delta\Omega^{(k)})||_2$ if we stopped at this step.

(d) If $\rho_k \leq \eta ||G(\Omega_n)||_2$, set $m = k$ and exit loop.

3. Form the approximate solution:

   - Let H_m be the $(m+1) \times m$ matrix whose entries are the coefficients $h_{j,k}$ and define $V_m \equiv [q_1, q_2, \cdots, q_m]$.
   - Find the vector y_m that minimizes $||\beta e_1 - H_m y||_2$ over all $y \in \mathbf{R}^m$, where $e_1 = [1, 0, \cdots, 0]^T \in \mathbf{R}^{m+1}$.
   - Project y_m into the full space via $\delta\Omega^{(m)} = V_m y_m$ and exit the inner loop

The forcing parameter η is updated each time prior to entering the inner (linear) loop. It is a rather complicated formula and is based on a rule developed by Eisenstat and Walker [40]. The idea is that initially, the iterate Ω_n may be far from the true solution and one should not expect the inner part of the solver to reduce the residual significantly so η should start out close to one. But as the residual decreases so should η in order to recover the theoretical quadratic convergence of the outer (nonlinear) part of the solver as one approaches the true solution. The reader is referred to [61, 40] for details.

Probably the most important aspect of the Newton-Krylov methods is that the Jacobian J is never actually needed in explicit form. The Arnoldi process only requires the matrix-vector products Jq. These are approximated via a forward difference directional derivative that employs the scaling on the difference increment proposed by Kelley [61] which has its roots in the approach for numerically computing columns of a Jacobian discussed in [34].

$$Df(\Omega_n; q_j) \approx \frac{||q_j|| f^T(\Omega_n + \epsilon\xi(\Omega_n, q_j) q_j / ||q_j||) - f^T(\Omega_n)}{\epsilon\xi(\Omega_n, q_j)}, \tag{36}$$

where $\xi(\Omega_n, q_j) = \max(|\Omega_n \cdot q_j|, ||q_j||) \cdot \text{sign}(\Omega_n \cdot q_j)/||q_j||$ and $\epsilon \sim 10^{-7}$.

Care must be taken once the inner iteration is exited and the Newton step is obtained. This is the start of the outer, nonlinear iteration. The line segment $\delta\Omega_n =$

$-(DG(\Omega_n))^{-1}G(\Omega_n)$ is only guaranteed to provide a *direction* in which the residual will be reduced. Various global convergence strategies can be implemented in order to control the size of the Newton step such that one actually does end up with a decrease in the residual once the step is taken. This is often done either through a backtracking line-search approach or a model-trust region approach [34]. In the code, the line-search approach was chosen because of the relative simplicity of its implementation. The idea is to to model the scalar function $\phi(\lambda) = ||G(\Omega_n + \lambda\delta\Omega_n)||_2^2$ with a polynomial and use the value λ_{min} that both minimizes the polynomial as well as reduces the residual in order to scale the step length. However, if λ_{min} is too close to 0, the step size can become too small and the method may stagnate as a result. Alternatively, if λ_{min} is too close to 1, the step size can be too large, and the solution might be missed. As such, we employ the safeguarding procedure suggested by Kelley [60].

$$\lambda = \begin{cases} s_0\lambda_c & \text{if } \lambda_{min} < s_0\lambda_c, \\ s_1\lambda_c & \text{if } \lambda_{min} > s_1\lambda_c, \\ \lambda_{min} & \text{otherwise} \end{cases} \tag{37}$$

Here λ_c is the current value of λ, $s_0 = 0.1$ and $s_1 = 0.5$. Let $\lambda_m = \lambda_c/2$. If λ_c does not provide a reduction in the residual G, then $\phi(\lambda_m)$ is computed and the polynomial that interpolates ϕ at $0, \lambda_m$, and λ_c is given by

$$p(\lambda) = \phi(0) + \frac{\lambda}{\lambda_c - \lambda_m}\left(\frac{(\lambda - \lambda_m)(\phi(\lambda_c) - \phi(0))}{\lambda_c} + \frac{(\lambda_c - \lambda)(\phi(\lambda_m) - \phi(0))}{\lambda_m}\right), \tag{38}$$

$$\text{which is minimized by } \quad \lambda_{min} = \frac{1}{2}\frac{\lambda_m^2(\phi(\lambda_c) - \phi(0)) - \lambda_c^2(\phi(\lambda_m) - \phi(0))}{\lambda_m(\phi(\lambda_c) - \phi(0)) - \lambda_c(\phi(\lambda_m) - \phi(0))}. \tag{39}$$

If $p''(\lambda_{min}) > 0$, then λ is given by the safeguarding condition (37). Otherwise we set $\lambda = s_1\lambda_c$. If a reduction in the residual is obtained by the Newton step $\lambda\delta\Omega_n$ then we are finished with the outer iteration and take the Newton step. If not, then we set $\lambda_c = \lambda$ and repeat the three-point parabolic interpolation. If λ becomes too small, then we have stagnated. The entire solver is then aborted, and one must find a better initial guess.

Finding fixed points uses the exact same solver except the period T is fixed at an arbitrary, but small, value of 2.0 s, which means that the linearized system has one less dimension than the one just described (i.e., since T is no longer a degree of freedom, there is no need to supply the orthogonality constraint equation equation $\frac{\partial \Omega}{\partial t} \cdot \delta\Omega = 0$).

In order to determine the stability of a converged solution, one simply builds up a Krylov subspace for it. The leading eigenvalues of the matrix H_m will converge to the leading stability eigenvalues of the solution as m gets large. For this system, convergence of the eigenvalues generally required $m \sim 0.01N$, where N is the dimension of the full space.

3.4 Variational method for computing periodic orbits in a flow

The previous section discussed computing periodic orbits in the sense of a repeating flow field. This section illustrates a very powerful and robust method for computing periodic orbits within the flow field. In the case of an area-preserving flow, these will be saddle and elliptic periodic orbits and they repeat with the same frequency as that of the particular time-periodic flow one is considering. For this system, it turns out that the saddle orbits are impossible to compute with conventional Newton-Raphson type methods. The eigenvalues of the saddles in all of the periodic flows that were found are $\lambda \sim \mathcal{O}(1)$ and the periods were $T \sim \mathcal{O}(100)$ which means along any unstable orbit there will be a stretching factor $\sim \exp(\mathcal{O}(100))$. There are nowhere near enough digits of accuracy on a computer to find orbits like these using Newton-Raphson methods. Multishooting, in combination with the Newton-Raphson method, attempts to eliminate this long-time exponential instability by splitting orbits into shorter segments with more manageble expansion rates. The variational method as described in [67, 31] is essentially an infintesimal step version of this strategy. Rather than making a local guess and "shooting", this method starts with a global guess of

points distributed on some loop that resembles the topology of the true orbit. Then a differential flow which governs the dynamics of the Newton-descent minimizes a cost function (quantifies the deviation of the loop flow from the true dynamical flow) and drives the trial loop to a true periodic orbit.

3.4.1 Derivation of the method

The loop will be defined as a smooth, differentiable closed curve $\tilde{x}(s)$, where s is uniformly spaced on the interval $[0, 2\pi]$ with the periodicity constraint $\tilde{x}(s) = \tilde{x}(s+2\pi)$ and an associated loop tangent vector defined by

$$\tilde{v}(\tilde{x}) = \frac{d\tilde{x}}{ds}. \tag{40}$$

The true periodic solution is governed by the dynamical flow

$$\frac{dx}{dt} = v(x), \tag{41}$$

and on the loop $v = v(\tilde{x})$. The goal is to deform the loop until v aligns with $\tilde{v}$ at every point on the loop. Up until now the magnitude of the loop tangent has been somewhat arbitrary. To ensure that the magnitudes of the tangent and velocity vectors match up, one needs to define a scaling parameter

$$\lambda = \frac{\Delta t}{\Delta s} = \frac{T}{2\pi}. \tag{42}$$

One cost functional that will serve to align the two vectors is

$$F^2[\tilde{x}] = \frac{1}{2\pi} \oint ds(\tilde{v} - \lambda v)^2. \tag{43}$$

Just as when using Newton's method, in practice, one can easily overshoot the true solution and put one's current guess outside of the basin of attraction for the method. As such, people generally use the so-called damped (or "step-reduced") Newton's method. In this spirit, the continuous deformations of the loop will, in addition,

be parameterized by a fictitious time τ such that the decrease of F^2 is ensured. Differentiating the cost functional with respect to τ yields

$$\frac{dF^2}{d\tau} = \frac{1}{\pi} \oint ds(\tilde{v} - \lambda v) \frac{d}{d\tau}(\tilde{v} - \lambda v). \tag{44}$$

Now, if we assume that

$$\frac{d}{d\tau}(\tilde{v} - \lambda v) = -(\tilde{v} - \lambda v) \tag{45}$$

then $F^2 = -\frac{1}{2}\frac{dF^2}{d\tau}$ and $F^2 \sim e^{-2\tau}$, so the cost functional is guaranteed to be an exponentially decreasing function of the fictitious time parameter. Substituting $\tilde{v} = \frac{d\tilde{x}}{ds}$ into Eq. 45 yields the Newton descent PDE (Eq. 46), the dynamics of which deforms the initial loop into the periodic orbit.

$$\frac{\partial^2 \tilde{x}}{\partial s \partial \tau} - \lambda A \frac{\partial \tilde{x}}{\partial \tau} - \frac{\partial \lambda}{\partial \tau} v = \lambda v - \tilde{v}, \quad A_{ij} = \frac{\partial v_i(x)}{\partial x_j}. \tag{46}$$

Before describing the particular implementation of the method, a few things should be mentioned. Once a periodic orbit is reached, it is invariant under cyclic permutations of the points. Thus, there is a marginal (zero eigenvalue) direction v making the operator $\partial_s - \lambda A$ increasingly singular as the loop approaches the true solution. This situation can be remedied by adding a constraint equation to the discretization of this operator. The simplest way to do this is to introduce a Poincare section by fixing one coordinate of one of the points on the loop. This will add an equation to the linearized system to solve for the period T (or equivalently for λ since $T = 2\pi\lambda$). However, for the flows discussed in this thesis, this procedure needed to be modified. The period of every orbit being solved for was already known apriori. This means that the term $\frac{\partial \lambda}{\partial \tau} v$ in Eq. 46 needs to be set to zero since λ is constant with respect to the fictitious time. Additionally, none of the spatial coordinates were known apriori. As such, the 2-d flow was converted into a 3-d (x, y, t) flow and the t-coordinates were fixed at *every* point on the loop with Δt being constant. The details of how this was done will be discussed in the next section.

3.4.2 Implementation of the method

In order to implement the variational method, we first discretize the PDE using a five-point centered finite-difference scheme. Let N be the number of points on the loop. The operator $\frac{\partial}{\partial s}$ is given by

$$D = \frac{1}{12h}\begin{pmatrix} 0 & 8 & -1 & & & & & & 1 & -8 \\ -8 & 0 & 8 & -1 & & & & & & 1 \\ 1 & -8 & 0 & 8 & -1 & & & & & \\ & & & & & \cdots & & & & \\ & & & & & & 1 & -8 & 0 & 8 & -1 \\ -1 & & & & & & & 1 & -8 & 0 & 8 \\ 8 & -1 & & & & & & & 1 & -8 & 0 \end{pmatrix}$$

where each entry is a diagonal 3×3 matrix, $h = 2\pi/N$, and the blank spaces represent zeros. The entries in the top right and bottom left corners incorporate the periodic boundary conditions on the PDE. Using forward Euler stepping as the temporal discretization yields the following representation for the Newton descent PDE

$$\hat{A}\delta\tilde{x} = \delta\tau(\lambda v - \tilde{v}), \tag{47}$$

where

$$\hat{A} = D - \lambda \operatorname{diag}[A_1, A_2, \ldots, A_N]. \tag{48}$$

Here, the A_k are the matrices $\partial v_i/\partial x_j|_{x=\tilde{x}_k}$. The velocity vector at each point on the loop is given by $v = (v_x, v_y, 1)$, where v_x and v_y are approximated using a cubic interpolant. The entries in the A_k are approximated using forward finite differencing. However, care must be taken so that the differencing is done in the same way for all three coordinates. Each block A_k is given by

$$A_k = \begin{pmatrix} \frac{dv_x}{dx} & \frac{dv_x}{dy} & \frac{dv_x}{dt} \\ \frac{dv_y}{dx} & \frac{dv_y}{dy} & \frac{dv_y}{dt} \\ 0 & 0 & 1 \end{pmatrix}$$

where $k = 1, 2, \ldots, N$. The first two columns are computed in the usual way,

$$\frac{dv_x}{dy} \approx \frac{v_x(x, y+\epsilon, t) - v_x(x, y, t)}{\epsilon}, \tag{49}$$

for example (in practice, $\epsilon = 1 \times 10^{-7}$ was used). However, $v_x(x, y, t_k + \epsilon) = v_x(x, y, t_k) + \epsilon[v_x(x, y, t_{k+1}) - v_x(x, y, t_k)] \equiv v_{x,k} + \epsilon(v_{x,k+1} - v_{x,k})$. Thus,

$$\frac{\partial v_x}{\partial t} \approx \frac{v_{x,k} + \epsilon(v_{x,k+1} - v_{x,k}) - v_{x,k}}{\epsilon} = v_{x,k+1} - v_{x,k}. \tag{50}$$

Now that everything is setup, Eq. 47 is inverted in order to obtain the update to the coordinates $\delta\tilde{x}$ and the process is repeated until convergence is obtained. However, there is still the $\delta\tau$ term in Eq. 47. This is the "damping parameter". How one needs to vary this term is system-dependent. But the idea is that it starts out small and as the residual ($||\lambda v - \tilde{v}||_2$) decreases, it is steadily increased up to $\delta\tau = 1$, at which point the quadratic convergence (or faster) of the Newton-Raphson method is recovered.

Finally, it should be mentioned that it is absolutely necessary that the smoothness of the loop is maintained throughout the computation, otherwise sawtooth oscillations begin to set in and the method breaks down. One way to safeguard against this happening is to Fourier transform the loop every so often, throw out the high frequency modes, and inverse transform the loop back into the phase space. It is a good idea to do this once the solution has converged as well. As always, if other symmetries exist in the flow besides translational invariance, these will need to be quotiented out too.

CHAPTER IV

TRANSITION TO WEAK TURBULENCE

In this chapter we describe the transition to 2D turbulence in our model system as the value of the control parameter A is increased using different numbers of magnet pairs. Unlike many shear flows in 3D which transition directly from laminar flow to turbulence, here we find a rather complicated sequence of transitional flow states whose temporal complexity changes in a rather non-monotonic fashion before a turbulent flow is eventually established. Several bifurcation analyses similar to this have been done over the years [43, 45], however these studies were carried out using truncated models of the Navier-Stokes equation, whereas we are computing these solutions and their bifurcations using a direct numerical simulation of the full PDE. In Section 4.4 we examine how many of the flow patterns we find in the 4-magnet case (Section 4.1) change as the length of the magnets L_x is varied as well as what new solutions appear. We conclude the Chapter with a discussion of the weakly turbulent regime.

4.1 Four-magnet array

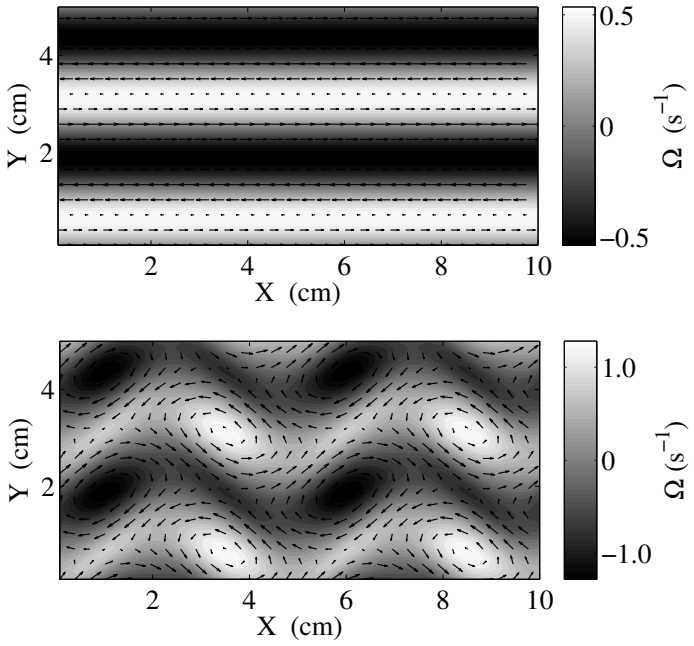

(a)

(b)

Figure 4: Laminar flow L at $A = 0.1$ s^{-2} (a) and spatially modulated flow M at $A = 0.250$ s^{-2} (b). Velocity field (arrows) is overlayed on top of the vorticity field (grayscale).

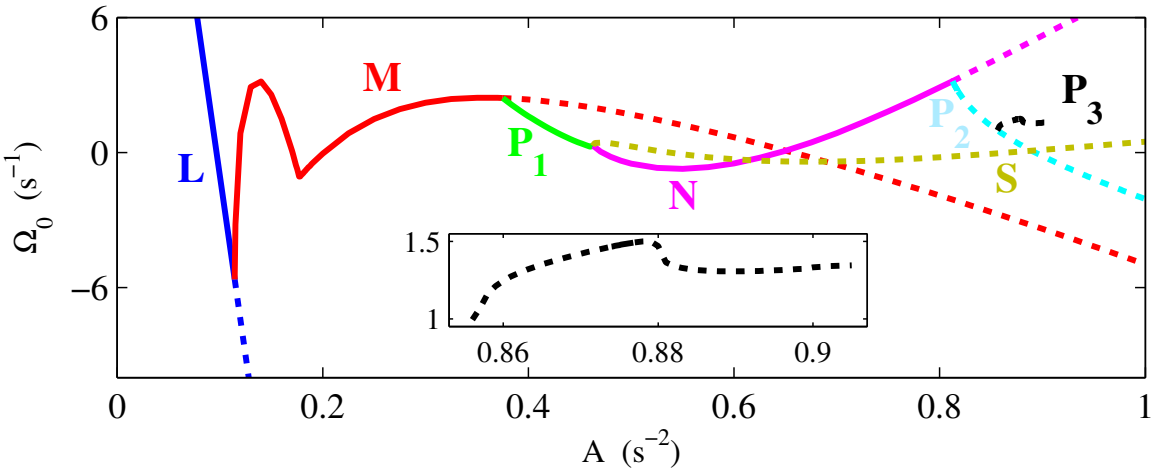

Figure 5: Bifurcation diagram. The relative vorticity magnitude $\Omega_0 \equiv \|\Omega - \Omega_L\|_2 - cA$ is shown, where c is a constant chosen to separate the various branches of the diagram for visualization purposes. Solid and dotted lines denote stable and unstable states, respectively. Periodic orbits are represented by their time-averaged values. Inset shows the region where the P_3 branch exists.

The Kolmogorov flow profile describes a laminar solution of the vorticity equation (17) with the symmetry of the driving force: continuous translational symmetry in the x direction and discrete translational symmetry in the y direction. The problem also possesses two additional discrete symmetries (rotation by 180 degrees about a vertical axis and a flip about x (or y) axis combined with the change in the sign of vorticity), but these will not play an important role in the subsequent discussion.

In order to perform a linear stability analysis of this flow pattern, the streamfunction is expanded as a Fourier series.

$$\Psi(x, y, t) = \sum_{mn} a_{mn}(t) X_m(x) Y_n(y) \tag{51}$$

where $X_m(x) = \exp(2m\pi i x/L_x)$ and $Y_n(x) = \exp(2n\pi i y/L_y)$. Using this expression to substitute into the PDE (17) for $\Omega = -\nabla^2\Psi$ and $\mathbf{u} = (\partial_y\Psi, -\partial_x\Psi)$ and projecting the resulting equation onto the Fourier modes yields a set of ODEs for the coefficients $a_{mn}(t)$'s. Setting these equations equal to zero and solving this system then gives the

steady state laminar solution for the vorticity (referred to simply as L below)

$$\Omega_L = \frac{A}{\alpha + \left(\frac{2\pi}{L_y}\right)^2 \nu} \sin \frac{2\pi y}{L_y} \tag{52}$$

and features straight alternating shear bands which reflect the geometric arrangement of the magnets (see Fig. 4(a)). Linearizing the system and solving for the values of A where the determinant of the Jacobian vanishes yields two real, positive solutions. The smaller of the two gives the value of A for which one of its eigenvalues first changes sign or equivalently where the laminar state becomes unstable. For our choice of parameters, this linear stability analysis predicts the flow profile to be stable for $A \leq 0.1145$ s^{-2}. This is confirmed by the results of our numerical simulations summarized in Fig. 5, which shows all stable and unstable solutions that have been computed using a Jacobian-free Newton-Krylov solver [65] for $A \leq 1$ s^{-2}.

At $A \approx 0.1145$ s^{-2} the laminar flow L loses stability through a supercritical pitchfork bifurcation and is replaced with its steady, spatially modulated version. As A is increased, the distortion of the shear bands increases and they are gradually replaced with a periodic array of counter-rotating vortices. Dovzhenko *et al.* were the first to draw a diagram describing this bifurcation based on their theoretical calculations. They then confirmed their analytical results experimentally [37]. This spatially modulated shear flow (denoted M and shown in Fig. 4(b)) eventually undergoes a supercritical Hopf bifurcation and loses stability at $A \approx 0.3750$ s^{-2}.

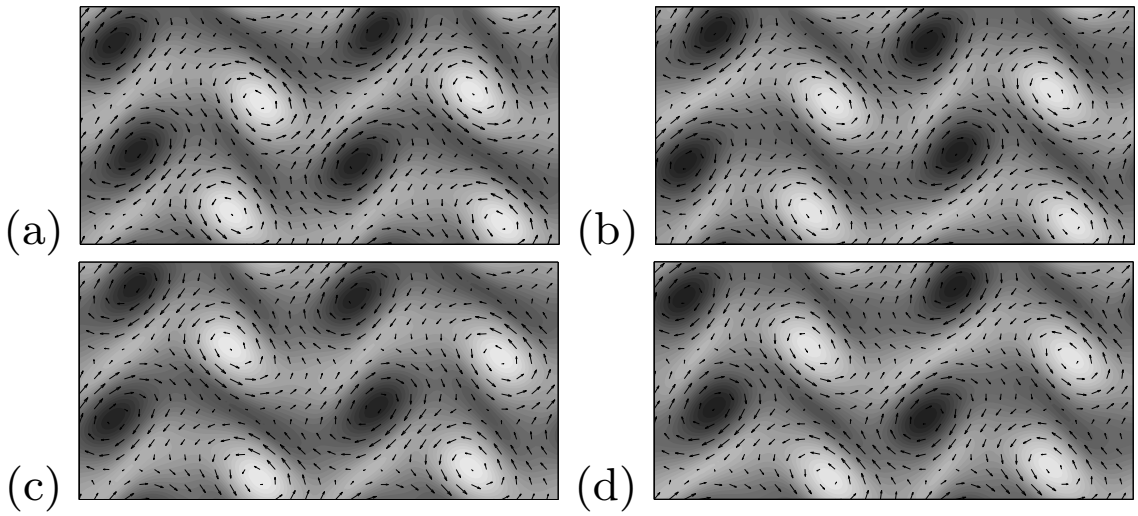

Figure 6: Time-periodic flow P_1 at $A = 0.428$ s^{-2} and (a) t=0, (b) t=T/4, (c) t=T/2, (d) t=3T/4 with $T = 365.83$ s. The same color bar as in Fig. 8(a) is used here. System size is 10 cm $\times$ 5 cm.

At this point the first stable, time-periodic solution (denoted P_1) appears. Four snapshots of this state at different phases of the oscillation are shown in Fig. 6. The strength ε of the time-dependent perturbation Ψ as a function of A is shown in Fig. 7 along with its base frequency $\omega_1 = 2\pi/T$. Batchaev and Dovzhenko were the first (and, to date, the only) group to experimentally observe a supercritical Hopf bifurcation from the modulated state using a four magnet setup [10].

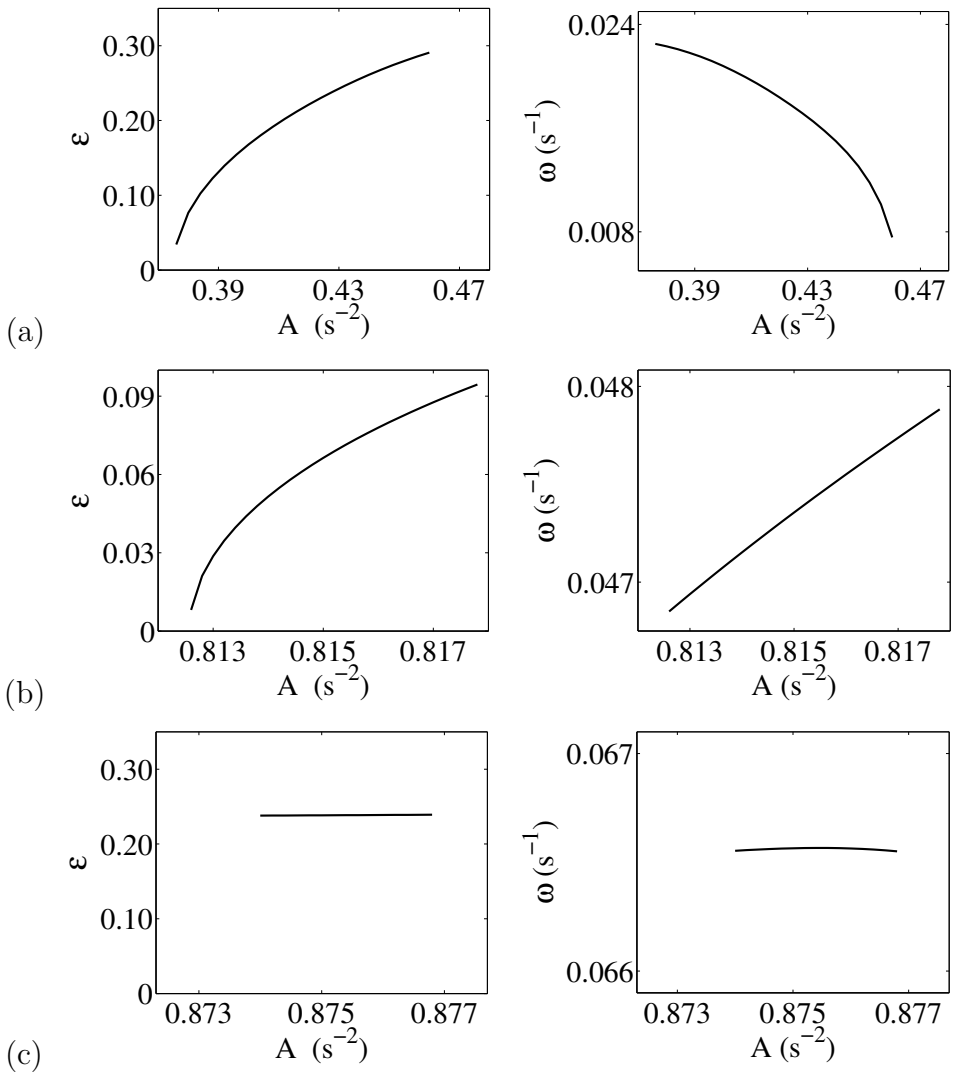

Figure 7: The perturbation amplitude ε and frequency $\omega_1 = 2\pi/T$ of the time-periodic flows P_1 (a), P_2 (b), and P_3 (c). Only the ranges of A are shown where these flows exist and are stable.

As expected for a state created via a Hopf bifurcation, the amplitude of oscillation for P_1 grows as a square root of the distance to the bifurcation point (see Fig. 7(a)). The frequency of oscillations $\omega_1 = 2\pi/T$ decreases (and the period T increases) monotonically with A until the oscillatory state is destroyed as a result of an infinite-period bifurcation at $A \approx 0.4635$ s^{-2}.

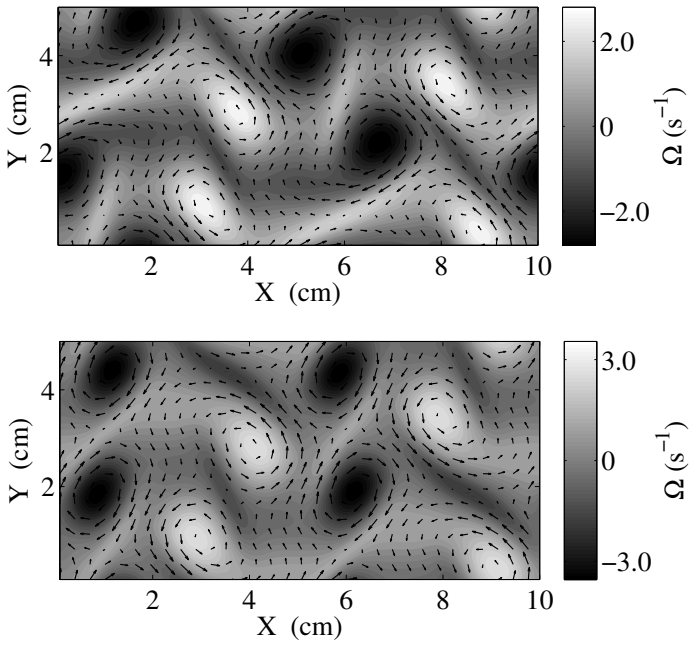

Figure 8: Stable steady flow N (a) and unstable steady flow S (b) at $A = 0.750$ s^{-2}.

At this point two steady solutions are created, a stable node N and a saddle S (shown in Figs. 8(a) and (b), respectively). The corresponding flows are quite similar (a disordered array of four clockwise and four counterclockwise vortices) and possess a relatively low symmetry: just like P_1, they are symmetric with respect to a shift $(x, y) \to (x + L_x/2, y + L_y/2)$.

The numerical solution of (17) follows the stable branch N as A increases further until the corresponding steady flow again develops an oscillatory instability (also a supercritical Hopf) at $A \approx 0.8125$ s^{-2}, giving rise to another time-periodic flow P_2, shown in Fig. 9. The amplitude and frequency of this flow are shown in Fig. 7(b). This state is stable in a fairly narrow range of A and, at $A \approx 0.8180$ s^{-2}, P_2 undergoes a secondary supercritical Hopf bifurcation giving rise to a quasi-periodic flow (denoted QP) which, after another Hopf bifurcation, transitions to aperiodic flow around $A \approx 0.865$ s^{-2}.

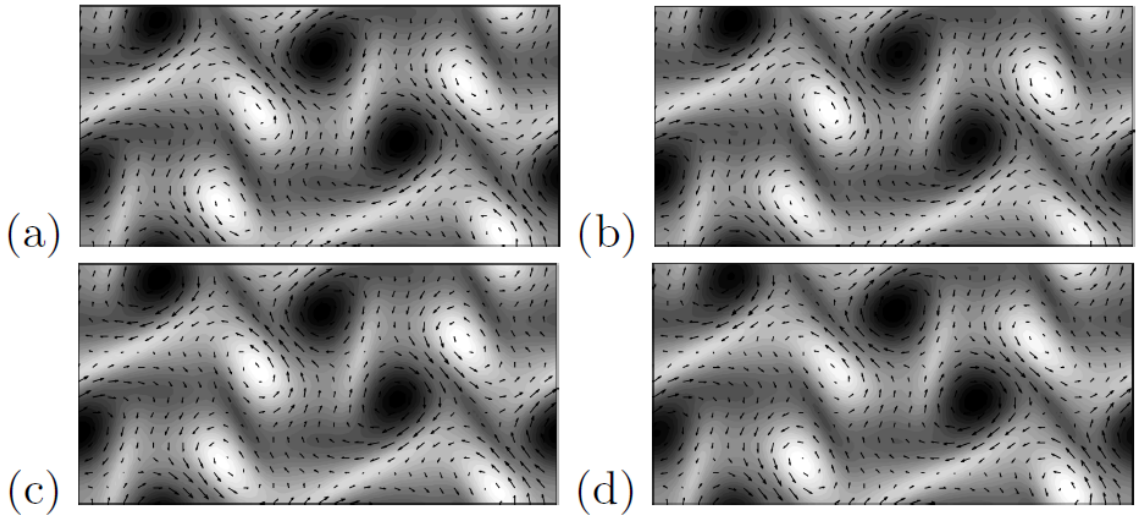

Figure 9: Time-periodic flow P_2 at $A = 0.817$ s^{-2} and (a) t=0, (b) t=T/4, (c) t=T/2, (d) t=3T/4 with $T = 131.76$ s. The same color bar as in Fig. 8(a) is used here. System size is 10 cm $\times$ 5 cm.

At $A \approx 0.8740$ s^{-2}, a third stable, time-periodic state P_3, shown in Fig. 10, is created via a subcritical Hopf bifurcation. The corresponding flow does not respect any of the symmetries of the system and is only stable for a very narrow range of A before it undergoes a subcritical pitchfork bifurcation at $A \approx 0.8768$ s^{-2}. Its amplitude and frequency are effectively constant throughout its range of stability as Fig. 7(c) illustrates.

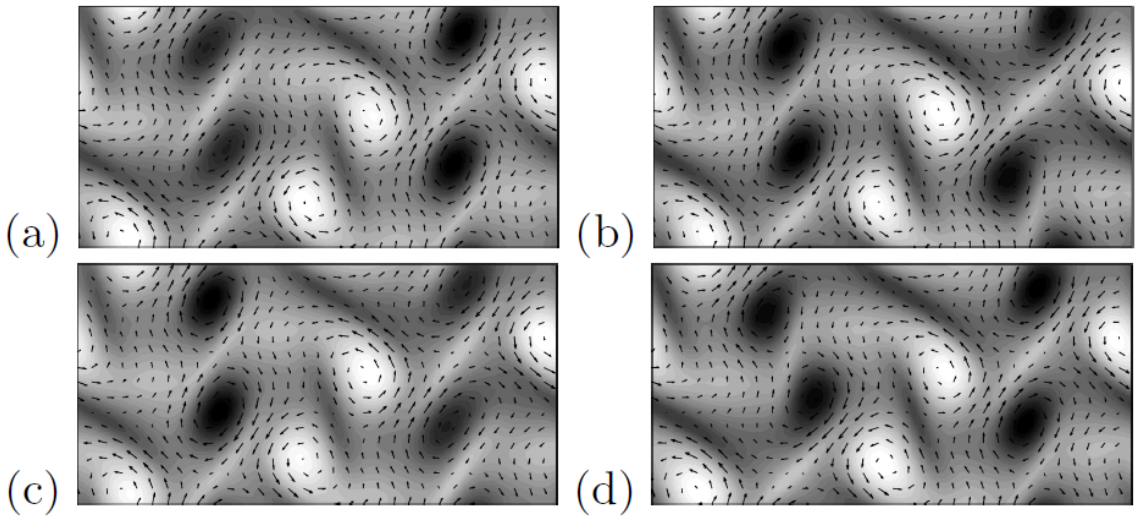

Figure 10: Time-periodic flow P_3 at $A = 0.875$ s^{-2} and (a) t=0, (b) t=T/4, (c) t=T/2, (d) t=3T/4 with $T = 94.39$ s. The same color bar as in Fig. 8(b) is used here. System size is 10 cm $\times$ 5 cm.

Increasing A further, we find another narrow aperiodic window before the flow returns to quasi-periodic behavior at about $A \approx 0.885$ s^{-2}. Finally, the flow once again becomes aperiodic at $A \approx 0.980$ s^{-2}. The temporally aperiodic (or chaotic) flows we find are weakly turbulent.

We conclude this section with a discussion of the Reynolds number

$$Re = w\nu^{-1}\|\langle \mathbf{v} \rangle_t\|_2 \tag{53}$$

characterizing the solutions described above. As Fig. 11 shows, Re varies linearly with A in different flow regimes. The slope is roughly the same for almost all flows, except the laminar flow L, for which it is much steeper. Indeed, a quick inspection of the vorticity fields shows that, beyond L, the flow is dominated by structures oriented at an angle $\theta \approx 45$ degrees to the x direction, so that the slope can be estimated as $Re/A \sim (k/\sin\theta)^{-4}\nu^{-2} \approx 47.5$ s^2. For the laminar flow we find instead $Re/A \sim k^{-4}\nu^{-2} \approx 190$ s^2. Both estimates are in reasonable agreement with the numerical data presented in Fig. 11.

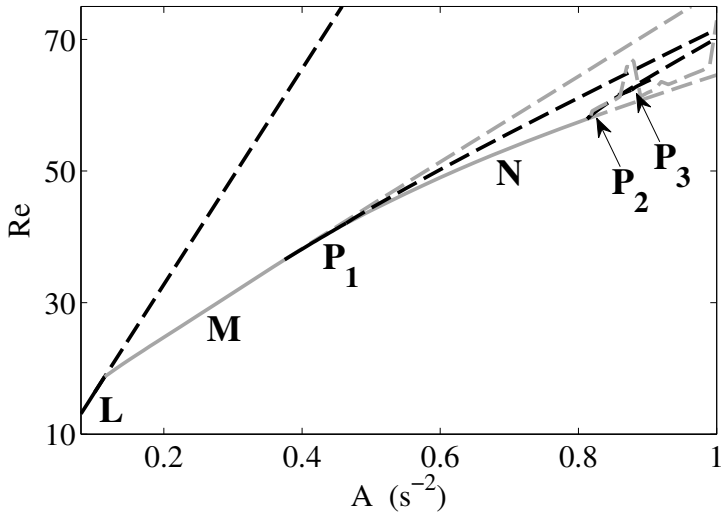

Figure 11: Relationship between the Reynolds number and the forcing strength A. Solid lines denote stable states and dashed lines denote unstable ones.

4.2 Six-magnet array

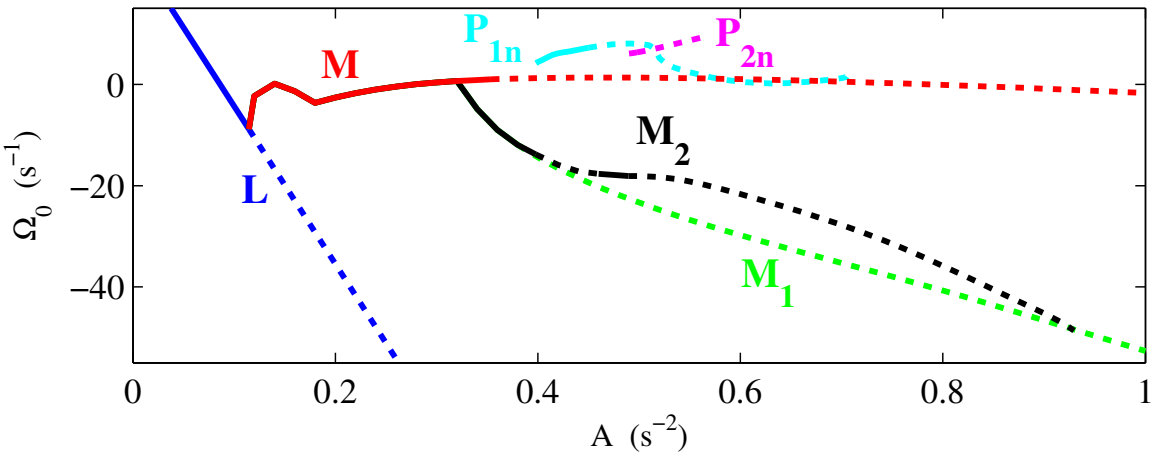

Figure 12: Bifurcation diagram. The relative vorticity magnitude $\Omega_0 \equiv \|\Omega - \Omega_L\|_2 - cA$ is shown, where c is a constant chosen to separate the various branches of the diagram for visualization purposes. Solid and dotted lines denote stable and unstable states, respectively and periodic orbits are represented by their time-averaged values.

(a)

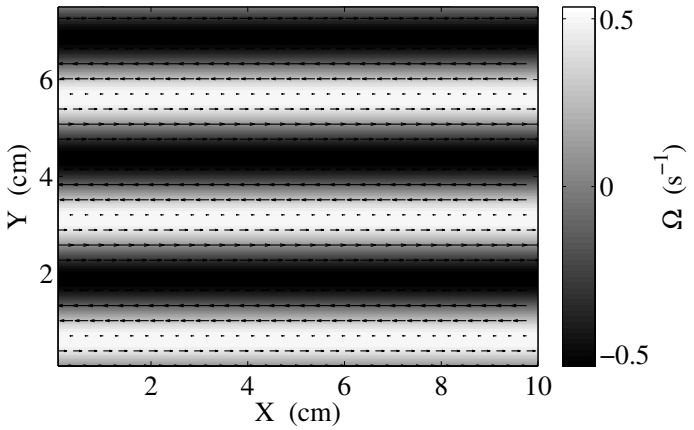

(b)

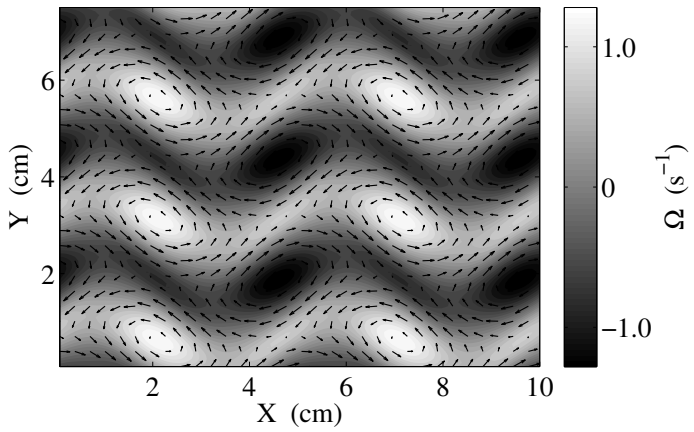

Figure 13: Laminar flow L at $A = 0.100$ s^{-2} (a) and spatially modulated flow M at $A = 0.250$ s^{-2} (b).

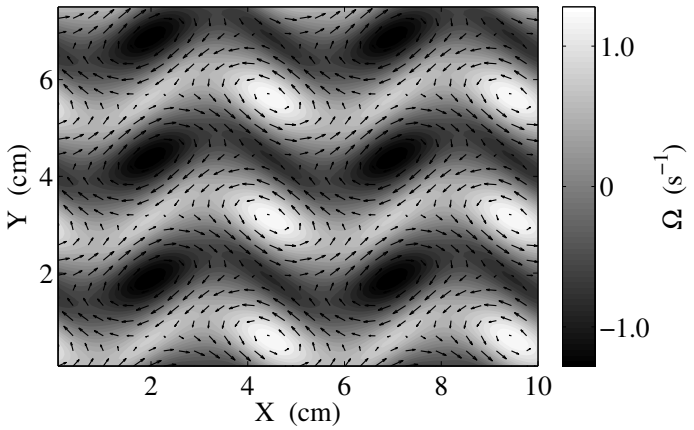

(a)

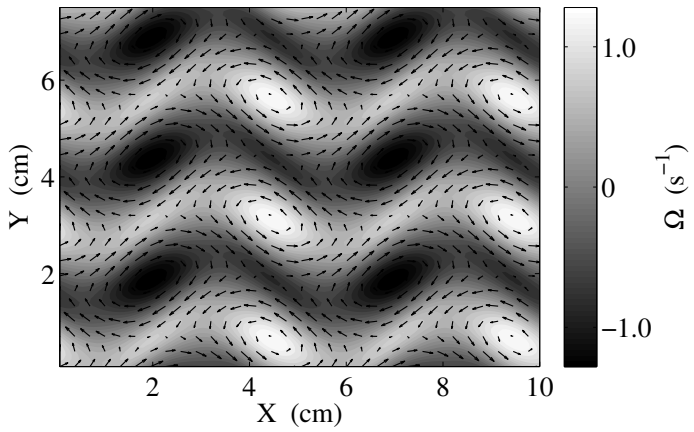

(b)

Figure 14: Spatially modulated flow M_1 at $A = 0.250\ \mathrm{s}^{-2}$ (a) and spatially modulated flow M_2 at $A = 0.250\ \mathrm{s}^{-2}$ (b).

As in the four-magnet case, at $A \approx 0.1145\ \mathrm{s}^{-2}$ the laminar flow L loses stability through a supercritical pitchfork bifurcation. Now instead of one, it is replaced with two seemingly identical steady flows and one that appears to be a horizontally shifted version of the other two. The latter is in fact the same flow as the modulated state (M) from Sect. 4.1 shown in Fig. 4 (b). Since this flow is periodic across any magnet pair, then it must be a solution for any system that has an even number of magnets. As A is increased, the distortion of the shear bands increases and for all three states they are gradually replaced with a periodic array of counter-rotating vortices (these are denoted M, M_1, and M_2). Despite the fact that at this point M_1 and M_2 look identical and M looks like a symmetry-related version of these two (see

Figs. 13(b) and 14) and the fact that they share the same stability eigenvalues, these properties begin to change as A is increased. Furthermore, examining the norm of the difference between any pair (with M shifted by the appropriate amount), one finds that this quantity monotonically approaches zero as A approaches the value at which the laminar state becomes unstable. So, it is clear that these three flows are indeed distinct from one another. As Fig. 15 shows, at $A = 0.350$ s^{-2} M_1 is spatially very different from M. Not shown is M_2 which, to the eye, is indistinguishable from M_1 at this value of A. Beyond this point, M undergoes a supercritical pitchfork bifurcation and loses stability at $A \approx 0.3537$ s^{-2}. As A is increased further, M_1 and M_2 begin to diverge from one another both in terms of their spatial structure as well as their eigenspectra. At $A \approx 0.3858$ s^{-2}, M_1 also loses stability through a supercritical pitchfork bifurcation. Finally, at $A \approx 0.3979$ s^{-2}, M_2 undergoes a Hopf bifurcation and becomes unstable.

(a)

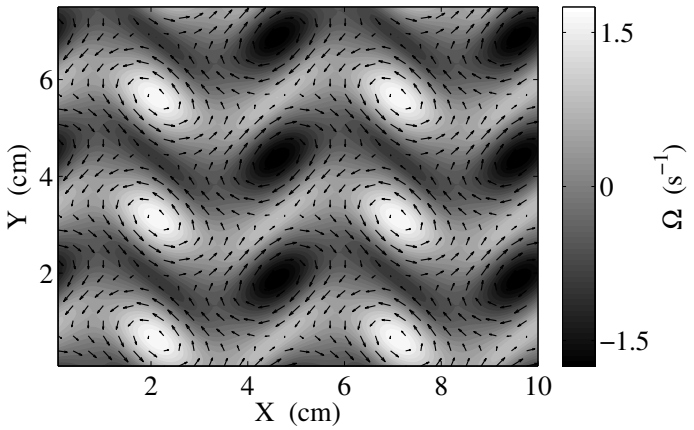

(b)

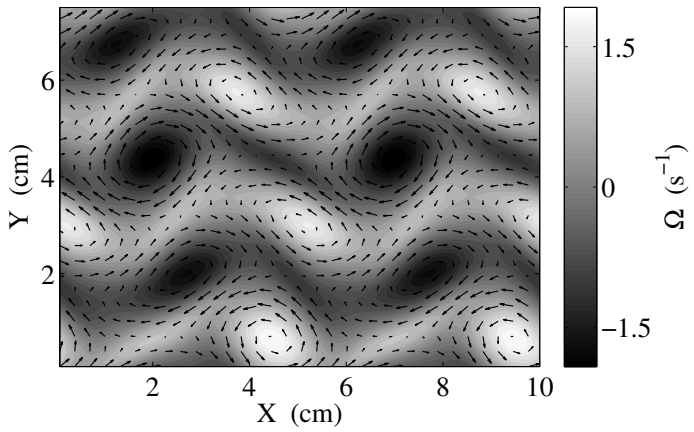

Figure 15: Spatially modulated flow M at $A = 0.350\ \mathrm{s}^{-2}$ (a) and spatially modulated flow M_1 at $A = 0.350\ \mathrm{s}^{-2}$ (b).

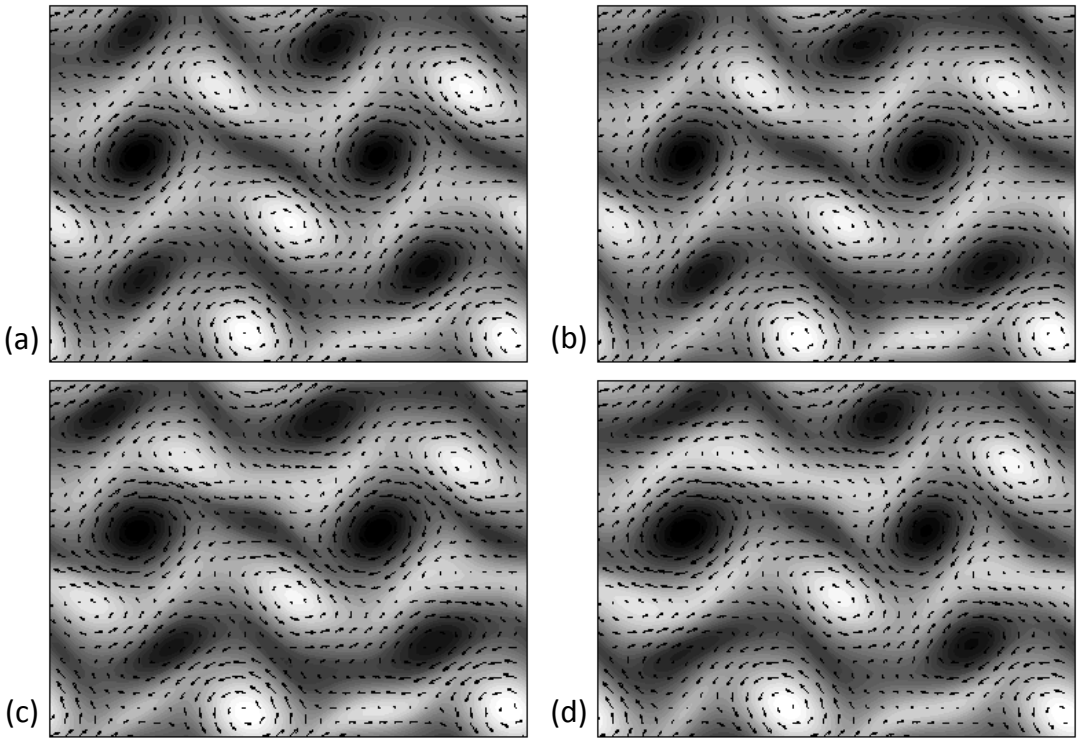

Figure 16: Time-periodic flow P_{1n} at $A = 0.420$ s^{-2} and (a) t=0, (b) t=T/4, (c) t=T/2, (d) t=3T/4 with $T = 53.20$ s. System size is 10 cm $\times$ 7.5 cm.

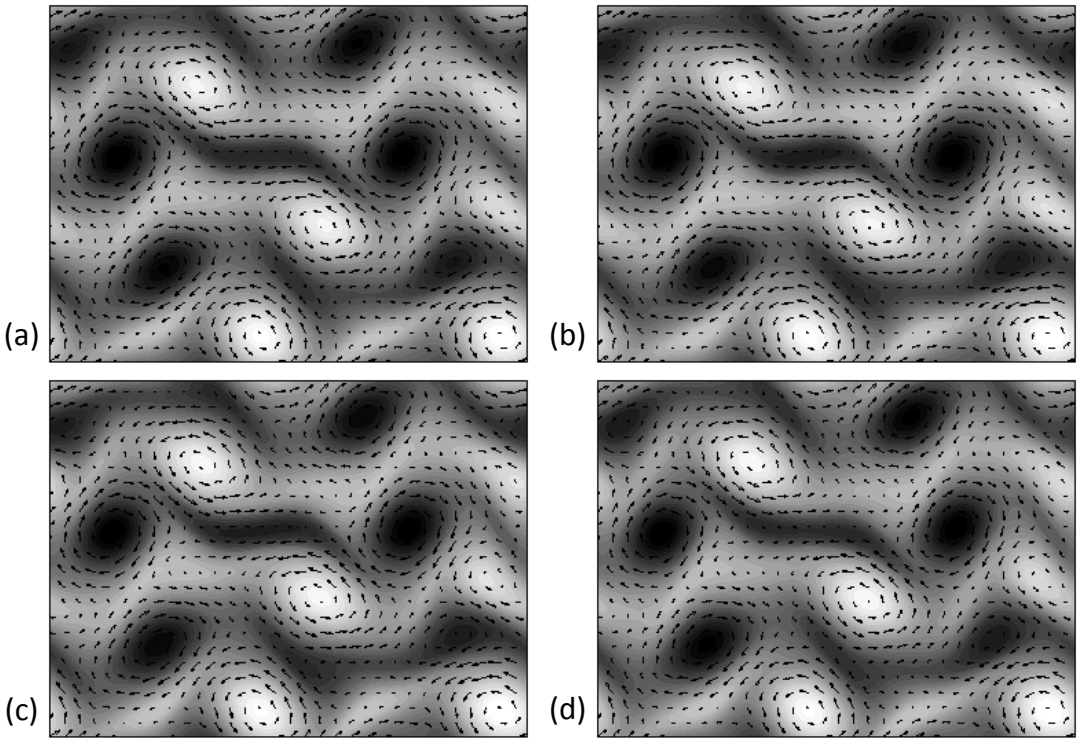

Figure 17: Time-periodic flow P_{2n} at $A = 0.490$ s^{-2} and (a) t=0, (b) t=T/4, (c) t=T/2, (d) t=3T/4 with $T = 33.45$ s. System size is 10 cm $\times$ 7.5 cm.

At this point, there emerges this system's first stable, time-periodic flow (denoted P_{1n}). Since this flow could not be continued in L_x for values smaller than $A = 0.3979$, it would seem that it emerged from the Hopf bifurcation of M_2. However, from what Fig. 12 shows, this does not appear to be the case as it is not connected to the M_2 branch. Four snapshots of this solution at different times of the oscillatory motion are shown in Fig. 16. This state then undergoes a secondary supercritical Hopf bifurcation at $A \approx 0.4471$ s^{-2} and the overall flow becomes quasiperiodic and then becomes aperiodic around $A \approx 0.452$ s^{-2}. However, at $A \approx 0.4643$ s^{-2} the previously unstable state, M_2, regains its stability through a subcritical pitchfork bifurcation. As A is increased further, it once again becomes unstable through yet another Hopf bifurcation at $A \approx 0.4896$ s^{-2}. Here, another time-periodic solution emerges, denoted P_{2n} and shown in Fig. 17. But, once again, Fig. 12 indicates that P_{2n} does not

appear to come from this Hopf bifurcation. More than likely both Hopf bifurcations of M_2 are subcritical, and there is an unstable branch connecting it to the stable branches of both P_{1n} and P_{2n}. P_{2n} remains stable only within a narrow range of A before undergoing a secondary Hopf bifurcation $A \approx 0.4953$ s^{-2} which gives rise to another quasiperiodic flow that quickly transitions to an aperiodic flow at $A \approx 0.500$ s^{-2}.

4.3 Eight-magnet array

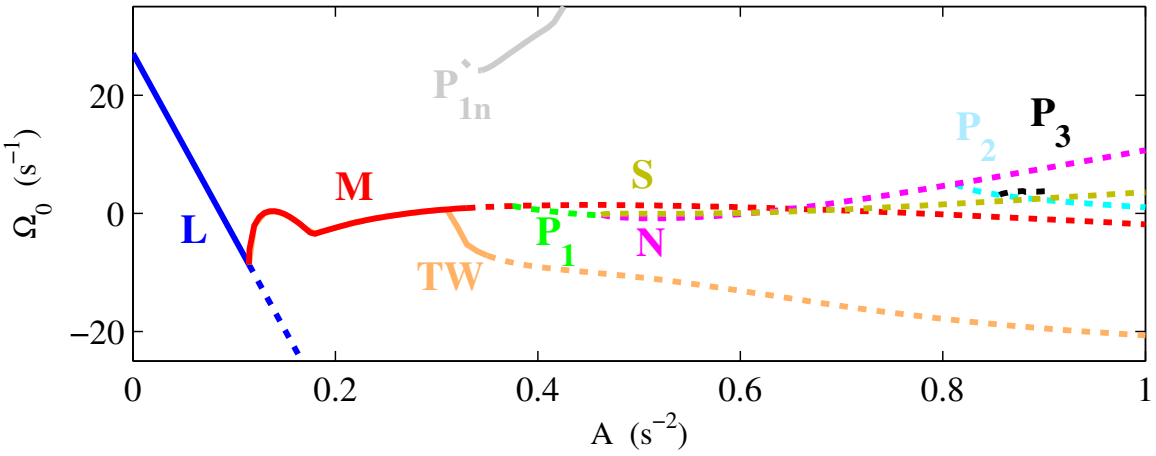

Figure 18: Bifurcation diagram. The relative vorticity magnitude $\Omega_0 \equiv \|\Omega - \Omega_L\|_2 - cA$ is shown, where c is a constant chosen to separate the various branches of the diagram for visualization purposesown. Solid and dotted lines denote stable and unstable states, respectively and periodic orbits are represented by their time-averaged values.

(a)

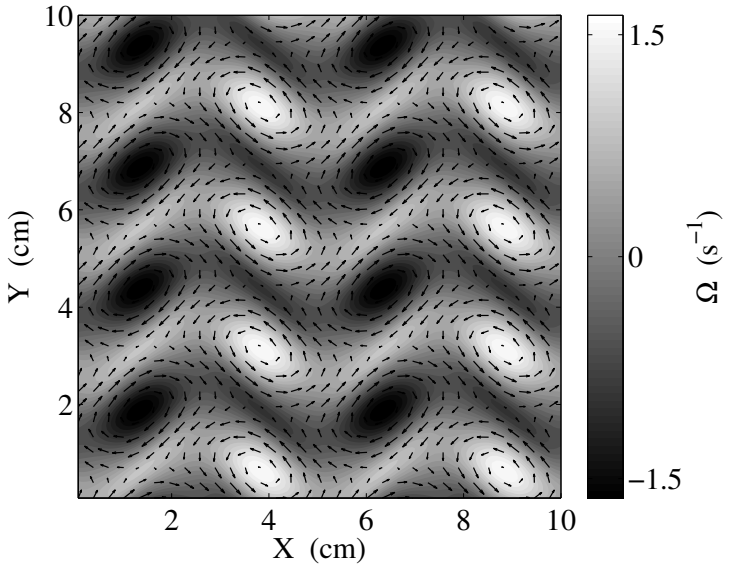

(b)

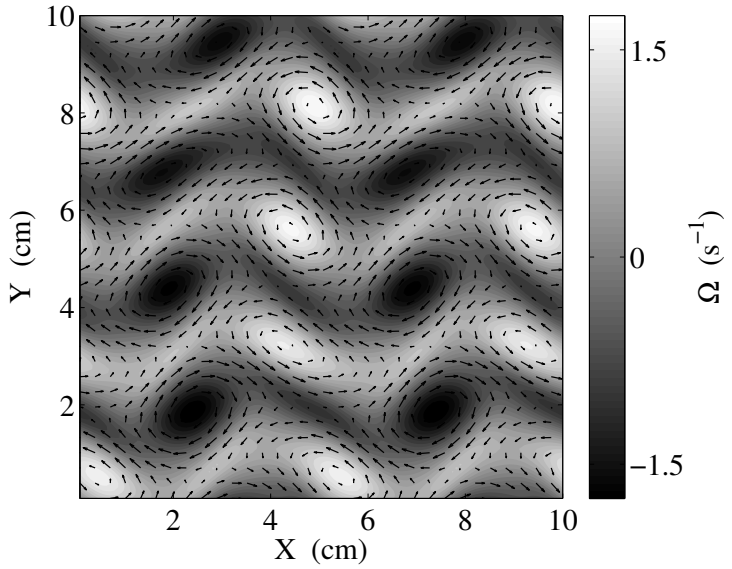

Figure 19: Spatially modulated flow M at $A = 0.325$ s^{-2} (a) and traveling wave flow TW at $A = 0.325$ s^{-2} (b).

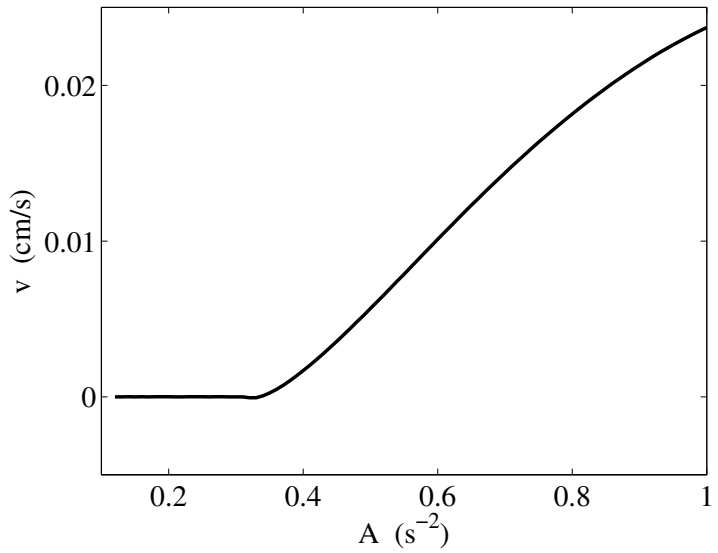

Figure 20: Velocity of the comoving frame for TW as a function of the driving force amplitude.

As in the four-magnet and six-magnet case, at $A \approx 0.1145$ s^{-2} the laminar flow L loses stability through a supercritical pitchfork bifurcation. And, once again, we find a different set of states as a result of this bifurcation. Two fixed points emerge that seem to be symmetry-shifted versions of one another. As in the six-magnet case, one of these is the state M from Sect. 4.1 as this state is a solution for every system with an even number of magnets. In fact, all of the solutions from Sect. 4.1 are solutions for this system as well (or any system where the number of magnets is a multiple of four), however their stability has changed – with the exception of M and L, they are all now unstable over the entire range of A where they exist (see Fig. 18). As A is increased, the distortion of the shear bands increases and for both fixed points, they are gradually replaced with a periodic array of counter-rotating vortices, but to the eye they still appear to be symmetry-shifted versions of one another and they still share the same set of stability eigenvalues. As A is increased further, however, they begin to diverge from one another both in terms of their spatial profile as well as their stability properties. These two states are denoted M and TW and are shown in

Fig. 19. Near onset, TW appears to be a fixed point, but as A is increased it begins to acquire an overall translation of the pattern in time. This is the first system in which a traveling wave solution has been found (albeit a *very* slowly moving one), and the dependence of the velocity of the pattern's reference frame on A is shown in Fig 20. M loses stability through a pitchfork bifurcation at $A \approx 0.3284$ s^{-2}, and TW becomes unstable through a Hopf bifurcation at $A \approx 0.3438$ s^{-2}. There is also a time-periodic solution, denoted P_{1n} and shown in Fig. 21, that is stable for 0.3444 s^{-2} $\lesssim A \lesssim$ 0.4350 s^{-2}. It becomes unstable for smaller values of A through a pitchfork bifurcation.

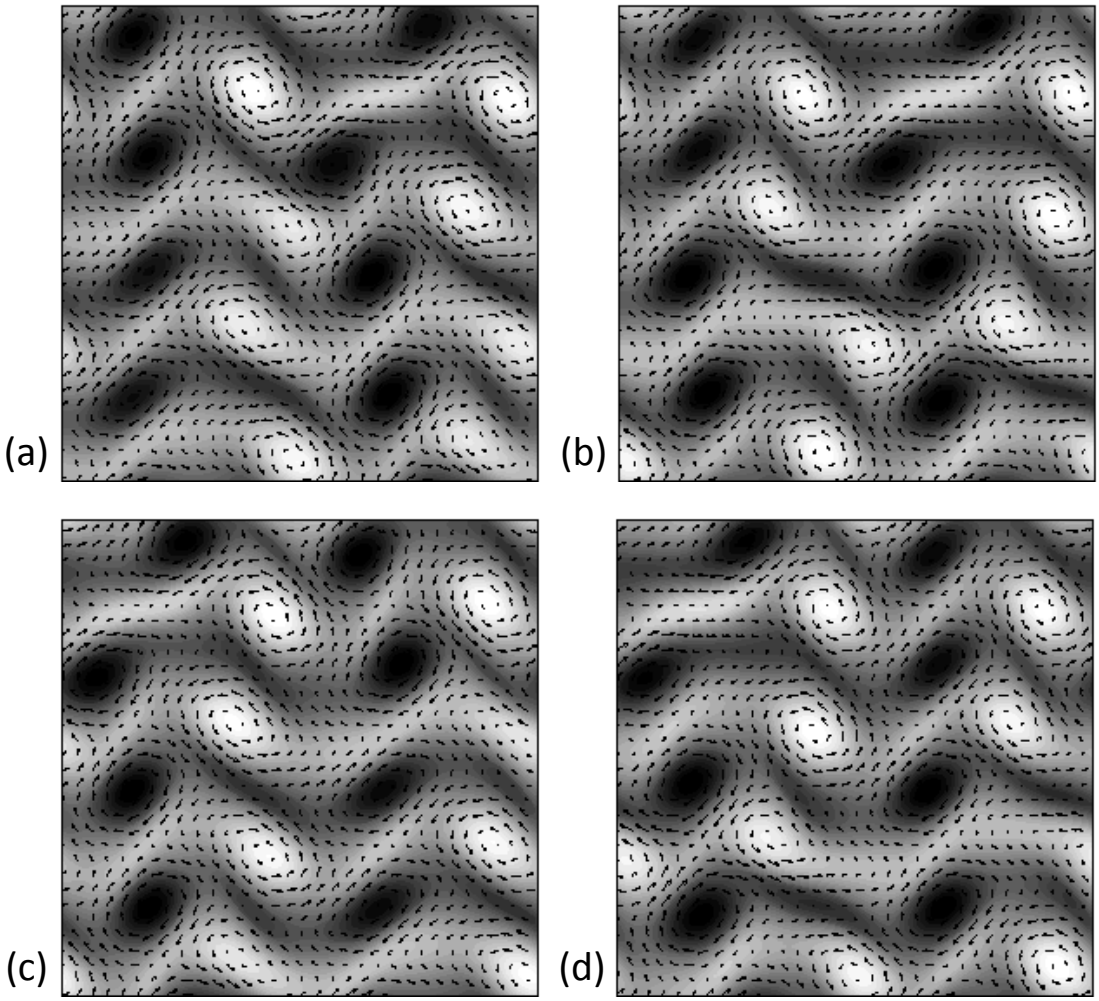

Figure 21: Time-periodic flow P_{1n} at $A = 0.390$ s^{-2} and (a) t=0, (b) t=T/4, (c) t=T/2, (d) t=3T/4 with $T = 207.62$ s. System size is 10 cm $\times$ 10 cm.

4.4 Variation of the system size

In this section, we take the four-magnet array from Sect. 4.1, where L_x was fixed at 10 cm, and study how the flows change as well as what new states appear as the result of varying the length of the magnets (L_x) to half the original system size up to double the system size. We also examine how their stability changes with respect to the parameter L_x. Both the stable and unstable branches of the laminar state do not undergo any bifurcations as a result of changing the system size, however their stability eigenvalues do vary as a function of L_x (see Fig. 22).

(a)

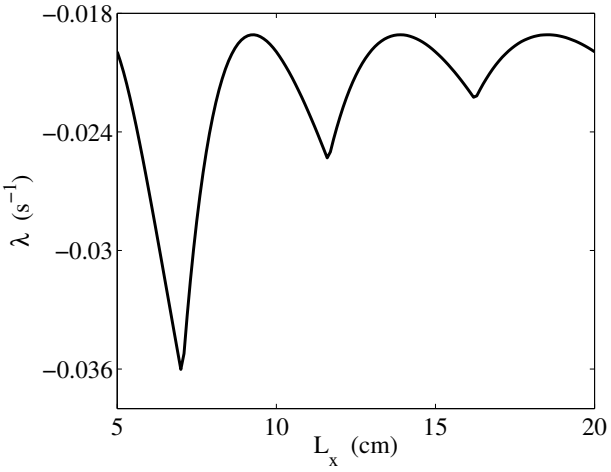

(b)

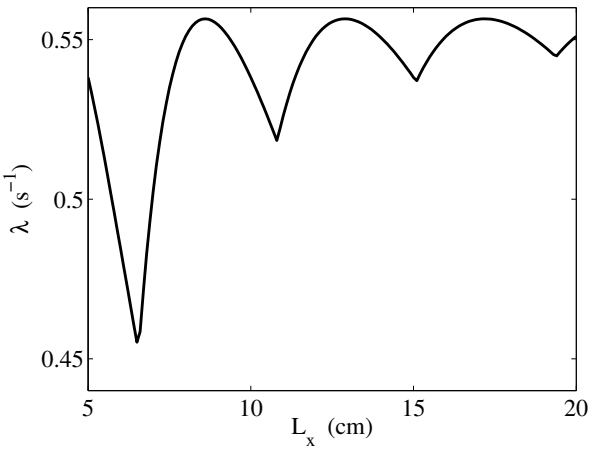

Figure 22: The leading eigenvalue of the laminar flow L as a function of system size in the region where it is (a) stable ($A = 0.100$ s^{-2}) and (b) unstable ($A = 0.500$ s^{-2}).

(a)

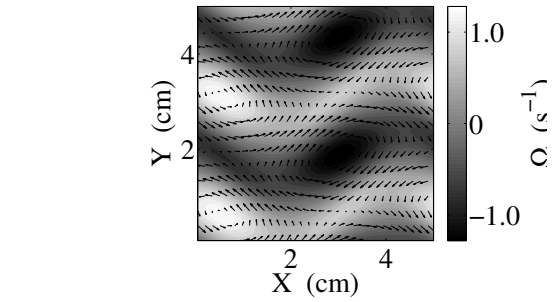

(b)

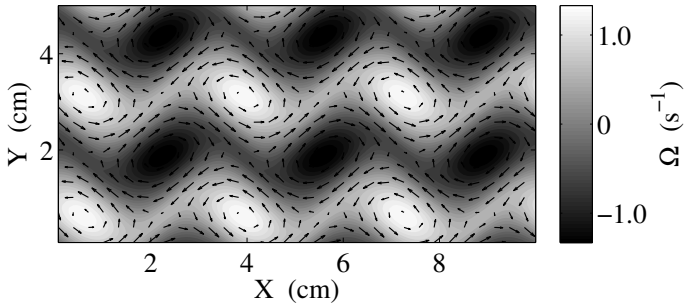

Figure 23: A one-vortex spatially modulated flow M_1 (a), $L_y = 5.0$ cm and a three-vortex spatially modulated flow M_3 (b), $L_y = 10.0$ cm. Both are at $A = 0.250$ s^{-2}

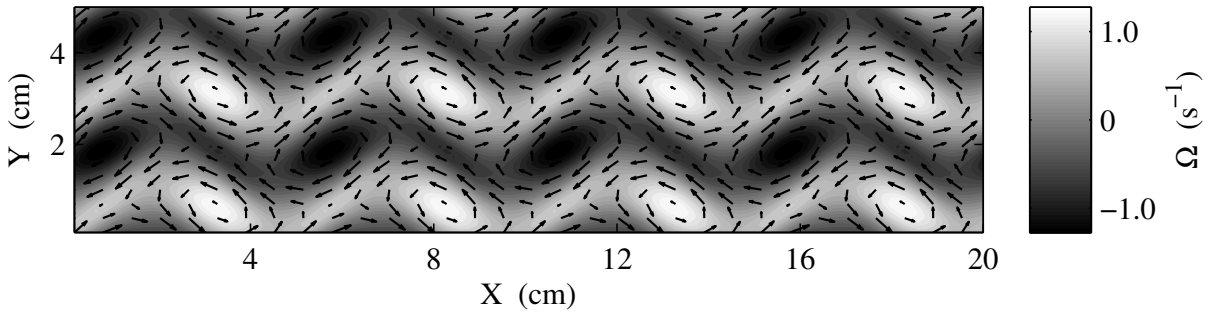

Figure 24: Four-vortex spatially modulated flow M_4 at $A = 0.250$ s^{-2}, $L_y = 20.0$ cm.

The stable, two-vortex (per shear band), modulated flow (denoted M in Sect. 4.1) on the other hand does change its stability as the system size is varied. Now we will denote this state M_2 to emphasize the fact that it is a two-vortex flow. Taking the solution for $A = 0.250$ s^{-2}, $L_x = 10.0$ cm and increasing L_x, M_2 becomes unstable

through a supercritical pitchfork bifurcation at $L_x \approx 15.92$ cm. The continuation of this unstable flow could not be extended past $L_x \approx 17.8750$ cm. This was not due to a singularity appearing in the Jacobian of the Newton solver (as would be the case as it approached a saddle-node bifurcation, for instance), but the loss of convergence of the solver appears as the flow tries to deform from a two-vortex state into a six-vortex state. Extending M_2 to smaller values of L_x, it again loses stability through a pitchfork bifurcation at $L_x \approx 5.89$ cm. Decreasing the length of the magnets further, it finally becomes an unstable laminar flow at $L_x \approx 5.53$ cm. There are also three new spatially modulated states that were found for this value of A as a result of the numerical continuation procedure in L_x. There is a one-vortex state (denoted M_1 and shown in Fig. 23 (a)) which is stable for 5.0 cm $\leq L_x \lesssim 7.96$ cm and loses stability at this upper bound through a pitchfork bifurcation. The computation of this flow could not be extended past $L_x \approx 8.937$ cm where it tries to converge to a three-vortex state. There is also a three-vortex state, M_3 shown in Fig. 23 (b), which is stable for 8.85 cm $\lesssim L_x \leq 20.0$ cm but becomes unstable for smaller values of L_x through a supercritical pitchfork bifurcation. And then it becomes an unstable laminar flow for $L_x \lesssim 8.30$ cm. Finally, there is a four-vortex state (denoted M_4 and shown in Fig. 24) which is stable for 11.84 cm $\lesssim L_x \leq 20.0$ cm but loses stability for smaller values of L_x through a supercritical pitchfork bifurcation and then becomes an unstable laminar flow for $L_x \lesssim 11.07$ cm. Even though the flow M_3 is stable for $L_x = 10.0$ cm, it was not able to be found in the computation of the bifurcation sequence in Sect. 4.1. Apparently, for larger values of L_x, this flow has a much larger basin of attraction and was then easily found and continued backwards for smaller values of L_x. So this procedure of looking for solutions for different system sizes can actually be of great use in finding solutions that may have been missed for the system size one is actually interested in. The unstable, two-vortex, modulated flow ($A = 0.800$ s^{-2}), remains unstable as the length of the magnets are varied to both smaller as well

as to larger values. And, similar to what happended with the stable version of M_2, the continuation procedure loses convergence at $L_x \approx 18.0239$ cm as the flow pattern also attempts to become a six-vortex state. These results are summarized in Fig. 25.

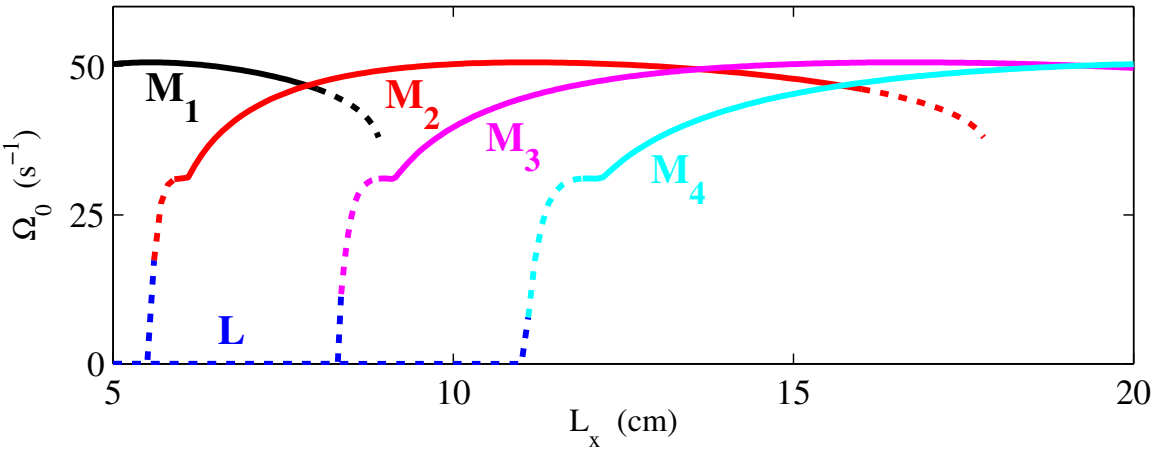

Figure 25: Bifurcation diagram ($A = 0.250$ s^{-2}). The relative vorticity magnitude $\Omega_0 \equiv \|\Omega - \Omega_L\|_2$ is shown. Solid and dotted lines denote stable and unstable states, respectively and periodic orbits are represented by their time-averaged values.

The same calculation was carried out for a value of where the equilibrium labeled N is stable as well as for the unstable saddle S from Sect. 4.1 ($A = 0.750$ s^{-2}). Not surprisingly, the stability of N changes as L_x is varied and several new periodic flows emerge. These results are summarized in Fig. 31.

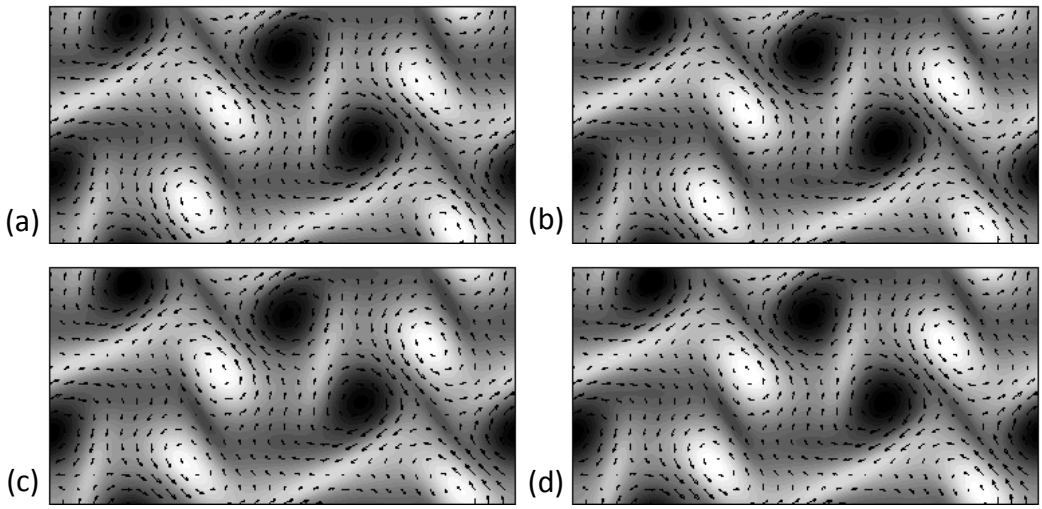

Figure 26: Time-periodic flow P_{1n} at $A = 0.750$ s^{-2} and (a) t=0, (b) t=T/4, (c) t=T/2, (d) t=3T/4 with $T = 140.15$ s. System size is 9.75 cm $\times$ 5 cm.

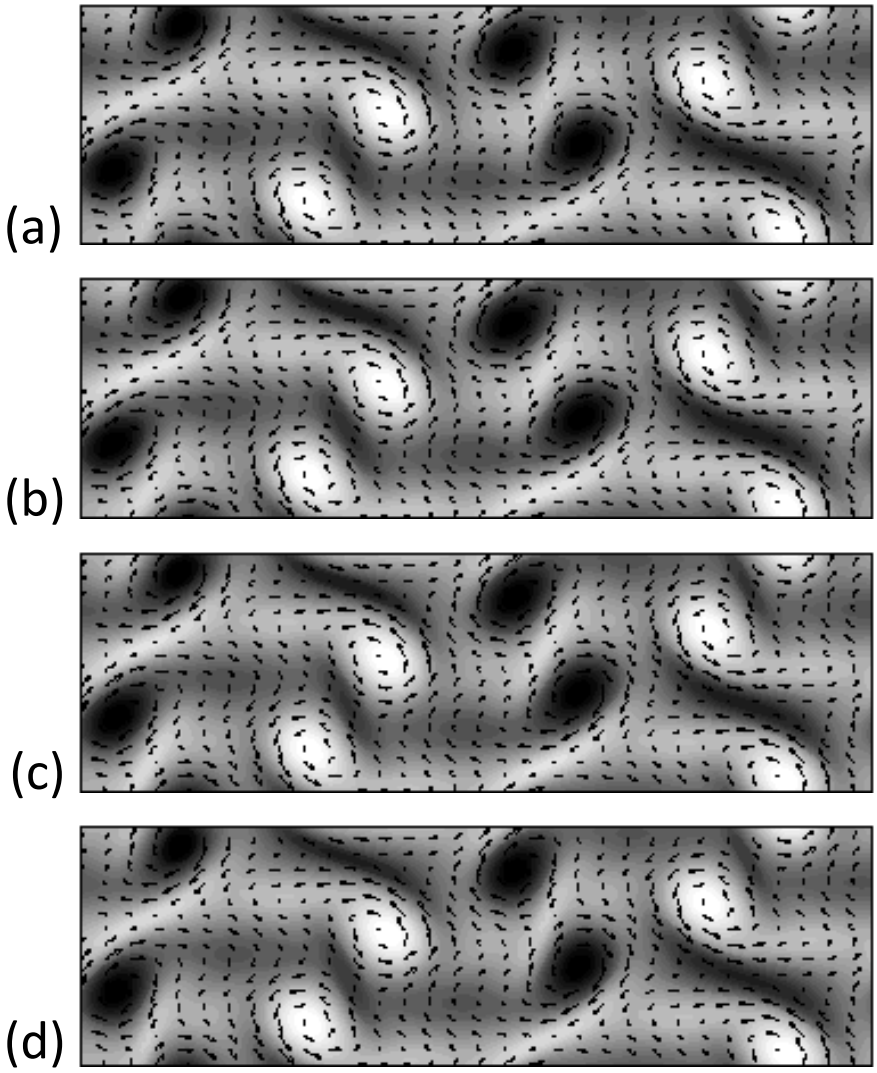

Figure 27: Time-periodic flow P_{2n} at $A = 0.750$ s^{-2} and (a) t=0, (b) t=T/4, (c) t=T/2, (d) t=3T/4 with $T = 12.34$ s. System size is 16.5 cm $\times$ 5 cm.

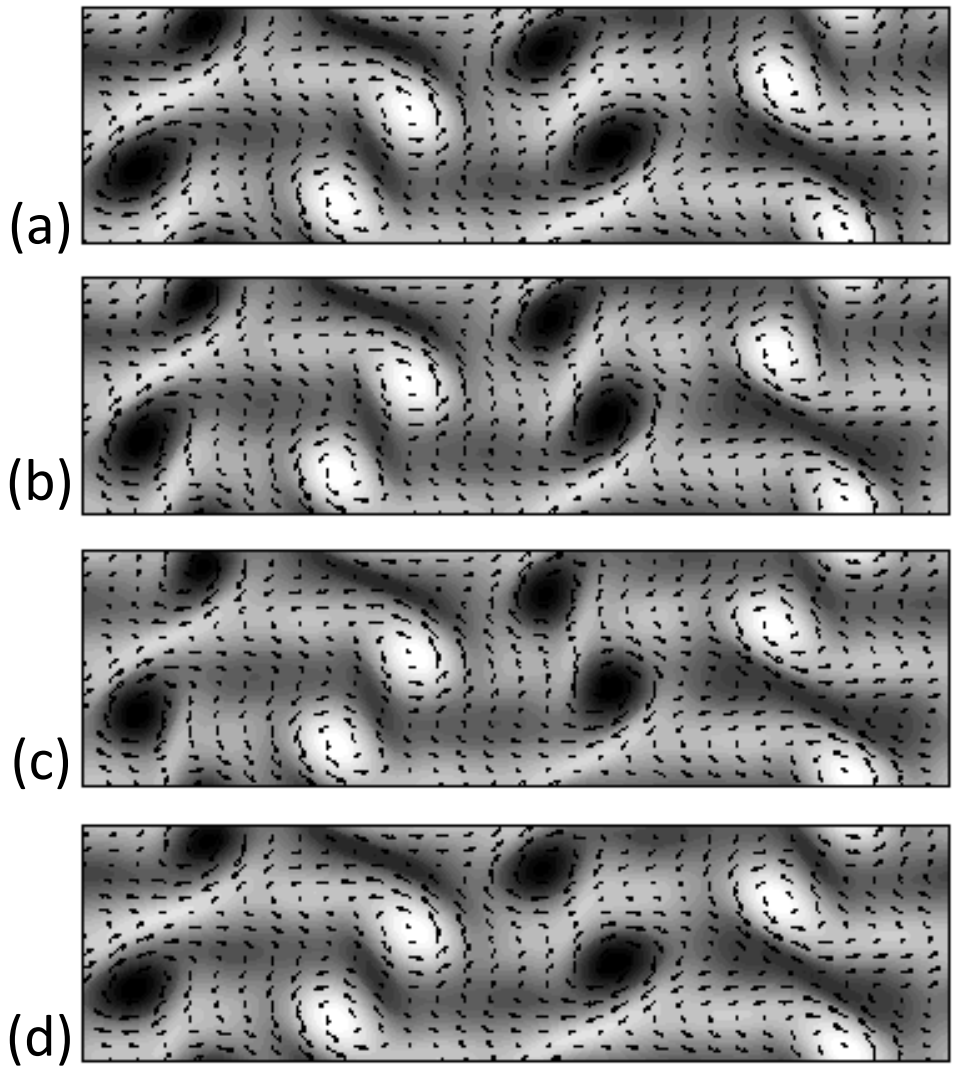

Figure 28: Time-periodic flow P_{3n} at $A = 0.750$ s^{-2} and (a) t=0, (b) t=T/4, (c) t=T/2, (d) t=3T/4 with $T = 12.38$ s. System size is 18 cm $\times$ 5 cm.

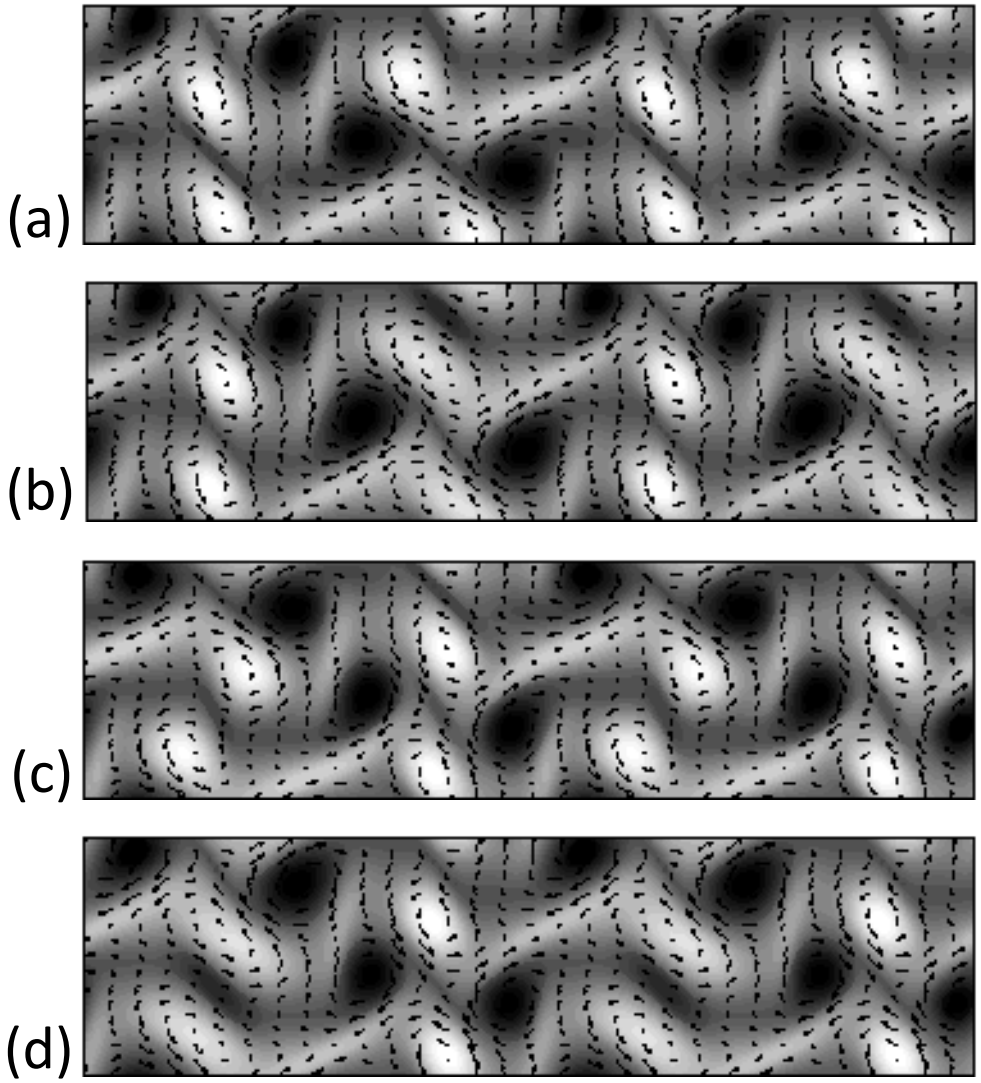

Figure 29: Time-periodic flow P_{4n} at $A = 0.750$ s^{-2} and (a) t=0, (b) t=T/4, (c) t=T/2, (d) t=3T/4 with $T = 19.53$ s. System size is 18.5 cm $\times$ 5 cm.

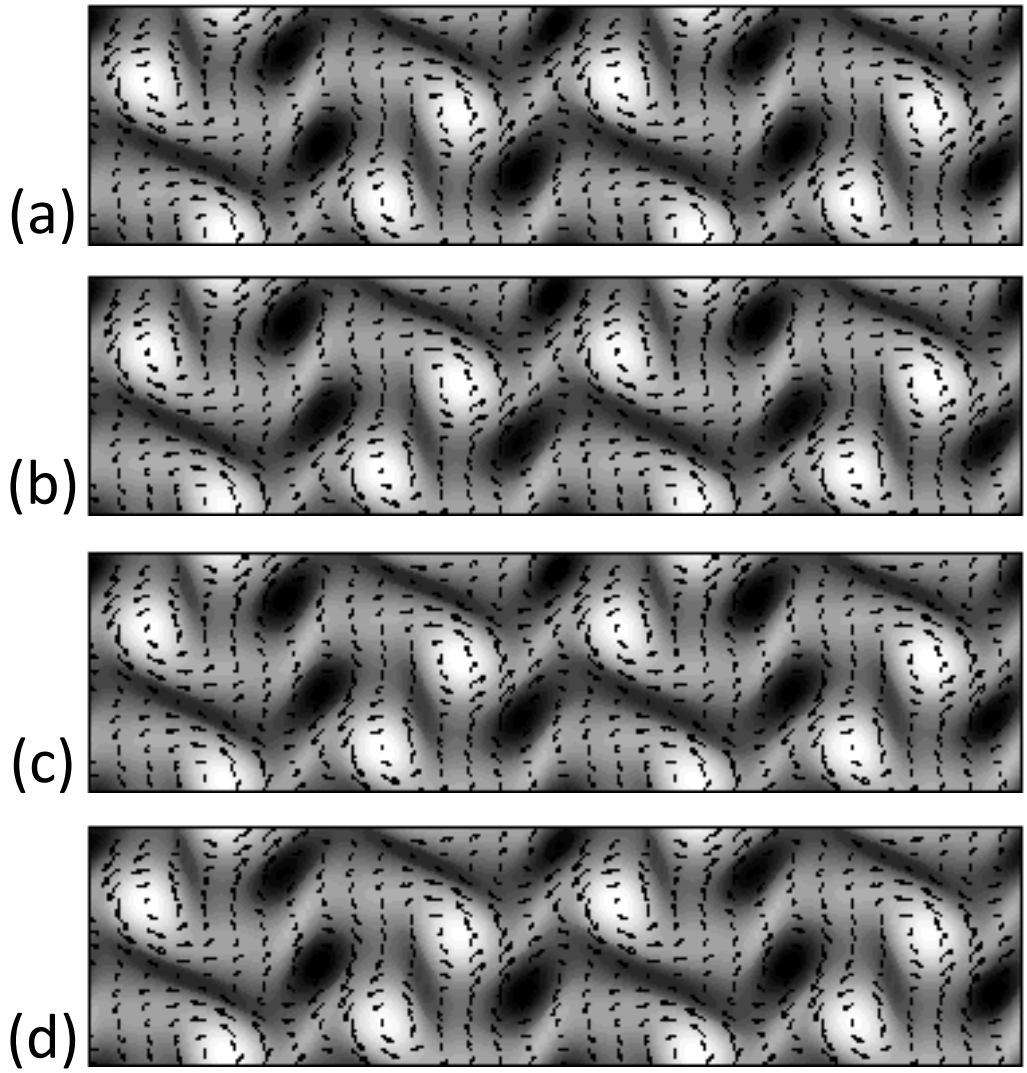

Figure 30: Time-periodic flow P_{5n} at $A = 0.750$ s^{-2} and (a) t=0, (b) t=T/4, (c) t=T/2, (d) t=3T/4 with $T = 140.15$ s. System size is 19.5 cm $\times$ 5 cm.

The stable node loses its stability for $L_x \lesssim 9.77$ cm and for $L_x \gtrsim 16.23$ cm, both through supercritical Hopf bifurcations, which give rise to two new periodic flows denoted P_{1n} and P_{2n}, respectively. Four snapshots of each of these flows are shown in Figs. 26 and 27. P_{1n} undergoes a secondary Hopf bifurcation at $L_x \approx 9.71$ cm, becomes unstable and is replaced with a quasiperiodic flow for smaller values of L_x. P_{2n} undergoes a pitchfork bifurcation and becomes unstable at $L_x \approx 17.12$ cm. From this bifurcation there emerges a new stable, time-periodic solution, which we will

denote P_{3n} and is shown in Fig. 28. At $L_x \approx 18.67$ cm it becomes unstable through a saddle-node bifurcation. There is another time-periodic state (denoted P_{4n} and shown in Fig. 29) which is stable for the range 18.16 cm $\lesssim L_x \lesssim$ 18.99 cm. At $L_x \approx 18.16$ cm this flow loses stability through a flip bifurcation and at $L_x \approx 18.99$ cm it becomes unstable through a Hopf bifurcation. Finally there is yet one more periodic orbit (denoted P_{5n} and shown in Fig. 30) that is stable or the range 19.42 cm $\lesssim L_x \lesssim$ 19.53 cm. It too becomes unstable through a Hopf bifurcation for $L_x \lesssim$ 19.42 cm. In the range 18.99 cm $\lesssim L_x \lesssim$ 19.42 cm, the flow is quasiperiodic so more than likely both Hopf bifurcations on either side of this interval for P_{4n} and P_{5n} are subcritical. P_{2n} regains its stability through a second pitchfork bifurcation at $Lx \approx 19.98$ cm. The unstable steady flow remains as such over the entire interval and as can be seen in Fig. 31, both N and S come into existence from the same point. The same thing occured as A was varied and P_1 Sect. 4.1 underwent an infinite period bifurcation. This flow (as with all the flows from Sect. 4.1)) is characterized by 4 positively-oriented vortices and 4 negatively-oriented ones. This continuation procedure loses convergence at $L_x \approx 19.012$ cm as 8 more positively-oriented vortices and 8 negatively-oriented ones begin to emerge in the flow pattern.

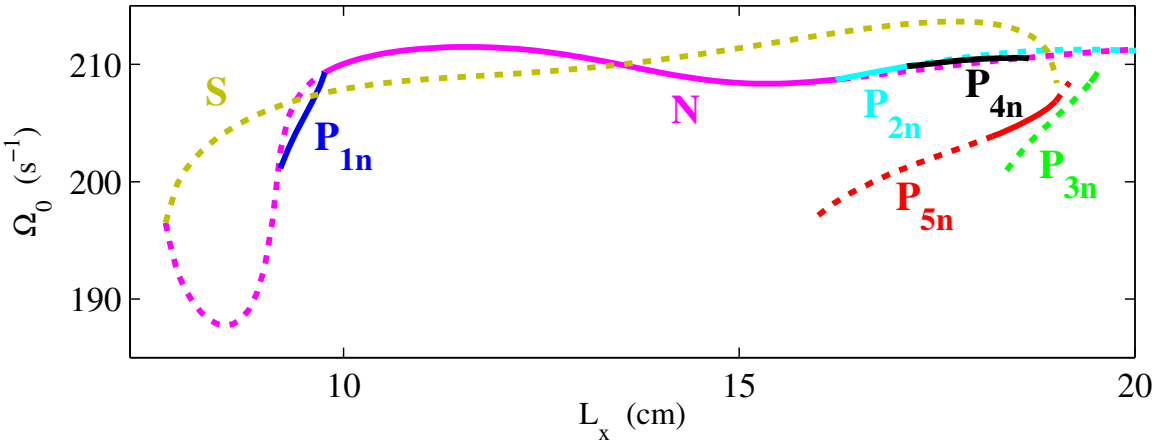

Figure 31: Bifurcation diagram ($A = 0.750$ s^{-2}). The relative vorticity magnitude $\Omega_0 \equiv \|\Omega - \Omega_L\|_2$ is shown. Solid and dotted lines denote stable and unstable states, respectively and periodic orbits are represented by their time-averaged values.

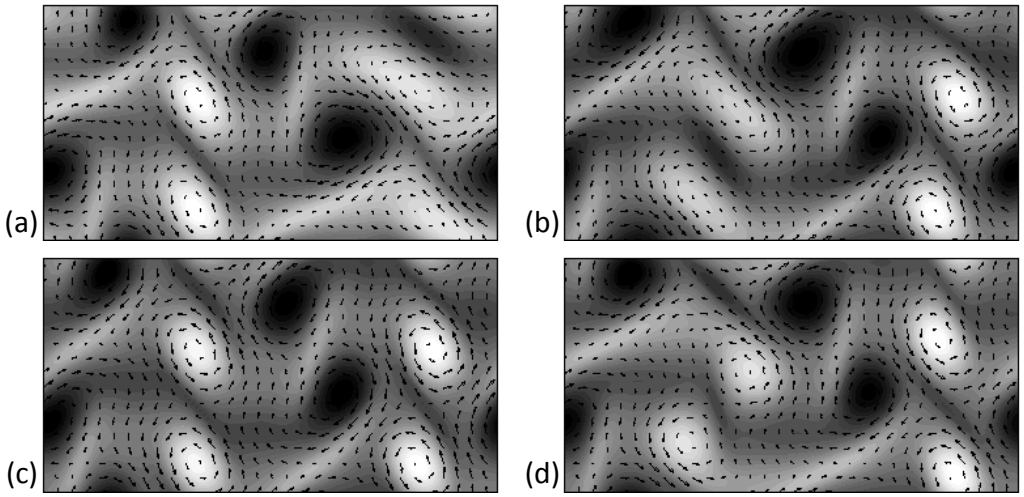

Figure 32: Time-periodic flow P_{6n} at $A = 0.850$ s^{-2} and (a) t=0, (b) t=T/4, (c) t=T/2, (d) t=3T/4 with $T = 37.22$ s. System size is 9.6 cm $\times$ 5 cm.

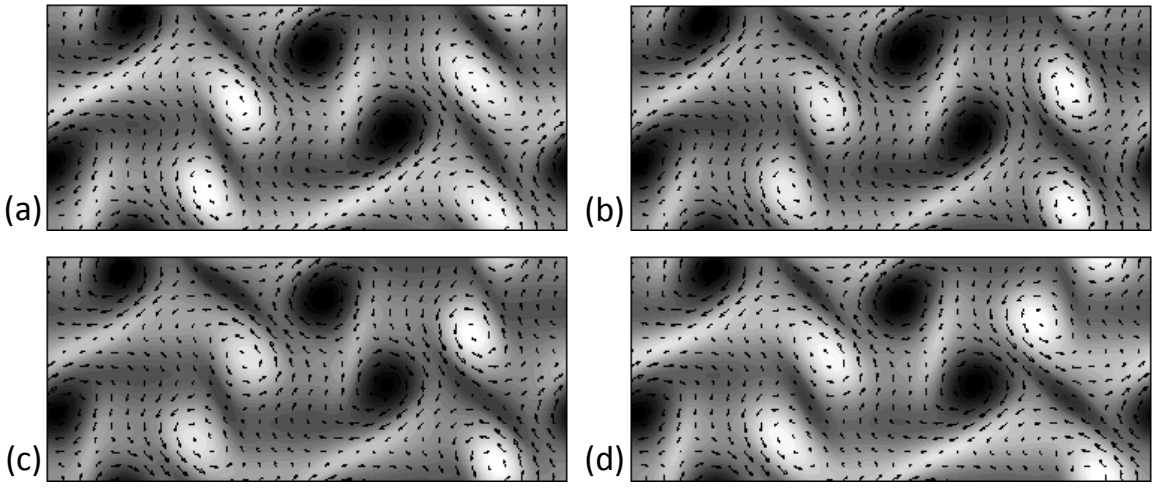

Figure 33: Time-periodic flow P_{7n} at $A = 0.850$ s^{-2} and (a) t=0, (b) t=T/4, (c) t=T/2, (d) t=3T/4 with $T = 22.05$ s. System size is 11.5 cm $\times$ 5 cm.

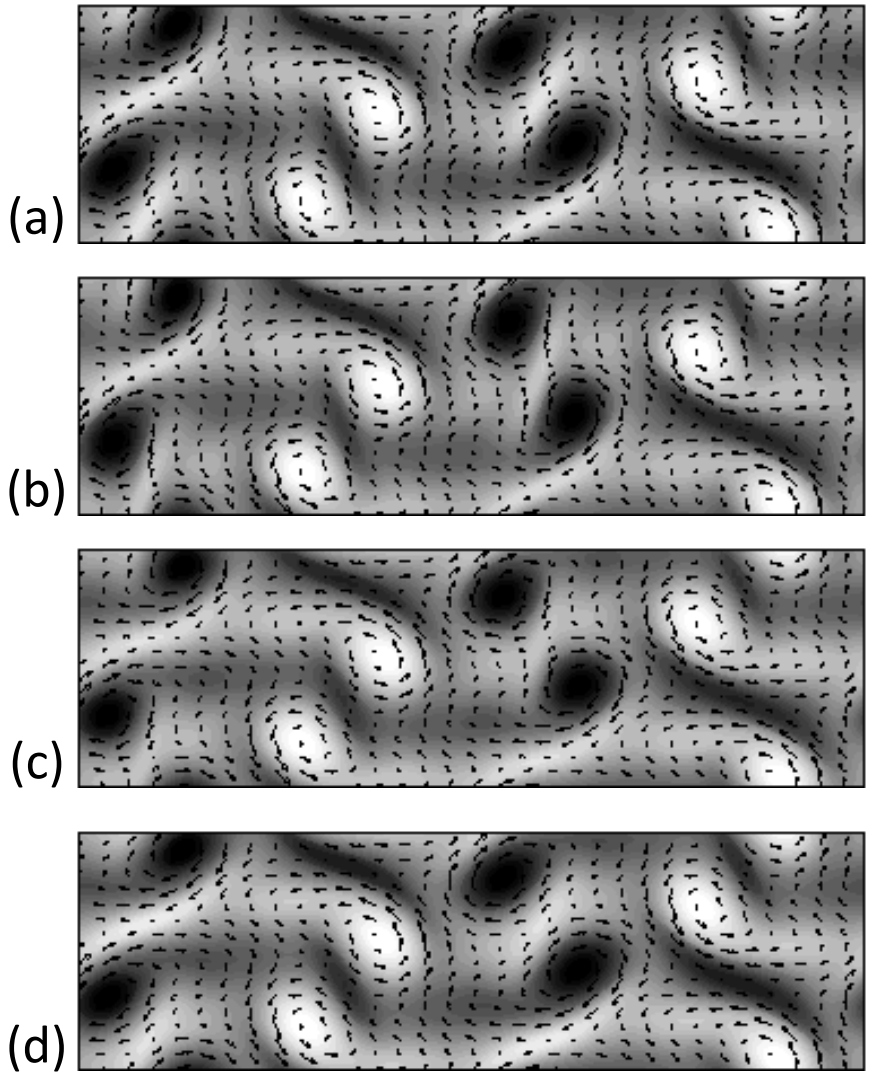

Figure 34: Time-periodic flow P_{8n} at $A = 0.850$ s^{-2} and (a) t=0, (b) t=T/4, (c) t=T/2, (d) t=3T/4 with $T = 11.50$ s. System size is 16.5 cm $\times$ 5 cm.

The unstable state, N ($A = 0.850$ s^{-2}), very quickly becomes stable as the length of the magnets is increased at $L_x \approx 10.10$ cm. For values of L_x smaller than this the flow is quasiperiodic so this is almost certainly part of the same branch as the quasiperiodic attractor that appears when P_2 (cf. Sect. 4.1) loses stability through a secondary Hopf bifurcation. This also means that likely this is a subcritical Hopf bifurcation that occurs at $L_x \approx 10.10$ cm. There is an unstable orbit with extremely large leading Floquet multipliers but the Newton-Krylov solver could only successfully

continue it for a very narrow range of L_x. We label this orbit P_{6n} and it is shown in Fig. 32. As L_x is increased, N loses stability at approximately 10.36 cm through another subcritical Hopf bifurcation. Just past this point, the flow is chaotic and remains so until $L_x \approx 10.8$ cm where a stable, quasiperiodic attractor appears. A new stable, periodic state also appears at $L_x \approx 11.28$ cm that we will denote P_{7n} (shown in Fig. 33), and depending on where the initial condition starts in state space, it will eventually settle into one of these two flows for $L_x \gtrsim 11.28$ cm. However, for $L_x \gtrsim 11.55$ cm, it seems that the quasiperiodic flow has either lost its stability or perhaps its basin of attraction has become extremely small since all the initial conditions tested converged onto P_{7n}. In any case, N regains stability once again through yet another Hopf bifurcation at $L_x \approx 11.71$ cm. P_{7n} is stable up to $L_x \approx 11.80$ cm where it undergoes a saddle-node bifurcation, so there is again a competition between two stable attractors for this range of L_x. N remains stable until $L_x \approx 15.57$ cm where it undergoes a supercritical Hopf bifurcation and another new periodic state emerges, which we will denote P_{8n} (shown in Fig. 34). This state becomes unstable through a pitchfork bifurcation at about $L_x \approx 16.74$ cm and another stable, periodic state emerges. All of these results are summarized in the bifurcation diagram which is Fig. 35. It turns out that, for the appropriate range of L_x, one can continuously deform P_{8n} into P_{2n} by fixing L_x and varying A. So these two flows are one and the same, meaning they are both part of the same "branch" in the parameter space spanned by L_x and A.

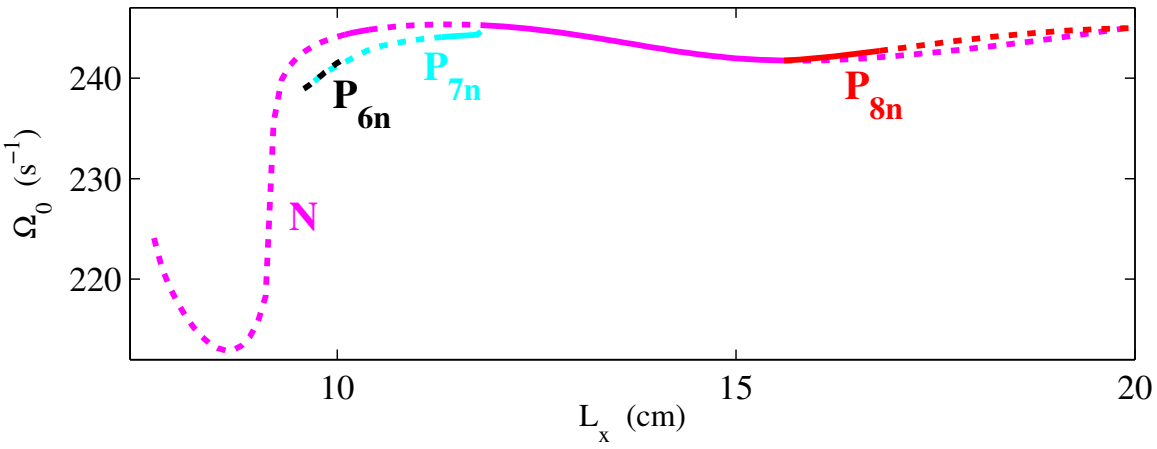

Figure 35: Bifurcation diagram ($A = 0.850$ s^{-2}). The relative vorticity magnitude $\Omega_0 \equiv \|\Omega - \Omega_L\|_2$ is shown. Solid and dotted lines denote stable and unstable states, respectively and periodic orbits are represented by their time-averaged values.

Varying the length of the magnets for the periodic flows from Sect. 4.1 (P_1, P_2, and P_3) proved to be not as fruitful. For all 3 flows, the step size necessary to achieve convergence was $\Delta L_y \sim 0.001$ cm which made the procedure very computationally intensive. For P_1, the continuation procedure in A led to an infinite period bifurcation and it appears that the same holds true when trying to continue this flow to smaller and larger values of L_y as the period T increased monotonically in both directions. For $L_y = 9.244$ cm, $T \approx 2040$ s and for $L_y = 11.940$ cm, $T \approx 1244$ s. For my Newton-Krylov solver, this meant that it took about 2 to 3 days to get each new state to converge. And, given the step size necessary for convergence, this meant that it would take 2000-3000 days to advance the state forward or backward by 1 cm in L_x! Clearly, a different approach needs to be taken in order to see how these flows change as one varies the system size.

These various bifurcation analyses show that there are a wide variety of different types of flows that can be found by changing the parameters of the system. But, more importantly, they are very structually stable even for relatively high Reynolds numbers. So in the laboratory, an experimentalist has a lot of freedom in choosing

the desired parameters for the experimental setup depending on the type of flow he or she desires. In the next chapter we will discuss the mixing properties of the various flows in the four-magnet array system.

4.5 Weakly turbulent regime

We conclude the present chapter with a discussion of the weakly turbulent regime for the 4-magnet system ($A = 1.0$ s^{-2}, $Re \approx 67$). There have been a number of reviews published in the past ten years which have discussed 2D turbulence in depth summarizing much of what we have learned through both numerical as well as experimental studies and what questions still remain open [59, 26, 117]. Exact invariant solutions (or exact coherent structures) have proven useful in recent years for understanding the dynamics of weak turbulent flow [63, 49, 39]. The point of view is that these flows can be thought of as a trajectory in phase space whose path is guided by unstable invariant solutions and their manifolds. Particularly, periodic orbits appear to resemble many of the structures seen in turbulent fluids and turbulence consists of a series of transitions between these states. Additionally, these unstable periodic orbits can be used to form weighted sums that can quantitatively predict observables and statistics in turbulent flow [29]. The difficulty is not so much in computing them but, rather, determining which ones are dynamically the most important. Typically it is the least unstable ones that play this role. These ideas are part of what is known as Periodic Orbit Theory, and it has been successfully applied to a great number of low-dimensional dynamical systems. With fluids, using the theory is a bit more subtle. These weighted sums are derived under the assumption of hyperbolicity which the Navier-Stokes equations do not satisfy [21]. Another issue is that to use the traditional trace formulas one needs strictly periodic orbits, so if one has relative periodic orbits, the symmetry should quotiented out. Finally, given the high dimensionality, it is likely that important invariant solutions may be missed thus reducing the accuracy

of any calculation.

Recently, Chandler and Kerswell [21] computed 50 unstable periodic solutions for the 2D Kolmogorov flow and used them as mentioned above to attempt to reconstruct various statistical quantities of the flow. They had a moderate amount of success in this endeavor but found the power of the theory lacking for higher Reynolds numbers. They also mentioned that they found their work to be quite time-consuming both computationally as well as in the manual labor involved in processing the data. Coincidentally, we also found 50 unstable solutions, the difference being that it was using a flow at a higher Reynolds number. Their solutions were computed at Re=40 and ours, using their definition of the Reynolds number, were computed at $Re \approx 60$. Additionally, the two models themselves were different. Their model did not include the Rayleigh friction term and they used a different number of magnets. Our model uses four magnets, whereas theirs used eight. While all of the periodic orbits found are unstable, it remains to determine their stability multipliers. In computing these solutions, there were literally hundreds of duplicates of each, so it was decided to postpone the calculation of their stability once they were sorted to be used in periodic orbit expansions. There were 5 periodic orbits found and 45 relative periodic orbits. Shown in Table 3 are their period, T, and their shift in the direction of the continuous symmetry, X, and their absolute residual ($||f^T(\Omega) - \Omega||_2$). Two examples of these orbits are shown in Figs. 36 and 37

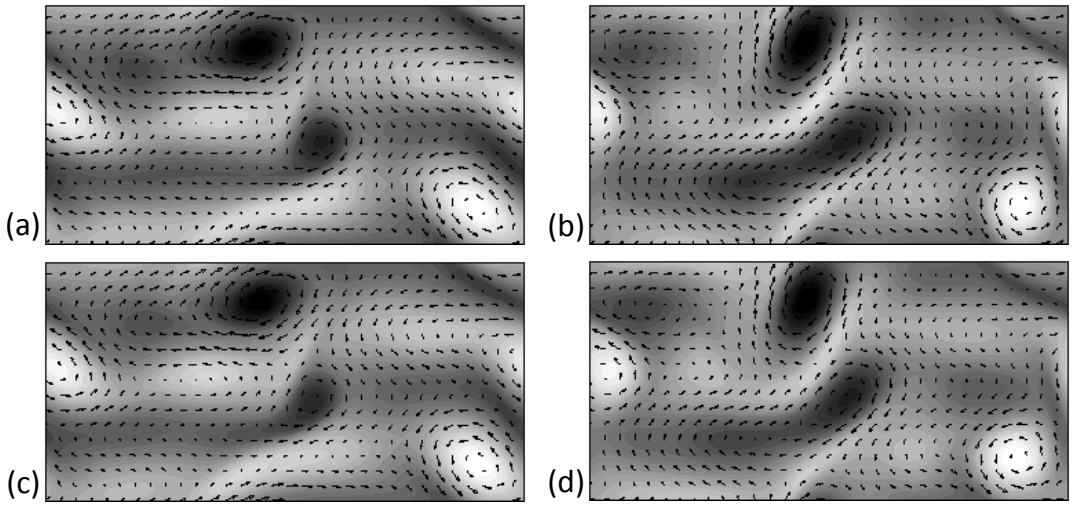

Figure 36: Time-periodic flow RP_1 at $A = 1.00$ s^{-2} and (a) t=0, (b) t=T/4, (c) t=T/2, (d) t=3T/4 with $T = 19.201$ s. The speed of the comoving frame is 5.78×10^{-3} cm/s. System size is 10 cm $\times$ 5 cm.

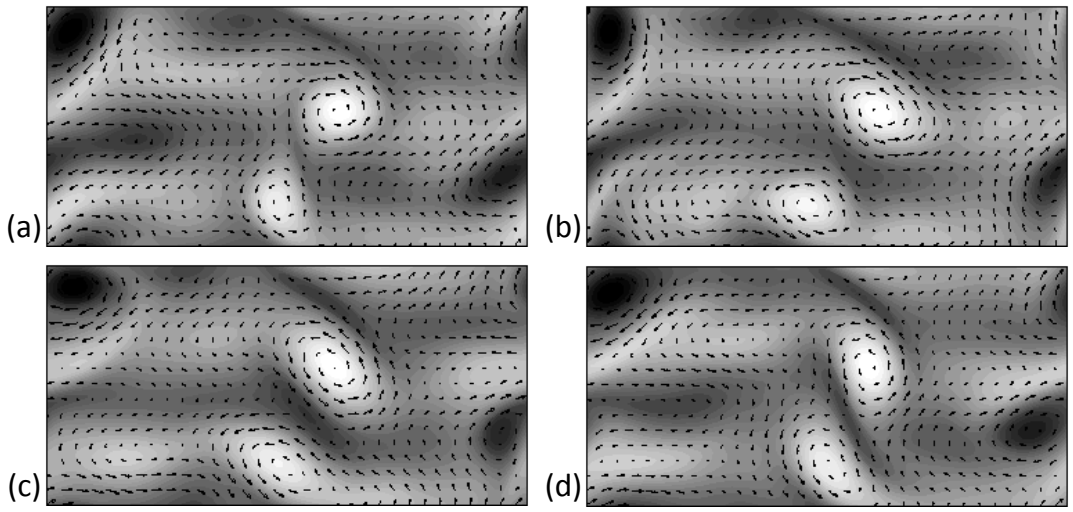

Figure 37: Time-periodic flow RP_2 at $A = 1.00$ s^{-2} and (a) t=0, (b) t=T/4, (c) t=T/2, (d) t=3T/4 with $T = 9.4941$ s. The speed of the comoving frame is 5.28×10^{-3} cm/s. System size is 10 cm $\times$ 5 cm.

Table 3: Invariant sets found directly from turbulent DNS data. T is the period of the periodic and relative periodic orbit. X is the shift in the direction of continuous symmetry.

T (s)	X (cm)	residual (s^{-1})	T (s)	X (cm)	residual (s^{-1})
8.8583	0	2.0874e-09	20.725	0	3.7592e-10
9.2727	-6.0487e-02	8.2862e-09	27.558	1.2275e-01	6.1731e-10
9.4941	-5.0147e-02	1.5577e-09	28.155	1.1620e-01	1.9071e-11
9.6401	-5.1403e-02	7.9679e-09	28.434	-9.9363e-02	2.0582e-11
9.6486	-2.0616e-02	1.5861e-10	28.482	-1.5044e-01	1.8343e-11
9.6828	3.1529e-02	1.7004e-08	29.048	9.4586e-02	1.5925e-08
9.8460	1.7802e-02	3.9941e-09	36.238	-1.3288e-01	2.4251e-10
10.132	-9.1437e-03	5.7753e-09	36.437	1.5635e-01	1.3347e-08
10.855	-5.7737e-02	7.9555e-09	37.567	-2.3585e-01	1.0032e-10
18.545	-1.2098e-01	7.5091e-09	38.177	0	2.5899e-09
18.719	1.0866e-01	3.6565e-08	38.379	1.6971e-01	8.7191e-11
18.813	8.7321e-02	8.1460e-11	38.402	-2.2209e-01	1.6797e-09
18.977	7.4574e-02	1.3809e-11	38.571	-1.2742e-01	9.0572e-11
18.981	-1.0450e-01	1.0784e-10	38.594	-8.2463e-02	2.8261e-08
19.988	-1.0029e-01	1.3116e-10	38.619	-5.0578e-02	8.1186e-09
19.089	0	1.3408e-10	38.731	1.2611e-01	3.8195e-10
19.189	-8.4856e-02	1.7970e-08	38.839	-4.9365e-02	5.4705e-09
19.201	-1.1104e-01	6.2379e-09	39.293	1.2661e-01	9.7316e-09
19.280	1.0281e-01	2.4388e-11	39.384	-7.1208e-02	1.4845e-08
19.297	-4.1231e-02	3.1117e-09	41.450	0	1.4575e-09
19.366	6.3057e-02	3.3184e-11	42.570	-1.3553e-02	2.7396e-09
19.692	3.5604e-02	2.0068e-11	47.811	1.7636e-01	1.3388e-09
19.904	3.7952e-03	5.3324e-10	47.927	1.7457e-01	4.0416e-09
20.180	-5.1835e-02	6.5104e-11	55.479	2.5662e-01	1.5099e-08
20.325	-4.7060e-02	1.3236e-08	58.803	2.0718e-01	4.2857e-09

CHAPTER V

MIXING

5.1 Numerical results

In this section we discuss the transport properties of the flows found in the 4-magnet system, which are also representative of the types of flows found in bigger systems. Transport properties can be conveniently quantified using two different metrics: (i) the relative size (in this case area) of the mixed region and (ii) the rate of mixing. Both metrics are most easily evaluated by following the evolution of an initially well-localized array of passive tracers. Before continuing with the detailed discussion of mixing dynamics, we should point out that, while the laminar flow L is expected to be the worst mixer and the aperiodic (turbulent) flow to be the best, the complicated sequence of transitional states observed as A is increased implies that we should not expect a monotonic increase for either metric. While one would expect both metrics to mirror the spatial and temporal complexity of the flow, we find that this correlation is far from perfect.

The dynamics of passive tracers in 2D flows of incompressible fluids is formally described by a Hamiltonian system (1) with one degree of freedom where the stream-function $\Psi(x, y, t)$ plays the role of a Hamiltonian and the coordinates x and y are the conjugate variables. Time-independent, one-degree-of-freedom Hamiltonian systems are always integrable and thus exhibit regular motion. The tracers follow closed streamlines on which Ψ is exactly conserved, hence the initial tracer distribution eventually stretches along the streamline passing through its center but never broadens. However, the introduction of time-dependence is expected to split the flow domain into regions of chaotic and regular dynamics. The relation between mixing and chaotic

streamlines establishes a direct analogy between transport in one-degree-of-freedom Hamiltonian systems and mixing in 2D area-preserving flows.

In order to quantify the mixing process, for each value of A, a set of passive tracers was initially placed in a square region 0.1 mm on each side (which corresponds to initial area fraction $f(0) = 2 \times 10^{-6}$). Since the greatest degree of stretching usually occurs along homoclinic or heteroclinic trajectories, the initial sets were centered on top of one of the saddles of the instantaneous flow field.

Each tracer was advected forward in time by numerically integrating (1) using a fourth-order, area-preserving, symplectic integrator based on the 2-stage Gauss-Legendre scheme described in Chapter 3. Velocities for each tracer were computed at each time step using a cubic interpolation scheme on the 64×128 grid in real space.

The dispersion of tracers was then used to compute the mixing metrics. The mixed area fraction $f(t)$ was computed by partitioning the flow domain into a set of small boxes and computing the ratio between the number of boxes m containing at least one tracer to the total number of boxes k. When the tracers uniformly cover the domain, the area fraction should be unity. However, if there are k boxes with n randomly distributed tracers, the fraction of boxes containing at least one tracer would on average be $p_{n,k} = 1 - \exp(-n/k)$. Thus, the measured area fraction for each value of A was normalized by $p_{n,k}$

$$f(t) = \frac{m(n,t)}{k p_{n,k}}, \tag{54}$$

so that a uniformly distributed set of tracers would give an area fraction of one.

Fig. 38 shows the area fraction occupied by the tracers after a rather long time interval of 5×10^4 s. In comparison, the period of P_1, P_2 and P_3 is of order 100 s, while the characteristic time scale of the flow around vortices is below 10 s. We find that the area fraction remains near zero for all of the time-independent flows (L, M, and N), as it should be since they are integrable.

For time-dependent flows (1) formally becomes a three-dimensional dynamical system (augmented by an equation $\dot{t} = 1$) which, in general, possesses chaotic solutions (streamlines). Chaotic advection, in principle, should dramatically enhance mixing. However, as Fig. 38 shows, the mixed area fraction for P_1 and P_2 is only slightly higher than that for the time-independent flows. The time-periodic flow P_3, on the other hand, produces nearly perfect mixing, with mixed area fraction comparable to that of aperiodic flows.

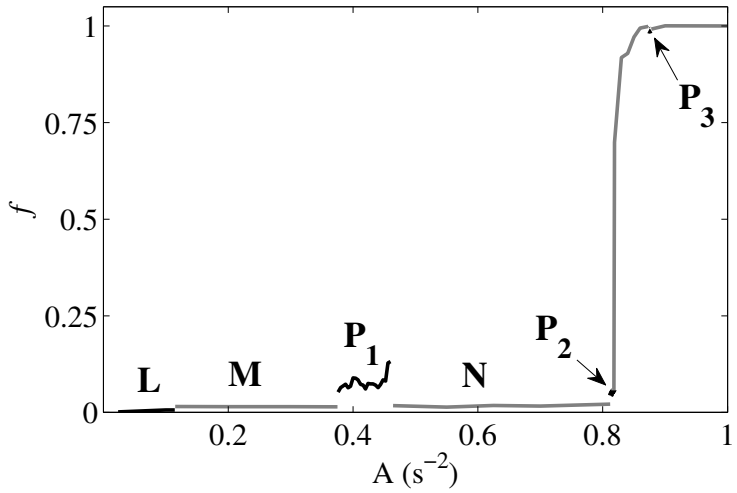

Figure 38: The fraction f of the mixed area relative to the total area of the domain at $t = 5 \times 10^4$ s.

Examining the temporal evolution of the area fraction covered by the tracers shown in Fig. 39, one can discern two distinct stages for the time periodic flows. Initially there is a very fast increase. For P_1 and P_2 it corresponds to rapid stretching of the set of tracers along the homoclinic trajectories forming a thin closed band (see Figs. 40(a) and (c)). This is followed by a much slower growth associated with the broadening of this band. However, even after a very long time, the band of tracers remains quite thin and aligned along the streamlines of the instantaneous flow (see Figs. 40(b) and (d)).

For P_3, on the other hand, the set of tracers undergoes a rapid initial phase of

both stretching *and* folding and quickly (within several periods of the flow) covers almost the entire domain (see Fig. 41(a)). Furthermore, a closer look shows that, for P_2 and P_3, the tracer distribution reaches an asymptotic state already around 10^3 s, while for P_1 the area fraction is still growing at $t = 5 \times 10^4$ s. Finally, although the asymptotic distribution of the tracers for P_3 is essentially uniform, the tracers never penetrate four small regular islands centered around vortices with positive vorticity, as Fig. 41(b) illustrates. We will return to this fact in Sect. 5.4.

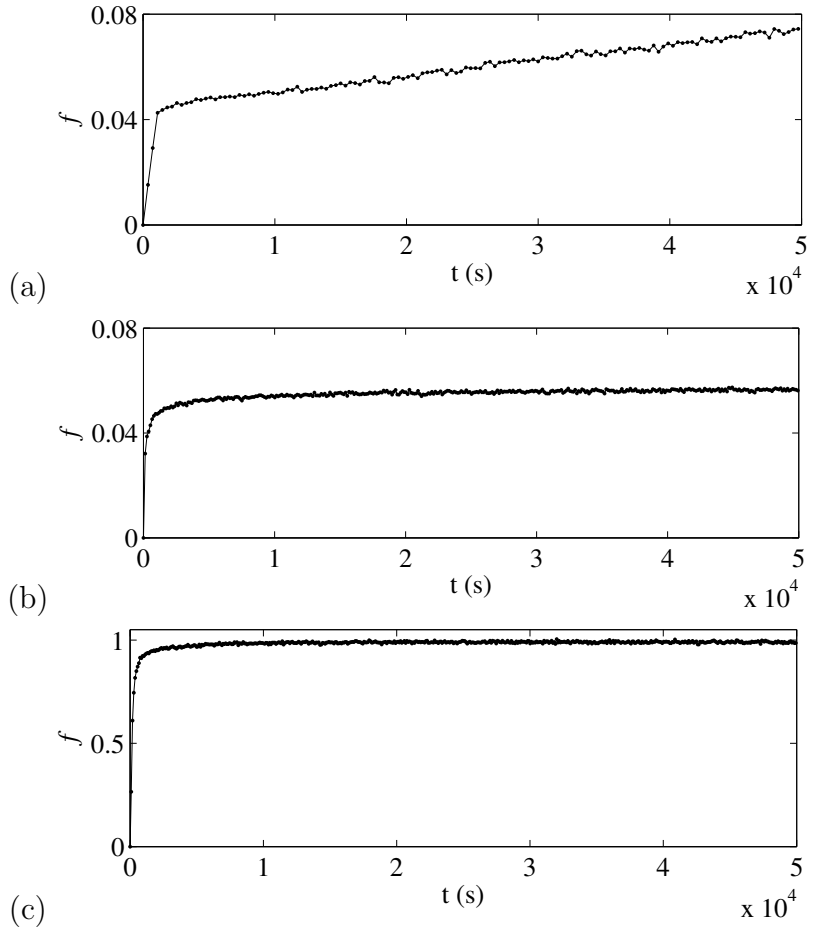

Figure 39: Temporal dependence of the area fraction for the three time-periodic flows: (a) P_1 at $A = 0.428$ s^{-2}, (b) P_2 at $A = 0.817$ s^{-2}, and (c) P_3 at $A = 0.875$ s^{-2}.

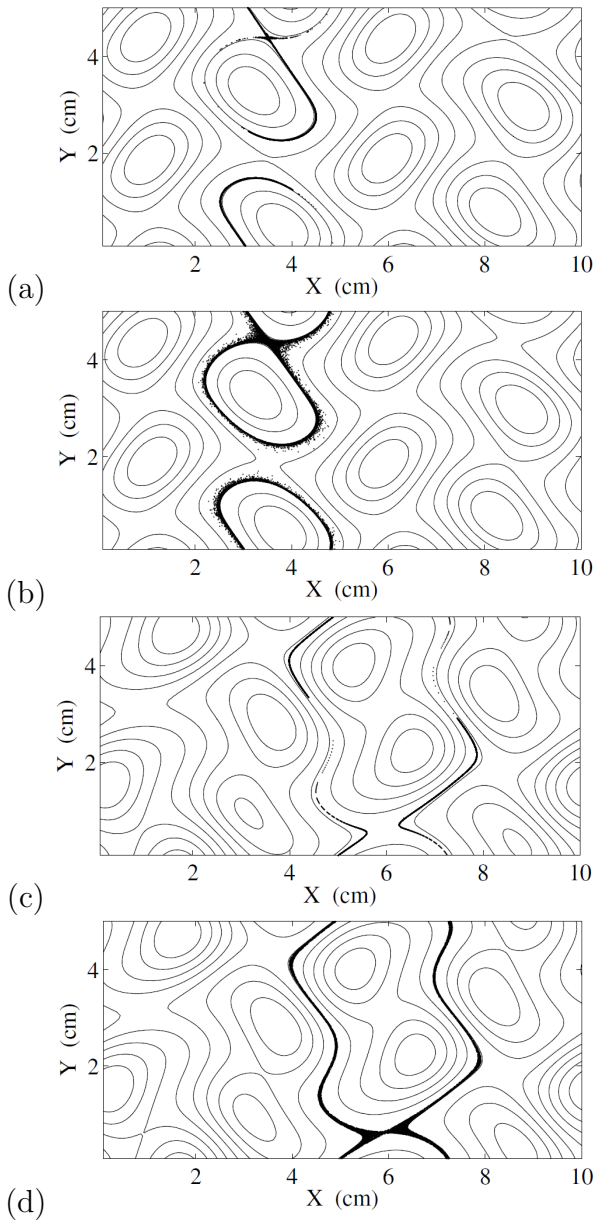

Figure 40: Mixing by the time periodic flows. The distribution of 6×10^4 tracers and the streamlines of the instantaneous flow for P_1 at $t = 598$ s (a) and $t = 5 \times 10^4$ s (b). The same for P_2 at $t = 49$ s (c) and $t = 5 \times 10^4$ s (d).

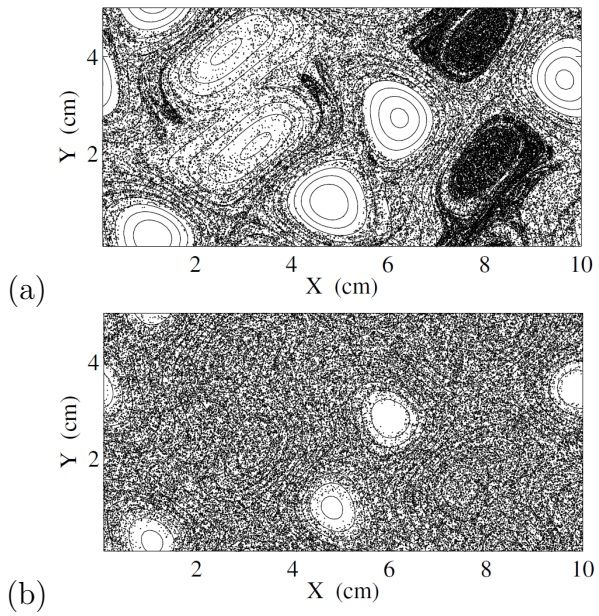

Figure 41: Mixing by the time-periodic flow P_3. The distribution of 6×10^4 tracers and the streamlines of the instantaneous flow at $t = 317$ s (a) and $t = 3500$ s (b).

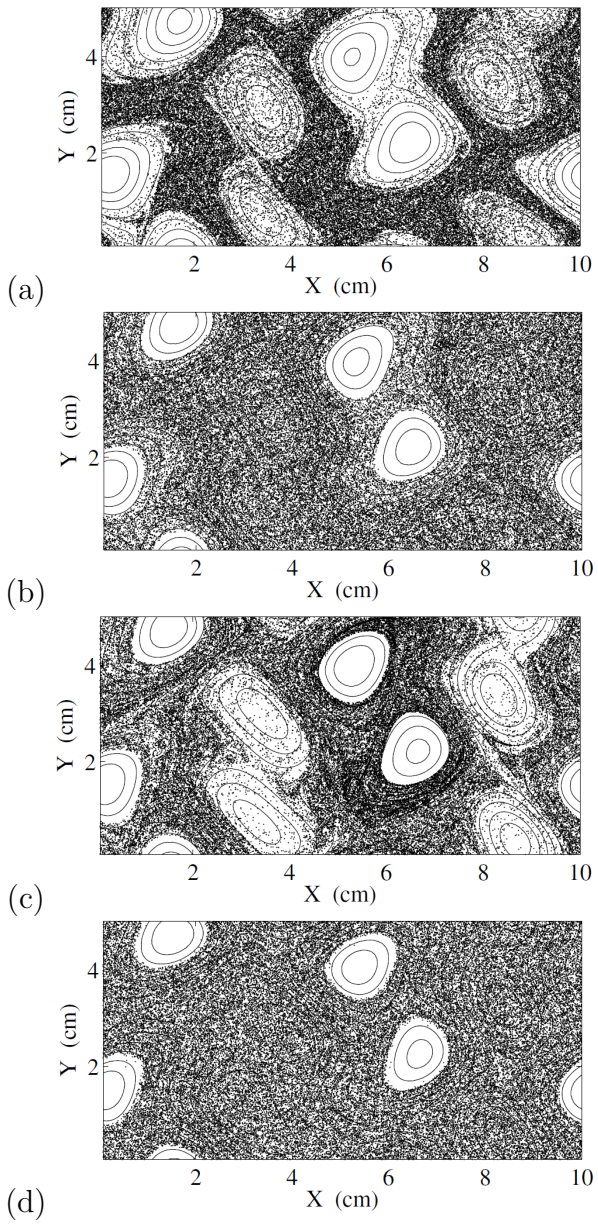

Figure 42: Mixing by quasi-periodic flow QP. The distribution of 6×10^4 tracers and streamlines of the instantaneous flow for $A = 0.820$ s^{-2} at $t = 1038$ s (a) and $t = 3500$ s (b). Same for $A = 0.846$ s^{-2} at $t = 645$ s (c) and $t = 3500$ s (d).

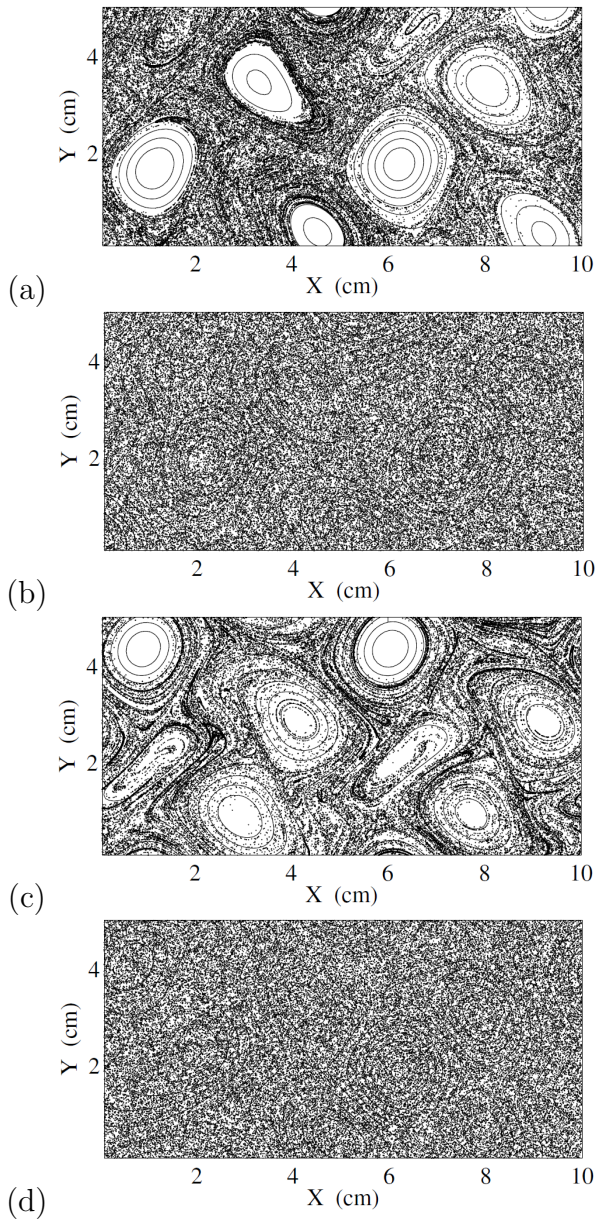

Figure 43: Mixing by aperiodic flow. Distribution of 6×10^4 tracers and the streamlines of the instantaneous flow for $A = 0.872$ s^{-2} at $t = 369$ (a) and $t = 3500$ s (b). The same for $A = 0.878$ s^{-2} at $t = 221$ s (c) and $t = 3500$ s (d).

Fig. 42 shows the tracer distribution for two values of A above the onset of the secondary Hopf bifurcation which destroys P_2 and makes the flow quasi-periodic. We find the evolution of the tracers to follow the same scenario as in the case of the time-periodic flow P_3: after a short initial stage of stretching and folding, the set of

tracers fills a significant fraction of the full domain. This stage is followed by a much slower homogenization process in which the distribution becomes spatially uniform. However, just like in the case of P_3, the tracers never penetrate four regular islands centered around vortices, now with negative vorticity.

The fundamental difference between (quasi)periodic and aperiodic flows makes itself apparent if we compare mixing by the periodic flow P_3 with that by aperiodic flows just outside of the window of stability for P_3, at $A = 0.872$ s^{-2} and $A = 0.878$ s^{-2}. Although the forcing is almost identical in these three cases and the short-term dynamics of the three flows are similar, Fig. 43 shows that the aperiodic flows achieve perfect mixing in the long term, covering the entire domain, including the four regular islands of P_3.

Fig. 44 summarizes the observed mixing rate as a function of the control parameter A. As Fig. 39 amply illustrates, the mixing process is characterized by a range of time scales. The fastest time scale describes stretching of the initial tracer distribution along the streamline passing through its center. The corresponding rate is defined as $r_{\max} = \max_t |df/dt|$ and is proportional to the average shear rate corresponding to that streamline.

The slowest time scale describes broadening of the distribution due to transport of tracers through semi-penetrable barriers discussed in Sect. 5.4. To characterize this broadening, we computed the time t_{90} it takes for the area fraction to reach 90% of its asymptotic value, $f(t_{90})/f(t_{100}) = 0.9$, where we assumed the asymptotic distribution is achieved at $t_{100} = 5 \times 10^4$ s. The minimal mixing rate was then defined as $r_{\min} = 1/t_{90}$. In both cases we averaged $f(t)$ over a small window to filter out small oscillations associated with the passage of tracers near saddles.

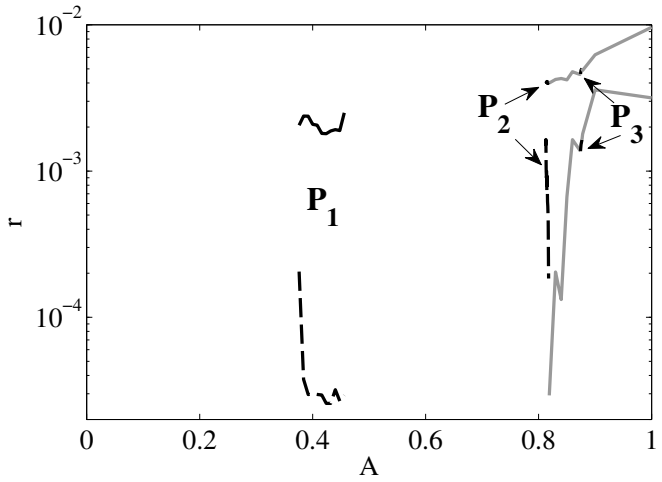

Figure 44: The rates of mixing for time-dependent flows as a function of A. The solid and dashed curves correspond, respectively, the fastest time scale $r_{\max}$ and the slowest time scale $r_{\min}$.

The fast time scale $r_{\max}$ is found to increase almost monotonically with A, reflecting the corresponding increase in the shear of the underlying flow. The slow time scale requires more care to interpret. In particular, for P_1 we find $r_{\min}$ to drop by almost an order of magnitude as A increases. This decline is associated with the tracer distribution (shown in Fig. 40(b)) slowly broadening in time as illustrated by Fig. 39(a). This broadening is due to a slow "leak" of tracers across a semi-penetrable transport barrier, creating a "halo" of tracers surrounding the main band. Another drop, observed around the secondary Hopf bifurcation at $A \approx 0.818$ s^{-2}, is associated with a similar process for the quasi-periodic flow QP. As A increases past this critical value of A, the transport barrier which exists for P_2 gets eroded, leading to a quick increase in $r_{\min}$.

While many of our numerical results are quite logical, several findings raise questions. For instance, the flows P_1 and P_3 appear to be qualitatively very similar. Both are stable, time-periodic and, with the choice of $A = 0.428$ s^{-2} for P_1, both have

a time-dependent component of the same magnitude $\varepsilon \approx 0.238$. Yet, despite these similarities, their mixing properties are radically different. P_1 is a very poor mixer, as Fig. 40(b) illustrates. It is characterized by both a very low mixing rate and a very low mixed area fraction. In fact, P_1's mixing properties are comparable to those of time-independent flows. P_3, on the other hand, is an extremely good mixer, almost as good as the aperiodic flows. The mixing rate for this flow is high and its mixed area fraction is close to unity.

Another question concerns the islands surrounding positive or negative vortices that remain impenetrable for extremely long times for both the time-periodic flow P_3 (Fig. 41) and the quasi-periodic flow QP succeeding P_2 (Fig. 42). In both cases there appear to be transport barriers surrounding vortices characterized by vorticity of one sign but not the other. This was also found to occur in the model flow of Danilov *et al.* [32] as well as in real oceanic flows [52].

5.2 Lagrangian coherent structures

Finite-time Lyapunov exponent (FTLE) fields associated with the time-dependent flows provide some intuition regarding their drastically different mixing properties. The forward FTLE is a scalar quantity

$$\sigma(\mathbf{x}_0, \tau) = \frac{1}{\tau} \ln \left\| \frac{D\mathbf{x}(\tau)}{D\mathbf{x}_0} \right\|_2, \tag{55}$$

which characterizes the amount of stretching along a trajectory $\mathbf{x}(t)$ passing through the point $\mathbf{x}_0$ at $t = 0$ over a finite time interval τ. In particular, the ridges of the forward FTLE field define Lagrangian Coherent Structures (LCS) [108] which, for time-periodic flows, correspond to segments of unstable manifolds of saddle orbits with temporal period equal to that of the flow. Similarly, backward FTLE fields are defined in the same manner but with respect to backward time, and they correspond to segments of stable manifolds. As Fig. 45 illustrates, for P_1 and P_2 the LCS show very little folding, effectively forming closed, compact curves. For P_3, on the other

hand, the LCS display a lot of folding, which is a necessary ingredient for efficient mixing and cover a substantial fraction of the total area. Indeed, we find the LCS of P_1 and P_2 are qualitatively similar to those of steady flows from which they are born (i.e., M and N), while the LCS of P_3 are qualitatively similar to those of aperiodic flows, which is consistent with the observed similarities in their mixing properties.

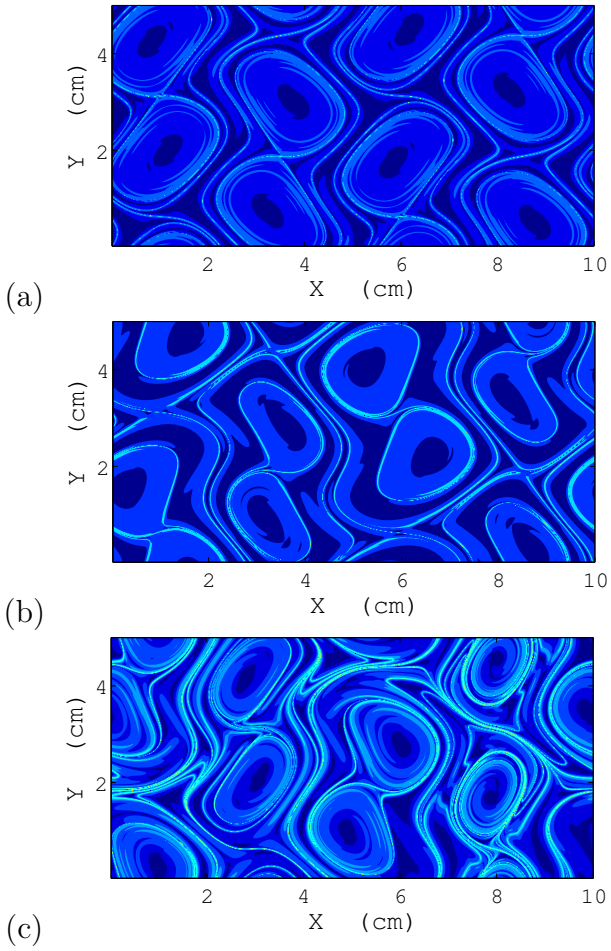

Figure 45: Forward finite-time Lyapunov exponent field. Light blue indicates the locations of the ridges. (a) P_1 at $A = 0.428$ s^{-2} with $\tau = 32$ s, (b) P_2 at $A = 0.817$ s^{-2} with $\tau = 19$ s, and (c) P_3 at $A = 0.875$ s^{-2} with $\tau = 22$ s.

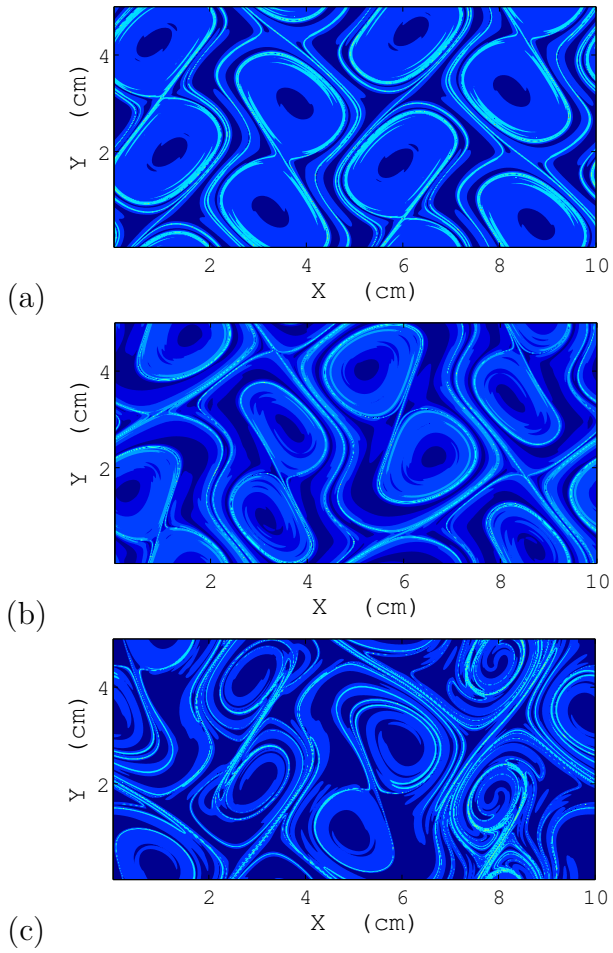

Figure 46: Backward finite-time Lyapunov exponent field. Light blue indicates the locations of the ridges. (a) P_1 at $A = 0.428$ s^{-2} with $\tau = 36$ s, (b) P_2 at $A = 0.817$ s^{-2} with $\tau = 19$ s, and (c) P_3 at $A = 0.875$ s^{-2} with $\tau = 22$ s.

LCS play an important role in organizing transport. For instance, placing the initial set of tracers on top of the saddle orbit we should expect that set to be quickly stretched along the LCS forming effectively one-dimensional structures for P_1 and P_2, while for P_3 the structure becomes effectively two-dimensional. Furthermore, the LCS form transport barriers which cannot be crossed by the tracers. For P_1 and P_2 (as well for steady flows), these transport barriers are closed, effectively partitioning the domain and preventing mixing between regions separated by the LCS. For P_3 (as well as for aperiodic flows), the transport barriers are open, enabling transport and

mixing across the whole domain.

The LCS-based description of transport is consistent with our long-term numerical advection calculations and has the advantage that it requires time-integration over a considerably shorter time-interval (fraction of the temporal period T of the flow, compared with hundreds to thousands of periods for numerical advection calculations). However, this approach does not explain *why* the mixing properties of the time-periodic flows are so dramatically different. A more insightful approach is discussed next.

5.3 Separatrix chaotic layers

As we discussed previously, area-preserving, time-periodic flows P_1, P_2, and P_3 can be treated formally as a perturbed Hamiltonian system (1), with the streamfunction (28) serving the role of the Hamiltonian. In particular, Ψ_0 plays the role of the unperturbed Hamiltonian and $\varepsilon\Psi_1$, the time-periodic perturbation. Transport in near-integrable time-periodic Hamiltonian systems and area-preserving flows has been studied extensively. It is well understood that, for weak perturbations, chaotic trajectories emerge in the neighborhood of the homo- or heteroclinic manifolds of saddle fixed points of the integrable unperturbed, or base, flow. These manifolds self-intersect as a result of the imposed perturbation, forming a homoclinic tangle with the lobe dynamics [102] which provides an insightful, albeit computationally intractable in practice, description of mixing in the separatrix chaotic layer (SCL).

However, there is an alternative description which can be used to describe the width of an SCL for low frequency perturbations such as the ones characterizing the flows we are dealing with here. For small ε, both Ψ and Ψ_0 are adiabatic invariants: away from the separatrices the change in each is slow, small (this is discussed in more detail later in this section), and bounded in the limit $t \to \infty$. In particular, the

change in Ψ over one period of the base flow is given by

$$\begin{aligned}\Delta\Psi &= \int_0^T \frac{d\Psi(\mathbf{x}(t),t)}{dt}dt = \int_0^T \partial_t\Psi(\tilde{\mathbf{x}}(t),0)dt + \int_0^T \dot{\tilde{\mathbf{x}}}(t)\cdot\nabla\Psi(\tilde{\mathbf{x}}(t),0)dt + \\ &+ \int_0^T t\,\partial_t^2\Psi(\tilde{\mathbf{x}}(t),0)dt + \cdots = O(\varepsilon)\left[1+O\left(\frac{\omega_1}{\omega_0}\right)\right], \qquad (56)\end{aligned}$$

where $\tilde{\mathbf{x}}$ is the streamline of the "frozen" streamfunction $\Psi(\mathbf{x},0)$. The second of the three integrals in (56) vanishes identically, so the first integral dominates and is the same for all tracers that originate on a particular streamline of Ψ. Hence, for slow perturbations ($\omega_1 \ll \omega_0$) the tracers closely follow the evolution of the streamlines of the time-dependent flow.

However, as shown by Neishtadt [81, 82], for Hamiltonian systems, the adiabatic invariance is broken for the trajectories (in our case streamlines) of the perturbed flow which cross the separatrices of the base (unpertubed) flow. If the value of Ψ at any of the saddles (more precisely, saddle periodic orbits of the perturbed flow) changes as a function of time, the corresponding separatrices will slowly sweep over a continuous band of streamlines (both effectively coincide with level sets of Ψ), causing quasirandom jumps in the value of the adiabatic invariant leading to an effective diffusion of the adiabatic invariant [126]. Destruction of adiabatic invariance for these streamlines will lead to transport and mixing across the corresponding band. This mechanism was identified as being responsible for mixing, e.g., in 3D volume-preserving flows in translating droplets perturbed by time-periodic electric fields [131, 132] and thermal gradients [125] as well as in some time-periodic 2D flows [32].

In our 2D time-periodic flows the boundaries of each SCL are defined by two level sets $\Psi_\pm(t)$ which touch (but do not intersect) the graph of $\Psi(\mathbf{x}_i(t),t)$, where $\mathbf{x}_i(t)$ is the saddle periodic orbit that anchors that SCL. In the adiabatic limit $\mathbf{x}_i(t)$ defines the location of the saddle of the instantaneous flow. As Fig. 47 (a)-(c) illustrates, all of the saddle periodic orbits for P_1 and P_2 and most of the orbits for P_3 are so compact that they can effectively be replaced by their averages $\bar{\mathbf{x}}_i$: in this case the

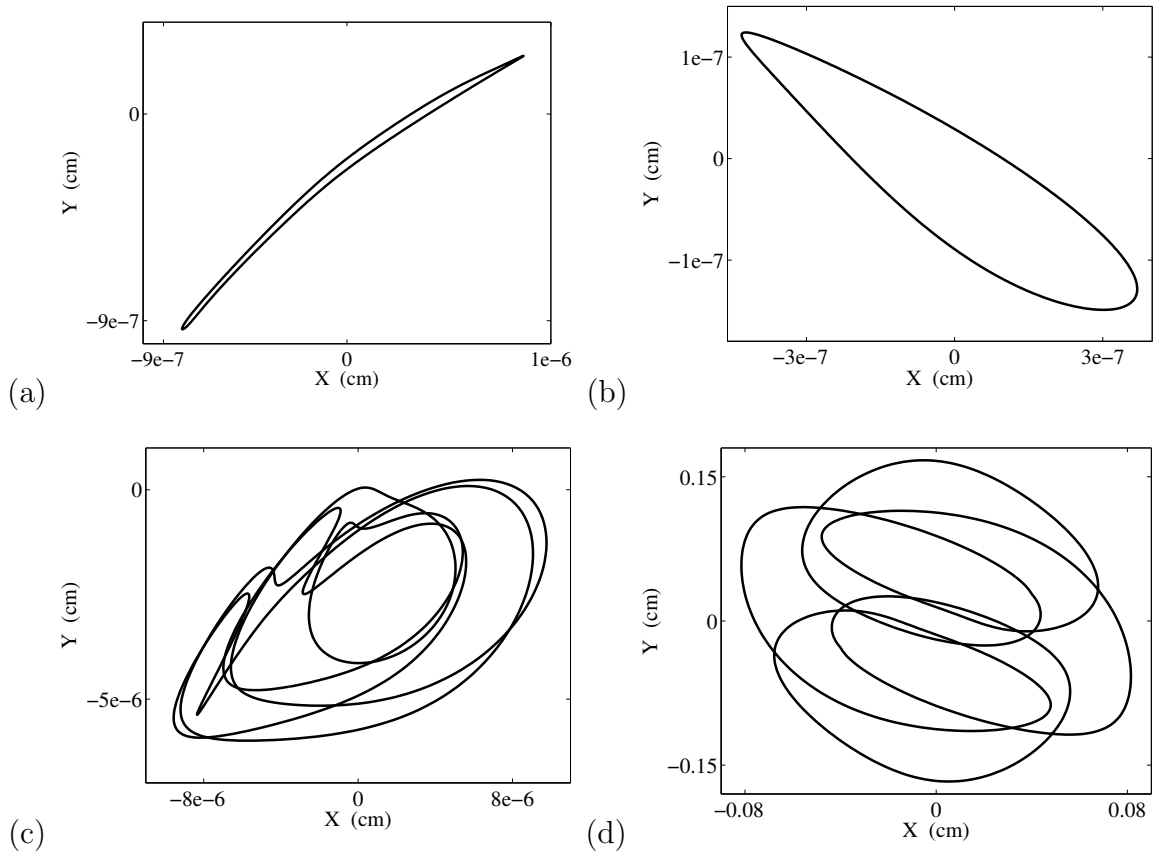

Figure 47: Saddle periodic orbits $\mathbf{x}_i(t) - \bar{\mathbf{x}}_i$. (a) P_1 at $A = 0.428$ s^{-2} with $\bar{\mathbf{x}}_1 = (0.625, 1.010)$, (b) P_2 at $A = 0.817$ s^{-2} with $\bar{\mathbf{x}}_1 = (0.625, 0.927)$, (c) P_3 at $A = 0.875$ s^{-2} with $\bar{\mathbf{x}}_1 = (4.375, 5.447)$, and (d) P_3 at $A = 0.875$ s^{-2} with $\bar{\mathbf{x}}_2 = (3.125, 2.947)$.

separatrices are defined simply by $\Psi(\bar{\mathbf{x}}_i, t)$. However, for some of the orbits of P_3, as illustrated by Fig. 47 (d), this is not the case, and the streamfunction must be evaluated on the separatrix as it evolves in time. From (56) we find that the values of the streamfunction defining the boundaries of an SCL evolve, to leading order in ω_1/ω_0, according to

$$\dot{\Psi}_{\pm}(t) \approx \frac{1}{T}\int_0^T \partial_t \Psi(\tilde{\mathbf{x}}_{\pm}(\tau), t) d\tau. \tag{57}$$

In the adiabatic limit, the solution of (57) is closely approximated by the value of streamfunction $\Psi(\mathbf{x}_{\pm}(t), t)$ evaluated for any tracer that originates on the streamline with $\Psi = \Psi_{\pm}$. An example is shown in Fig. 48(b) for the flow P_2. Red and blue curves show the values of the streamfunction at the two saddles of the flow, while the black curves show the values of the streamfunction for the tracers that move along the boundaries of the two SCLs. The fast oscillations of the black curves represent deviations from adiabatic behavior (smooth, periodic variation).

If the values of Ψ at different saddles cross, as they do for P_1 and P_3 (cf. Figs. 48(a) and 48(c)), then the respective SCLs merge, forming an even wider mixed region, with boundaries that can be found in the same way as for the non-overlapping SCLs. Although the perturbations $\varepsilon\Psi_1$ of the base flows Ψ_0 in our system cannot be considered weak, the mechanism of scattering of an adiabatic invariant still produces a remarkably accurate description of the mixed region as long as the perturbations are essentially monochromatic (e.g., for P_1 and P_2). The shape of the SCLs in the physical space is shown in Fig. 49 for all three periodic flows. For P_2, the tracers are seen to cover, quite precisely, the SCL which contained the initial set. The other SCL contains no tracers, since there is no transport between the SCLs. For P_1, the SCL is not uniformly covered by the tracers. This is not surprising, since the diffusion of the adiabatic invariant is relatively slow, as Fig. 39(a) illustrates. In fact, for P_1 the integration was performed over a time interval which corresponds to only 136 periods of the perturbation. In comparison, for P_2 the same time interval corresponds to 379

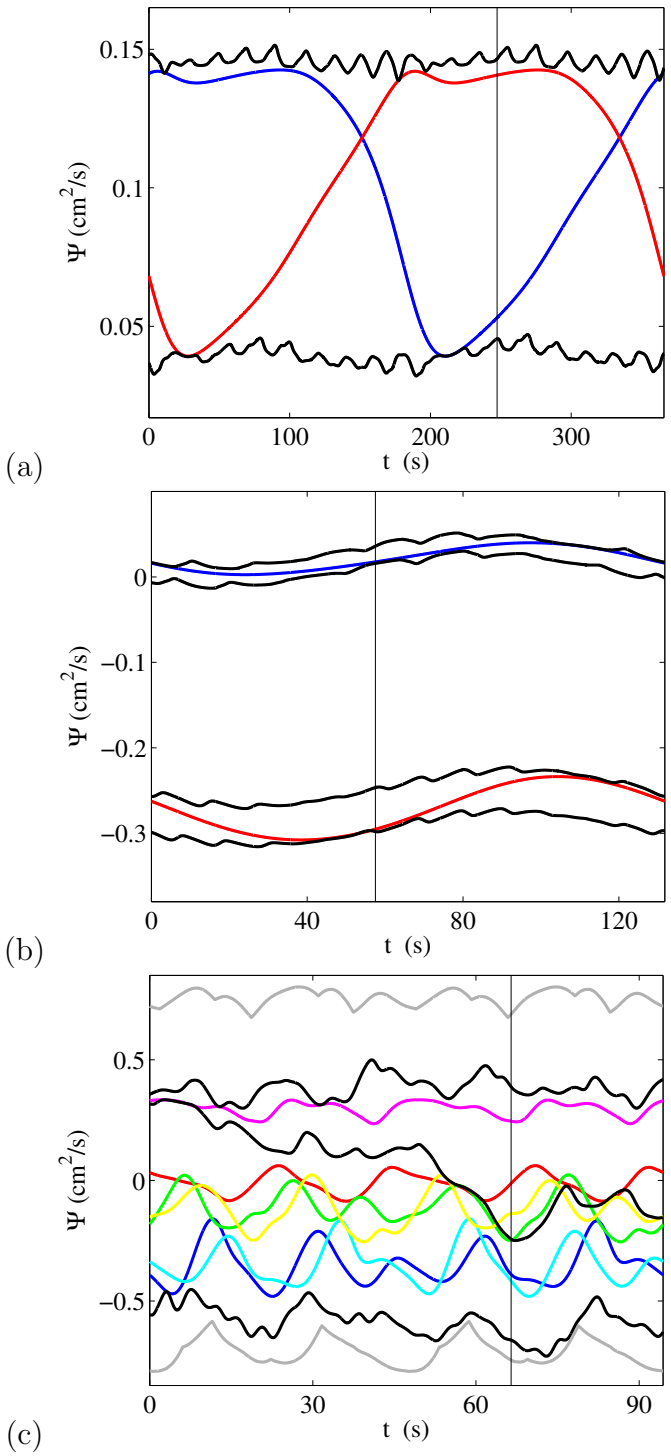

Figure 48: Time-dependent streamfunction Ψ evaluated evaluated over one temporal period of the flow, $0 < t < T$. The value at the saddles are shown in color. The values on the bounding streamlines are shown in black. The minimal and maximal values of Ψ (for P_3) are shown in gray. (a) P_1 at $A = 0.428$ s^{-2}, (b) P_2 at $A = 0.817$ s^{-2}, and (c) P_3 at $A = 0.875$ s^{-2}.

periods of the perturbation, leading to a much more uniform coverage of the SCL.

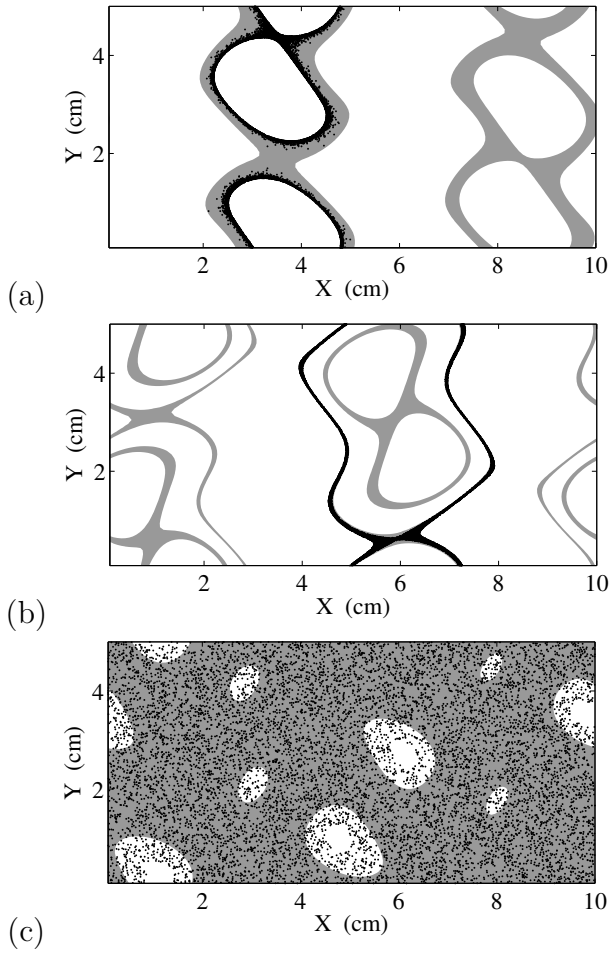

Figure 49: Separatrix chaotic layers (gray) with asymptotic tracer distributions (black dots). (a) P_1 at $A = 0.428$ s^{-2}, (b) P_2 at $A = 0.817$ s^{-2}, and (c) P_3 at $A = 0.875$ s^{-2}.

Unlike P_1 and P_2, the flow P_3 is characterized by global transport, with the mixed region which covers almost the entire domain. The merged SCLs define the shape of the mixed region reasonably well, although the agreement with the results of direct numerical simulation is not perfect, as Fig. 49(c) illustrates. For instance, the quartet of small islands predicted by the adiabatic description is completely filled in by the tracers. The islands are centered at the minimum of Ψ. Near the extrema of Ψ (gray curves at the top and bottom of Fig. 49(c)) a small error in evaluting $\Psi_\pm$ leads to a

large error in the shape of the corresponding boundary in real space. A very small decrease in the value of Ψ_- (e.g., due to inclusion of higher order corrections in (56) and (57) for moderate ε) will lead to a complete disappearance of these islands.

The adiabatic description also somewhat overestimates the size of the four big islands which are centered around the maximum of Ψ. Since the predicted boundary Ψ_+ is further away from the maximum of Ψ (see Fig. 50), a different explanation is likely needed. We discuss one possibility in the next Section.

5.4 Resonant chaotic layers

The flow P_3 is characterized by a perturbation which contains a lot of harmonics, so in addition to the SCLs, we may also need to take into account additional mixed regions that emerge outside of the SCLs. According to the KAM theory [66, 5, 79], in the presence of a time-periodic perturbation, resonant tori of the unperturbed flow (tori whose frequency $\omega_0(\Psi_0)$ is in rational ratio with the frequency ω_1 of the perturbation) break up, forming chains of elliptic and hyperbolic time-periodic orbits (or streamlines), each with their own sets of self-intersecting stable and unstable manifolds generating resonant chaotic layers (RCL). These RCLs can overlap with each other and with the SCLs, making the chaotic domain much broader.

The dynamics away from the separatrices can be described by computing the change in the value of Ψ_0 in the action-angle variables. The difference in the values of action

$$I = \oint y dx \tag{58}$$

between streamlines corresponding to values of the unperturbed streamfunction Ψ_0 and $\Psi_0 + d\Psi_0$ can be computed by integrating the separation $dr(s)$ between the streamlines

$$dI = \oint dr(s) ds = \oint \frac{dr}{d\Psi_0} d\Psi_0 ds = d\Psi_0 \oint dt = T_0 d\Psi_0 \tag{59}$$

which yields

$$I(\Psi_0) = \int_{\Psi_0^*}^{\Psi_0} \frac{dI}{d\Psi_0} d\Psi_0 = \int_{\Psi_0^*}^{\Psi_0} \frac{2\pi}{\omega_0} d\Psi_0, \tag{60}$$

where Ψ_0^* is the value of the unperturbed streamfunction at the elliptic fixed point enclosed by the streamline. The action I is the invariant of the unperturbed flow (and the adiabatic invariant of the perturbed flow), while the angle evolves according to

$$\dot{\theta} = \omega_0 = \frac{\partial H_0(I)}{\partial I} = 2\pi \frac{\partial \Psi_0}{\partial I}, \tag{61}$$

such that $H_0(I) = 2\pi\Psi_0(I)$. The perturbed Hamiltonian can then be written in terms of the action-angle variables:

$$H = H_0(I) + \varepsilon V(I, \theta, t) = 2\pi[\Psi_0(I) + \varepsilon \Psi_1(I, \theta, t)]. \tag{62}$$

According to the KAM theory of Hamiltonian systems [137] the width of the resonant chaotic layer that forms around the unperturbed streamline with frequency ω_0 which is in resonance with the perturbation frequency ω_1 of the perturbation, $m\omega_0 = k\omega_1$, is

$$\Delta I_{k,m} \approx \sqrt{\frac{2\pi}{\omega_0} \frac{\varepsilon V_{k,m}}{|\omega_0'|}}, \tag{63}$$

where $\omega_0' = d\omega_0/d\Psi_0$,

$$V_{k,m} = \frac{4\pi}{TT_0} \left| \int_0^{T_0} dt \int_0^T d\tau \Psi_1(\mathbf{x}(t), \tau) e^{ik\omega_1\tau - im\omega_0 t} \right|, \tag{64}$$

and the t-integral is taken along the streamline.

For low-frequency perturbations characterizing periodic flows P_1, P_2, and P_3, resonances with $m > 1$ will have exponentially small thickness and can be ignored. The width of the dominant k:1 RCLs (with $\Psi_0 = \Psi_0^k$) can be found from (63):

$$W(\Psi_0^k) = \frac{d\Psi_0}{dI} \Delta I_{k,1} \approx \sqrt{\varepsilon \frac{\omega_0}{2\pi} \frac{V_{k,1}}{|\omega_0'|}}. \tag{65}$$

Comparing these widths with the distances

$$S(\Psi_0^k) = \Psi_0^{k+1} - \Psi_0^k \tag{66}$$

between the neighboring resonant tori, we can determine which RCLs overlap and which do not for a particular strength of the perturbation.

Streamlines with low values of k lie extremely close to separatrices of the unperturbed flow, so numerical calculation of their period or separation becomes impossible. Instead, we can use the analytical result

$$T_0(\Psi_0) = -\sum_i \lambda_{l,i}^{-1} \ln \frac{|\Psi_0 - \psi_l|}{\xi_l}, \tag{67}$$

where ψ_l is the value of Ψ_0 characterizing the separatrix l, $\lambda_{l,i}$ are the positive eigenvalues of all the saddles on the separatrix and ξ_l is a constant. Indeed, we find that the distance from the separatrix to the nearest k:1 resonant streamline (1-torus) is exponentially small for low k:

$$|\Psi_0^k - \psi_l| = \xi_l \exp\left(-\frac{\chi_l}{\omega_0}\right) = \xi_l \exp\left(-\frac{\chi_l}{k\omega_1}\right), \tag{68}$$

where $\chi_l^{-1} \equiv \sum_i \lambda_{l,i}^{-1}/2\pi$. The distance between the resonant streamlines for low k can be found from (66) and (68):

$$S(\Psi_0^k) \approx \frac{\omega_1}{|\omega_0'|} \approx \frac{\xi_l \chi_l}{k^2 \omega_1} \exp\left(-\frac{\chi_l}{k\omega_1}\right). \tag{69}$$

It should be pointed out however that, for $\omega_1 \ll \omega_0$, the resonant streamlines with low k will be inside an SCL, so calculation of their width and separation is unnecessary. For P_1 and P_2, which are nearly monochromatic, the widths of the RCLs are exponentially small for moderate k, so none of their RCLs need to be considered.

For moderate ε, we can expect several RCLs to overlap with each other and with the SCL for non-monochromatic flows, such as P_3. Let us denote $p_\pm$ the orders of the resonant streamlines that lie inside an SCL and are the closest to its boundary (p_- near the low-Ψ side, p_+ near the high-Ψ side). If the half-width of the corresponding RCL exceeds the distance to the boundary of the SCL, the corresponding boundary of the chaotic region would be determined by an outer edge of an RCL (rather than an SCL).

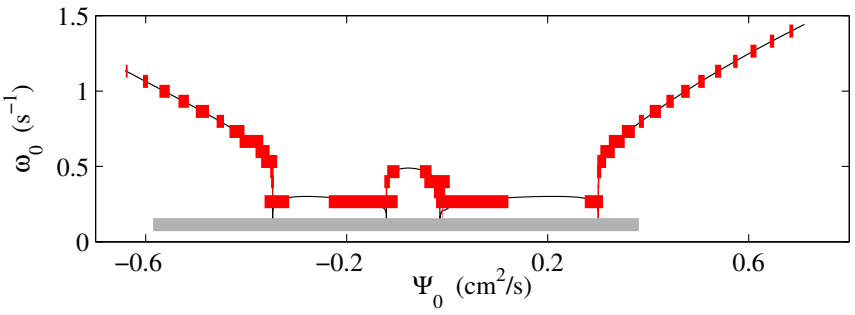

Figure 50: The frequency $\omega_0(\Psi_0)$ of the base flow for P_3. The range of Ψ_0 corresponding to the merged SCLs is shown in gray, with red bars showing the position and width of the RCLs.

This is illustrated in Fig. 50 where the SCLs and the RCLs are plotted along with the base flow frequency ω_0 as a function of Ψ_0. As discussed previously, the merged SCLs form a fully mixed region which covers most of the range between the minimim and the maximum of Ψ_0, where the boundaries of the mixed region in terms of Ψ_0 were obtained by temporally averaging $\Psi_\pm(t)$. However, the predicted sizes of the islands (both the small ones with $\Omega < 0$ surrounding the minima of Ψ_0 and the large ones with $\Omega > 0$ surrounding the maxima of Ψ_0) are somewhat larger than what the set of advected tracers defines, according to Fig. 49(c).

In principle, the RCLs can extend the mixed region of the flow beyond the SCLs. In this particular flow, the widths of the RCLs are comparable to their separation and we do find a significant number of overlapping RCLs in Fig. 50, especially near the separatrices of the base flow (characterized by the values of Ψ_0 for which $\omega_0 = 0$). However, the overlapping RCLs do not appreciably extend the region defined by the merged SCLs and, thus, do not appear to resolve the slight discrepancy between the predictions of the adiabatic description and direct numerical simulation. It is likely that higher order corrections are needed to more accurately estimate the widths of the RCLs, since the estimate (65) is valid only in the limit $\varepsilon \to 0$, while for P_3 we have $\varepsilon \approx 0.24$.

CHAPTER VI

CONCLUSION

One of the main objectives of this thesis was to understand how the transport properties of this fluid dynamical system change in the process of transitioning from steady laminar flow to turbulence. Particularly, as we asked in Section 1.5, "time-dependence is a necessary condition for mixing via chaotic advection in 2D, but is it also a sufficient condition?" It turns out that the answer to this question is definitively no. Even for strongly perturbed time-dependent flows which are qualitatively very similar, we found that for one of the flows, the mixing is poor, while for the other, near perfect mixing was achieved. The reason for this depends on whether or not the perturbation is monochromatic – the presence of multiple frequencies seems to be the sufficient condition for mixing rather than time-dependence. Another question posed in Section 1.5 was "can we expect the mixing to improve monotonically with the strength of externally applied shear?" Naively, one might think this to be the case – it seems quite natural that the stronger one drives a fluid, the more efficiently it would tend to mix. However, as the results in Chapter 5 showed, this is not necessarily true. As one would expect, we found that fluids in the turbulent regime mix extremely well, but, in transitioning to turbulence as the driving was increased, the flow progressed through a variety states each with very different mixing properties which did not advance in a monotonic fashion. Finally, we asked "is there a strong correlation between mixing quality of the flow and its type (steady, time-periodic, quasi-periodic, aperiodic)?" To a certain degree the answer is yes. Steady flows, which are integrable and thus exhibit regular motion, were very poor mixers as the theory predicts. Similarly, it was not surprising to find that the aperiodic flows were extremely efficient at mixing.

As far as periodic and quasiperiodic flows are concerned, we found that there is no direct correlation between the time-dependence and the quality of mixing. Rather, the mixing properties are affected by subtle properties of time-dependent flows, such as their spectral content. Although we illustrated that the mixing properties of a variety of flows could be described qualitatively using a fairly simple approach, a more detailed and careful analysis is required in some cases for a quantitative description.

One significant contribution provided by the research in this thesis is that we have developed an accurate 2D model of the flow as well as a very efficient and accurate numerical code to simulate it. The experiment itself is relatively easy to setup, and the tools are in place to facilitate comparison between theory and experiment on any number of issues. One area where this code could be extended and improved upon is the incorporation of more realistic boundary conditions rather than using periodic ones. However, even as it currently stands, we have found it to be in good agreement with the results found experimentally for low to moderate Reynolds numbers. We have also implemented the Newton-Krylov method for computing recurrent solutions, and it has proven to be extremely successful in finding them for a wide range of Reynolds numbers. Combined with the simulation code, it is straightforward to generate as much data as one desires, look for close recurrences, and feed these into the solver. The number of invariant solutions that one can compute is limited only by the length of the data set. The solver, as it currently stands, searches for fixed points, periodic orbits, and solutions which are shifted in the direction of continuous symmetry (traveling waves and relative periodic orbits), but it would be very easy to incorporate searches for solutions shifted in the directions of the discrete symmetries.

We have also done a very extensive bifurcation analysis and examined what solutions there are, how their stability properties change, and what new solutions arise as different parameters of the system are varied. There have been some bifurcation studies performed over the years for the Kolmogorov flows but, to the best of our

knowledge, none were anywhere near as comprehensive and thorough as the ones presented in Chapter 4. More important than the actual details presented in that Chapter, though, was the overarching result that the computed flows exhibits a large amount of structural stability. The solutions found as well as their various bifurcations persisted over a wide range of different parameters. This means that for an experimentalist, there is quite a lot of freedom in how they choose to design the experimental setup.

In Chapter 5 we presented the results and analysis of certain mixing properties for many of the different flows that we found. In the literature there are a variety of ways that are used to describe mixing in fluid flows. For instance, Lagrangian Coherent Structures defined as the ridges of Finite Time Lyapunov Exponents are interpreted as transport barriers. At best, these structures can give only qualitative information about the flow. One can see that if the ridges do not exhibit much folding then flow is likely a poor mixer and vice-versa. However, one cannot quantify the quality of mixing either in terms of its rate or the size of the mixed region. Furthermore, we found that these ridges do not always serve as barriers to transport on large time scales. Similarly, one can use the results of long-time tracer advection in order to describe the mixing quality, which we have done. But, as we found out, this is an extraordinarily expensive way to quantify mixing; and the validity of these long-time computations cannot be trusted without the use of very high-order, implicit integration schemes. As described in Chapter 5, we have developed an extremely economical description of the quality of mixing for low frequency perturbations. And this description works remarkably well even for strongly perturbed time-periodic flows. However, as we discovered, these calculations will have to be done more carefully and higher order corrections will need to be included for perturbations containing a large number of harmonics. Nonetheless, the results we have so far seem to indicate that we are on the right track.

REFERENCES

[1] Allègre, C. J. and Turcotte, D. L., "Implications of a two-component marble-cake mantle," *Nature*, vol. 323, no. 6084, pp. 123–127, 1986.

[2] Aref, H., "Stirring by chaotic advection," *Journal of Fluid Mechanics*, vol. 143, pp. 1–21, 1984.

[3] Aref, H., "The development of chaotic advection," *Physics of Fluids*, vol. 14, p. 1315, 2002.

[4] Aref, H. and Balachandar, S., "Chaotic advection in a Stokes flow," *Physics of Fluids*, vol. 29, no. 11, pp. 3515–3521, 1986.

[5] Arnold, V., "Small denominators, 1: Mappings of the circumference onto itself," *AMS Translations*, vol. 46, pp. 213–288, 1965.

[6] Arnold, V. I. and Meshalkin, L. D., "The A. N. Kolmogorov seminar on selected problems of analysis (1958-1959)," *Usp. Mat. Nauk*, vol. 15, no. 1, pp. 247–250, 1960.

[7] Arratia, P. E. and Gollub, J. P., "Statistics of stretching fields in experimental fluid flows exhibiting chaotic advection," *Journal of Statistical Physics*, vol. 121, pp. 805–821, 2005.

[8] Ascher, U. M., Ruuth, S. J., and Wetton, B. T. R., "Implicit-explicit methods for time-dependent partial differential equations," *SIAM Journal on Numerical Analysis*, vol. 32, pp. 797–823, 1995.

[9] Ballal, B. Y. and Rivlin, R. S., "Flow of a newtonian fluid between eccentric rotating cylinders: inertial effects," *Archive for Rational Mechanics and Analysis*, vol. 62, no. 3, pp. 237–294, 1976.

[10] Batchaev, A. and Dovzhenko, V., "Laboratory simulation of the stability loss of periodic zonal flows," in *Akademiia Nauk SSSR Doklady*, vol. 273, pp. 582–584, 1983.

[11] Behringer, R., Meyers, S., and Swinney, H., "Chaos and mixing in a geostrophic flow," *Physics of Fluids A: Fluid Dynamics*, vol. 3, p. 1243, 1991.

[12] Beyer, P. and Benkadda, S., "Advection of passive particles in the Kolmogorov flow," *Chaos*, vol. 11, pp. 774–779, 2001.

[13] Boffetta, G., Lacorata, G., Redaelli, G., and Viulpiani, A., "Detecting barriers to transport: a review of different techniques," *Physica D*, vol. 159, pp. 58–70, 2001.

[14] Bondarenko, N. F., Gak, M. Z., and Dolzhanskii, F. V., "Laboratory and theoretical models of plane periodic flows," *Atmospheric and Oceanic Physics*, vol. 15, pp. 711–716, 1979.

[15] Braun, D., "Pcr by thermal convection," *Modern Physics Letters B*, vol. 18, no. 16, pp. 775–784, 2004.

[16] Braun, R., Feudel, F., and Seehafer, N., "Bifurcations and chaos in an array of forced vortices," *Physical Review E*, vol. 55, no. 6, p. 6979, 1997.

[17] Brown, P. and Saad, Y., "Hybrid krylov methods for nonlinear systems of equations," *SIAM Journal on Scientific and Statistical Computing*, vol. 11, no. 3, pp. 450–481, 1990.

[18] Cardoso, O., Marteau, D., and Tabeling, P., "Quantitative experimental study of the free decay of quasi-two-dimensional turbulence," *Physical review E*, vol. 49, no. 1, p. 454, 1994.

[19] Chaiken, J., Chevray, R., Tabor, M., and Tan, Q. M., "Experimental study of Lagrangian turbulence in a Stokes flow," *Proceedings of the Royal Society of London. A. Mathematical and Physical Sciences*, vol. 408, no. 1834, pp. 165–174, 1986.

[20] Chaiken, J., Chu, C. K., Tabor, M., and Tan, Q. M., "Lagrangian turbulence and spatial complexity in a Stokes flow," *Physics of Fluids*, vol. 30, no. 3, pp. 687–694, 1987.

[21] Chandler, G. J. and Kerswell, R. R., "Invariant recurrent solutions embedded in a turbulent two-dimensional kolmogorov flow," *Journal of Fluid Mechanics*, vol. 722, pp. 554–595, 2013.

[22] Chen, Z. M. and Price, W. G., "Secondary fluid flows driven electromagnetically in a two-dimensional extended duct," *Proceedings of the Royal Society A: Mathematical, Physical and Engineering Science*, vol. 461, no. 2058, pp. 1659–1683, 2005.

[23] Chien, W. L., Rising, H., and Ottino, J. M., "Laminar mixing and chaotic mixing in several cavity flows," *Journal of Fluid Mechanics*, vol. 170, no. 1, pp. 355–377, 1986.

[24] Chován, T. and Guttman, A., "Microfabricated devices in biotechnology and biochemical processing," *TRENDS in Biotechnology*, vol. 20, no. 3, pp. 116–122, 2002.

[25] Clercx, H. J. H., Van Heijst, G. J. F., and Zoeteweij, M. L., "Quasi-two-dimensional turbulence in shallow fluid layers: The role of bottom friction and fluid layer depth," *Physical review E*, vol. 67, no. 6, p. 066303, 2003.

[26] Clercx, H. and van Heijst, G., "Two-dimensional navier-stokes turbulence in bounded domains," 2009.

[27] Coulliette, C., Lekien, F., Paduan, J., Haller, G., and Marsden, J., "Optimal pollution mitigation in monterey bay based on coastal radar data and nonlinear dynamics," *Environmental science & technology*, vol. 41, no. 18, pp. 6562–6572, 2007.

[28] Crisanti, A., Falcioni, M., Paladin, G., and Vulpiani, A., "Lagrangian chaos: transport, mixing and diffusion in fluids," *Rivista del Nuovo Cimento*, vol. 14, pp. 1–80, 1991.

[29] Cvitanović, P., Artuso, R., Mainieri, R., Tanner, G., and Vattay, G., *Chaos: Classical and Quantum*. Niels Bohr Institute, 2012.

[30] Cvitanović, P., Artuso, R., Mainieri, R., Tanner, G., and Vattay, G., *Chaos: Classical and Quantum*. Niels Bohr Institute, 2012.

[31] Cvitanovic, P. and Lan, Y., "Turbulent fields and their recurrences," in *Proceedings of 10th International Workshop on Multiparticle Production: Correlations and Fluctuations in QCD*, pp. 313–325, 2003.

[32] Danilov, S. D., Dovzhenko, V. A., and Yakushkin, I. G., "Transport of a passive scalar and lagrangian chaos in a hamiltonian hydrodynamic system," *Journal of Experimental and Theoretical Physics*, vol. 91, no. 2, pp. 423–432, 2000.

[33] Dauxois, T., Fauve, S., and Tuckerman, L., "Stability of periodic arrays of vortices," *Physics of Fluids*, vol. 8, p. 487, 1996.

[34] Dennis, J. and Schnabel, R., *Numerical methods for unconstrained optimization and nonlinear equations*, vol. 16. Society for Industrial Mathematics, 1987.

[35] Dolzhanskii, F. V., Krymov, V. A., and Manin, D. Y., "An advanced experimental investigation of quasi-two-dimensional shear flows," *Journal of Fluid Mechanics*, vol. 241, pp. 705–722, 1992.

[36] Dolzhanskii, F., Krymov, V., and Manin, D. Y., "Stability and vortex structures of quasi-two-dimensional shear flows," *Physics-Uspekhi*, vol. 33, no. 7, pp. 495–520, 1990.

[37] Dovzhenko, V., Krymov, V. A., and Ponomarev, V., "Experimental and theoretical investigation of the shear flow generated by an axially symmetric force," *Izv. Akad. Nauk SSSR, Fiz. Atmos. Okeana*, vol. 20, p. 693, 1984.

[38] Dovzhenko, V., Obukhov, A., and Ponomarev, V., "Generation of vortices in an axisymmetric shear flow," *Fluid Dynamics*, vol. 16, no. 4, pp. 510–518, 1981.

[39] Eckhardt, B., Schneider, T. M., Hof, B., and Westerweel, J., "Turbulence transition in pipe flow," *Annu. Rev. Fluid Mech.*, vol. 39, pp. 447–468, 2007.

[40] Eisenstat, S. and Walker, H., "Choosing the forcing terms in an inexact newton method," *SIAM Journal on Scientific Computing*, vol. 17, no. 1, pp. 16–32, 1996.

[41] El-Ali, J., Sorger, P. K., and Jensen, K. F., "Cells on chips," *Nature*, vol. 442, no. 7101, pp. 403–411, 2006.

[42] Evans, J., Liepmann, D., and Pisano, A. P., "Planar laminar mixer," *MEMS97, Nagoya, Japan*, pp. 96–101, 1997.

[43] Feudel, F. and Seehafer, N., "Bifurcations and pattern formation in a two-dimensional Navier-Stokes fluid," *Physical Review E*, vol. 52, no. 4, p. 3506, 1995.

[44] Fiorentino, L., Olascoaga, M., Reniers, A., Feng, Z., Beron-Vera, F., and MacMahan, J., "Using lagrangian coherent structures to understand coastal water quality," *Continental Shelf Research*, 2012.

[45] Franceschini, V. and Giberti, C., "Qualitative and quantitative stabilized behavior of truncated two-dimensional naver-stokes equations," *Theoretical and Computational Fluid Dynamics*, vol. 2, no. 4, pp. 185–192, 1991.

[46] Freund, R., "A transpose-free quasi-minimal residual algorithm for non-hermitian linear systems," *SIAM Journal on Scientific Computing*, vol. 14, no. 2, pp. 470–482, 1993.

[47] Fukuta, H. and Murakami, Y., "Nonlinear stability of Kolmogorov flow with bottom-friction using the energy method," *Journal of the Physical Society of Japan*, vol. 64, pp. 3725–3739, 1995.

[48] Gent, P. R. and McWilliams, J. C., "Isopycnal mixing in ocean circulation models," *Journal of Physical Oceanography*, vol. 20, pp. 150–155, 1989.

[49] Gibson, J. F., Halcrow, J., and Cvitanović, P., "Visualizing the geometry of state space in plane couette flow," *arXiv preprint arXiv:0705.3957*, 2007.

[50] Gotoh, K. and Yamada, M., "Instability of a cellular flow," *Physical Society of Japan, Journal*, vol. 53, pp. 3395–3398, 1984.

[51] Hairer, E., Lubich, C., and Wanner, G., *Geometric Numerical Integration: Structure-Preserving Algorithms for Ordinary Differential Equations*. Springer, 2006.

[52] Haller, G. personal communication.

[53] Haller, G. and Pope, A. C., "Eddy growth and mixing in mesoscale oceanographic flows," *Nonlinear Processes in Geophysics*, vol. 4, pp. 223–235, 1997.

[54] Haynes, P. H., "Transport and mixing in the atmosphere," in *Mechanics of the 21st Century : Proceedings of the 21st International Congress of Theoretical and Applied Mechanics*, 2005.

[55] Held, I. M., Pierrehumbert, R. T., Garner, S. T., and Swanson, K. L., "Surface quasi-geostrophic dynamics," *Journal of Fluid Mechanics*, vol. 282, pp. 1–20, 1995.

[56] Hoffman, N. R. A. and McKenzie, D. P., "The destruction of geochemical heterogeneities by differential fluid motions during mantle convection," *Geophysical Journal of the Royal Astronomical Society*, vol. 82, pp. 163–206, 1985.

[57] Honji, H., "Instability of an electromagnetically driven vortex array," in *Proceedings of the Sixth Asian Congress of Fluid Mechanics (Nanyang Technological University, Singapore, 1995)*, pp. 1218–1221, 1995.

[58] Jüttner, B., Marteau, D., Tabeling, P., and Thess, A., "Numerical simulations of experiments on quasi-two-dimensional turbulence," *Physical Review E*, vol. 55, no. 5, p. 5479, 1997.

[59] Kellay, H. and Goldburg, W. I., "Two-dimensional turbulence: a review of some recent experiments," *Reports on Progress in Physics*, vol. 65, no. 5, p. 845, 2002.

[60] Kelley, C., *Iterative methods for linear and nonlinear equations*, vol. 16. Society for Industrial Mathematics, 1995.

[61] Kelley, C., *Solving nonlinear equations with Newton's method*, vol. 1. Society for Industrial Mathematics, 2003.

[62] Kelley, D. H. and Ouellette, N. T., "Separating stretching from folding in fluid mixing," *Nature Physics*, vol. 7, no. 6, pp. 477–480, 2011.

[63] Kerswell, R., "Recent progress in understanding the transition to turbulence in a pipe," *Nonlinearity*, vol. 18, no. 6, p. R17, 2005.

[64] Khakhar, D. V., Rising, H., and Ottino, J. M., "Analysis of chaotic mixing in two model systems," *Journal of Fluid Mechanics*, vol. 172, pp. 419–51, 1986.

[65] Knoll, D. A. and Keyes, D. E., "Jacobian-free Newton-Krylov methods: a survey of approaches and applications," *Journal of Computational Physics*, vol. 193, pp. 357–397, 2004.

[66] Kolmogorov, A. N., "On conservation of conditionally periodic motions under small perturbations of the Hamiltonian," *Dokl. Akad. Nauk, SSSR*, vol. 98, pp. 527–530, 1954.

[67] Lan, Y. and Cvitanović, P., "Variational method for finding periodic orbits in a general flow," *Physical Review E*, vol. 69, no. 1, p. 016217, 2004.

[68] Lasagni, F., "Canonical runge-kutta methods," *Zeitschrift für Angewandte Mathematik und Physik (ZAMP)*, vol. 39, no. 6, pp. 952–953, 1988.

[69] Lee, Y. K., Deval, J., Tabeling, P., and Ho, C. M., "Chaotic mixing in electrokinetically and pressure driven micro flows," in *Micro Electro Mechanical Systems, 2001. MEMS 2001. The 14th IEEE International Conference on MEMS*, pp. 483–486, IEEE, 2001.

[70] Lekien, F., Coulliette, C., Mariano, A., Ryan, E., Shay, L., Haller, G., and Marsden, J., "Pollution release tied to invariant manifolds: A case study for the coast of florida," *Physica D: Nonlinear Phenomena*, vol. 210, no. 1, pp. 1–20, 2005.

[71] Leong, C. W. and Ottino, J. M., "Experiments on mixing due to chaotic advection in a cavity," *Journal of Fluid Mechanics*, vol. 209, no. 1, pp. 463–499, 1989.

[72] Mackay, R. S., Meiss, J. D., and Percival, I. C., "Stochasticity and transport in Hamiltonian systems," *Phys. Rev. Lett.*, vol. 52, pp. 697–700, 1984.

[73] Marchuk, G. I., *Methods of Numerical Mathematics*. Springer-Verlag, 1975.

[74] Marchuk, G., "On the theory of the splitting-up method," in *Proceedings of the 2nd Symposium on Numerical Solution of Partial Differential Equations, SVNSPADE*, pp. 469–500, 1970.

[75] Marteau, D., Cardoso, O., and Tabeling, P., "Equilibrium states of two-dimensional turbulence: An experimental study," *Physical Review E*, vol. 51, pp. 5124–5127, 1995.

[76] Mathis, S. and Zahn, J. P., "Transport and mixing in the radiation zones of rotating stars," *Astronomy and Astrophysics*, vol. 425, no. 1, pp. 229–242, 2004.

[77] Melnikov, V. K., "On the stability of the center for time-periodic perturbations," *Trans. Moscow Math. Soc.*, vol. 12, pp. 1–57, 1963.

[78] Meshalkin, L. D. and Sinai, Y. G., "Investigation of the stability of a stationary solution of equations for the plane movement of an incompressible viscous fluid," *J. Appl. math. Mech. (Prikl. Mat. Mekh.)*, vol. 25, p. 1700, 1961.

[79] Moser, J., "On invariant curves of area-preserving mappings of an annulus.," *Nachr. Akad. Wiss. Göttingen, II Math. Phys.*, vol. 1, pp. 1–20, 1962.

[80] Nakamura, Y., "Spatio-temporal dynamics of forced periodic flows in a confined domain," *Physics of Fluids*, vol. 9, p. 3275, 1997.

[81] Neishtadt, A., "Change of an adiabatic invariant at a separatrix," *Sov. J. Plasma Phys.*, vol. 12, pp. 568–573, 1986.

[82] Neishtadt, A., "On the change in the adiabatic invariant on crossing a separatrix in systems with two degrees of freedom," *PMM USSR*, vol. 51, pp. 586–592, 1987.

[83] Newhouse, S., Ruelle, D., and Takens, F., "Occurrence of strange axiom a attractors near quasiperiodic flows on t^m, $m \geq 3$," *Comm. Math. Phys.*, vol. 64, pp. 35–40, 1978.

[84] Ngyen-Duc, J. M., Caperan, P., and Sommeria, J., *Advances In Turbulence*, ch. Experimental study of the inverse energy cascade in two-dimensional turbulence, pp. 265–268. Springer-Verlag, 1987.

[85] Niu, X. and Lee, Y. K., "Efficient spatial-temporal chaotic mixing in microchannels," *Journal of Micromechanics and Microengineering*, vol. 13, no. 3, p. 454, 2003.

[86] Olascoaga, M. J. and Haller, G., "Forecasting sudden changes in environmental pollution patterns," *Proceedings of the National Academy of Sciences*, vol. 109, no. 13, pp. 4738–4743, 2012.

[87] Ottino, J. M. and Chella, R., "Laminar mixing of polymeric liquids; a brief review and recent theoretical developments," *Polymer Engineering & Science*, vol. 23, no. 7, pp. 357–379, 2004.

[88] Ottino, J. M., Leong, C. W., Rising, H., and Swanson, P. D., "Morphological structures produced by mixing in chaotic flows," *Nature*, vol. 333, pp. 419–425, 1988.

[89] Ouellette, N. T. and Gollub, J. P., "Dynamic topology in spatiotemporal chaos," *Physics of Fluids*, vol. 20, p. 064104, 2008.

[90] Panic, S., Loebbecke, S., Tuercke, T., Antes, J., and Boskovic, D., "Experimental approaches to a better understanding of mixing performance of microfluidic devices," *Chemical Engineering Journal*, vol. 101, pp. 409–419, 2004.

[91] Paret, J. and Tabeling, P., "Intermittency in the two-dimensional inverse cascade of energy: Experimental observations," *Physics of Fluids*, vol. 10, p. 3126, 1998.

[92] Peacock, T. and Dabiri, J., "Introduction to focus issue: Lagrangian coherent structures," *Chaos*, vol. 20, no. 1, pp. Art–No, 2010.

[93] Peacock, T. and Haller, G., "Lagrangian coherent structures: The hidden skeleton of fluid flows," *Physics Today*, vol. 66, no. 2, pp. 41–47, 2013.

[94] Peng, J. and Dabiri, J., "Transport of inertial particles by lagrangian coherent structures: application to predator-prey interaction in jellyfish feeding," *Journal of Fluid Mechanics*, vol. 623, no. 12, pp. 75–84, 2009.

[95] Peyret, R., *Spectral methods for incompressible viscous flow*, vol. 148. Springer, 2002.

[96] Pierrehumbert, R. T., "Largescale horizontal mixing in planetary atmospheres," *Physics of Fluids A*, vol. 3, pp. 1250–1260, 1991.

[97] Platt, N., Sirovich, L., and Fitzmaurice, N., "An investigation of chaotic Kolmogorov flows," tech. rep., DTIC Document, 1990.

[98] Pomeau, Y. and Manneville, P., "Intermittent transition to turbulence in dissipative dynamical systems," *Comm. Math. Phys.*, vol. 74, pp. 189–197, 1980.

[99] Proshutinsky, A. Y. and Johnson, M. A., "Two circulation regimes of the wind-driven arctic ocean," *Journal of Geophysical Research*, vol. 102, no. C6, pp. 12493–12, 1997.

[100] Rivera, M. K. and Ecke, R. E., "Pair dispersion and doubling time statistics in two-dimensional turbulence," *Physical review letters*, vol. 95, no. 19, p. 194503, 2005.

[101] Robert, H. and Montgomery, D., "Two-dimensional turbulence," *Rep. Prog. Phys*, vol. 43, 1980.

[102] Rom-Kedar, V., Leonard, A., and Wiggins, S., "An analytical study of transport, mixing and chaos in an unsteady vortical flow," *Journal of Fluid Mechanics*, vol. 214, pp. 347–394, 1990.

[103] Rothstein, D., Henry, E., and Gollub, J. P., "Persistent patterns in transient chaotic fluid mixing," *Nature*, vol. 401, no. 6755, pp. 770–772, 1999.

[104] Ruelle, D. and Takens, F., "On the nature of turbulence," *Comm. Math. Phys.*, vol. 20, pp. 167–192, 1971.

[105] Satijn, M., Cense, A., Verzicco, R., Clercx, H., and Van Heijst, G., "Three-dimensional structure and decay properties of vortices in shallow fluid layers," *Physics of fluids*, vol. 13, p. 1932, 2001.

[106] Schrenk, W. and Alfrey Jr, T., "Coextruded multilayer polymer films and sheets," *Polymer blends*, vol. 2, p. 129, 1978.

[107] Shadden, S. C., Dabiri, J. O., and Marsden, J. E., "Lagrangian analysis of fluid transport in empirical vortex ring flows," *Physics of Fluids*, vol. 18, p. 047105, 2006.

[108] Shadden, S. C., Lekien, F., and Marsden, J. E., "Definition and properties of Lagrangian coherent structures from finite-time lyapunov exponents in two-dimensional aperiodic flows," *Physica D*, vol. 212, pp. 271–304, 2005.

[109] Shadden, S. C. and Taylor, C. A., "Characterization of coherent structures in the cardiovascular system," *Annals of biomedical engineering*, vol. 36, no. 7, pp. 1152–1162, 2008.

[110] Sivashinsky, G. and Yakhot, V., "Negative viscosity effect in large-scale flows," *Phys. Fluids;(United States)*, vol. 28, no. 4, 1985.

[111] Sommeria, J., "Experimental study of the two-dimensional inverse energy cascade in a square box," *Journal of fluid mechanics*, vol. 170, no. 1, pp. 139–168, 1986.

[112] Soskin, S. M. and Mannella, R., "Maximal width of the separatrix chaotic layer," *Phys. Rev. E*, vol. 80, p. 066212, 2009.

[113] Strang, G., "On the construction and comparison of difference schemes," *SIAM Journal on Numerical Analysis*, vol. 5, no. 3, pp. 506–517, 1968.

[114] Stremler, M. A., Haselton, F. R., and Aref, H., "Designing for chaos: applications of chaotic advection at the microscale," *Philosophical Transactions of the Royal Society of London. Series A: Mathematical, Physical and Engineering Sciences*, vol. 362, no. 1818, pp. 1019–1036, 2004.

[115] Suri, B., Tithof, J., Mitchell, R., Grigoriev, R. O., and Schatz, M. F., "Velocity profile in a two-layer Kolmogorov-like flow." Submitted to J. Fluid Mech.

[116] Tabeling, P., Perrin, B., and Fauve, S., "Instability of a linear array of forced vortices," *EPL (Europhysics Letters)*, vol. 3, no. 4, p. 459, 1987.

[117] Tabeling, P., "Two-dimensional turbulence: a physicist approach," *Physics Reports*, vol. 362, no. 1, pp. 1–62, 2002.

[118] Takaoka, M., "Stability of triangular cell flows," *J. Phys. Soc. Japan*, vol. 58, pp. 2223–2226, 1989.

[119] Thess, A., "Instabilities in two-dimensional spatially periodic flows. Part I: Kolmogorov flow," *Physics of Fluids A*, vol. 4, pp. 1385–1395, 1992.

[120] Thess, A., "Instabilities in two-dimensional spatially periodic flows. part ii: Square eddy lattice," *Physics of Fluids A: Fluid Dynamics*, vol. 4, p. 1396, 1992.

[121] Thess, A., "Instabilities in two-dimensional spatially periodic flows. part iii: Inviscid triangular lattice," *Physics of Fluids A: Fluid Dynamics*, vol. 5, p. 335, 1993.

[122] Tsuda, A., Laine-Pearson, F. E., and Hydon, P. E., "Why chaotic mixing of particles is inevitable in the deep lung," *Journal of Theoretical Biology*, vol. 286, pp. 57–66, 2011.

[123] Vainchtein, D., Neishtadt, A., and Mezic, I., "On passage through resonances in volume-preserving systems," *Chaos*, vol. 16, p. 043123, 2006.

[124] Vainchtein, D., Rovinsky, E., Zelenyi, L., and Neishtadt, A., "Resonances and particle stochastization in nonhomogeneous electromagnetic fields," *J. of Nonlinear Science*, vol. 14, pp. 173–205, 2004.

[125] Vainchtein, D., Widloski, J., and Grigoriev, R., "Mixing properties of steady flow in thermocapillary driven droplets," *Physics of Fluids*, vol. 19, p. art. 067102, 2007.

[126] Vainchtein, D., Widloski, J., and Grigoriev, R., "Resonant mixing in perturbed action-action-angle flow," *Phys. Rev. E*, vol. 78, p. art. 026302, 2008.

[127] Van der Vorst, H., "Bi-cgstab: A fast and smoothly converging variant of bi-cg for the solution of nonsymmetric linear systems," *SIAM Journal on scientific and Statistical Computing*, vol. 13, no. 2, pp. 631–644, 1992.

[128] Verron, J. and Sommeria, J., "Numerical simulation of a two-dimensional turbulence experiment in magnetohydrodynamics," *Physics of Fluids*, vol. 30, p. 732, 1987.

[129] Voth, G. A., Haller, G., and Gollub, J. P., "Experimental measurements of stretching fields in fluid mixing," *Physical Review Letters*, vol. 88, p. 254501, 2002.

[130] Voth, G. A., Saint, T. C., Dobler, G., and Gollub, J. P., "Mixing rates and symmetry breaking in two-dimensional chaotic flow," *Physics of Fluids*, vol. 15, pp. 2560–2566, 2003.

[131] Ward, T. and Homsy, G., "Electrohydrodynamically driven chaotic mixing in a translating drop," *Phys. Fluids*, vol. 13, pp. 3521–3525, 2001.

[132] Ward, T. and Homsy, G., "Electrohydrodynamically driven chaotic mixing in a translating drop. II. Experiments," *Phys. Fluids*, vol. 15, pp. 2987–2994, 2003.

[133] Weigl, B. H., Bardell, R. L., and Cabrera, C. R., "Lab-on-a-chip for drug development," *Advanced drug delivery reviews*, vol. 55, no. 3, pp. 349–377, 2003.

[134] Weldon, M., Peacock, T., Jacobs, G., Helu, M., and Haller, G., "Experimental and numerical investigation of the kinematic theory of unsteady separation," *Journal of Fluid Mechanics*, vol. 611, pp. 1–12, 2008.

[135] Wiggins, S., "The dynamical systems approach to Lagrangian transport in oceanic flows," *Annu. Rev. Fluid Mech.*, vol. 37, pp. 295–328, 2005.

[136] Yao, S. and Bakajin, O., "Improvements in mixing time and mixing uniformity in devices designed for studies of protein folding kinetics," *Analytical chemistry*, vol. 79, no. 15, pp. 5753–5759, 2007.

[137] Zaslavsky, G. M., *The physics of chaos in Hamiltonian systems*. Imperial College Press London, 2007.

VITA

Radford Mitchell, Jr., the son of Radford Mitchell, Sr. and Rebecca Mitchell, was born in 1976 in Norfolk, Virginia. At the age of three, he moved to Virginia Beach, Virginia and lived there until completing high school. In the fall of that year, he moved to Blacksburg, Virginia to pursue his studies in the Mechanical Engineering department at Virginia Polytechnic Institute. After a year and a half, dissatisfied with engineering, and academic life in general, and not wanting to waste any more of his parents' money, he left Blacksburg and spent several months traveling throughout the United States. Eventually he ended up in a small resort town in Sedona, Arizona where he made a living working as a chef at a few different restaurants. After saving up enough money, he spent several months traveling all over Costa Rica, Panama, and Nicaragua. Upon his return to Arizona, he obtained his A.S. from Yavapai Community College and then transferred to Flagstaff to study physics at Northern Arizona University. He graduated from there with a B.S. in Physics, a B.S. in Mathematics, and a Minor in Spanish. In 2004, he moved to Atlanta, Georgia to pursue a Ph.D. in Physics at the Georgia Institute of Technology. Apart from math and physics, Radford also enjoys traveling, cooking, and playing various musical instruments, his first love being the acoustic guitar.